Synchronization of Dust-Density Waves and Formation of Torus-Shaped Dust Clouds in a Magnetized Anodic Plasma

Dissertation
zur Erlangung des Doktorgrades
der Mathematisch-Naturwissenschaftlichen Fakultät
der Christian-Albrechts-Universität zu Kiel

vorgelegt von
Iris Pilch

Kiel
Mai 2010

Referent:	Prof. Dr. A. Piel
Korreferent:	Prof. Dr. H. Kersten
Tag der mündlichen Prüfung: ...	09. Juli 2010
Zum Druck genehmigt: Kiel, den	

Der Dekan

Kurzfassung

In dieser Dissertation werden zwei unterschiedliche dynamische Zustände von Staubwolken in einem schwach magnetisierten anodischen Plasma untersucht. Die Staubwolken sind in einem Kraftgleichgewicht aus elektrischer Feldkraft und Ionenwindkraft eingefangen. Es wird zwischen kompakten und torusförmigen Staubwolken unterschieden. In kompakten Staubwolken können Staubdichtewellen, welche durch strömende Ionen angeregt werden, beobachtet werden. Diese Staubwolken werden anhand des Verhältnisses der Wolkenlänge zu einer typischen Wellenlänge weiter untergliedert. In torusförmigen Staubwolken ist ein staubfreier Bereich, welcher als "Void" bezeichnet wird, gefunden worden. Die Staubteilchen rotieren hierbei um die Hauptachse des Torus aufgrund der Hallkomponente der Ionenwindkraft.

Der erste Teil beschäftigt sich mit der Reaktion von kompakten Staubwolken auf eine externe Modulation, wenn selbsterregte Staubdichtewellen vorliegen und auch ohne Wellenaktivität in kleinen Staubwolken. Der Schwerpunkt liegt auf der Fragestellung, ob die Staubdichtewelle durch die externe Modulation synchronisiert werden kann und wie sich die Modulation auf die räumliche Ausbreitung der Welle auswirkt. Es wurde gefunden, dass eine "Sloshing" und "Stretching" Bewegung der gesamten Staubwolke bei niedrigen Frequenzen angeregt werden kann. Diese zeigen ein resonanzartiges Verhalten. Die Staubdichtewelle in großen Staubwolken kann in einem bestimmten Frequenzbereich auf der Grundfrequenz der externen Modulation synchronisiert werden. Es ist außerdem eine subharmonische und superharmonische Synchronisation beobachtet worden. Darüber hinaus konnte die dreidimensionale Struktur der Staubdichtewelle mit Hilfe der externen Modulation rekonstruiert werden. Die Dispersionsrelation der Staubdichtewelle in einer finiten Staubwolke ist gemessen worden. Es zeigte sich eine unterschiedliche Gruppen- und Phasengeschwindigkeit der Staubdichtewellen sowie eine Cutoff-Frequenz für den Grenzwert der langen Wellenlängen. Die Dispersionsrelation kann mit einer Wellenleitertheorie, welche Randeffekte der Staubwolke berücksichtigt, beschrieben werden.

Der Schwerpunkt des zweiten Teils liegt auf dem Verständnis zur Bildung von torusförmigen Staubwolken. Eine systematische Variation der Entladungsparameter wurde durchgeführt, um einen Überblick über das generelle Verhalten der Torusbildung zu erlangen. Der Einschluss und die Rotation der Partikel werden in einem hierarchischen Einzelteilchenmodell beschrieben. Die Kräfte unterteilen sich hierbei in radiale und azimutale Komponenten. Die radialen Kraftkomponenten der elektrischen Feldkraft und der Ionenwindkraft bestimmen die Einschlussbedingung des Torus. Deren Ergebnis stimmt gut mit dem beobachteten Durchmesser des Voids überein. Die azimutalen Komponenten der Ionenwindkraft, welche durch die Lorentzkraft hervorgerufen wird, und der Gravitationskraft bestimmen das Einsetzen der Rotation von Partikeln. Dabei definiert die Gravitationskraft einen Schwellwert, der von der Ionenwindkraft überschritten werden muss. Während die Geschwindigkeiten von dem Modell noch überschätzt werden, ist die allgemeine Variation der Geschwindigkeiten entlang des Torus in guter Übereinstimmung.

Abstract

In this thesis, two different dynamical situations of dust clouds in a weakly magnetized anodic plasma are studied. The dust clouds are confined by an equilibrium of the electric field force and the ion drag force. It is distinguished between compact and torus-shaped dust clouds. In compact dust clouds, dust-density waves, which are excited by streaming ions, can be observed, and the compact dust clouds are further classified by the ratio of their length and a typical wavelength. For the torus-shaped dust clouds, a dust-free region, which is termed "void", is found, and the dust particles rotate about the major axis of the torus due to the Hall component of the ion drag force.

The first part deals with the response of compact dust clouds to an external modulation, when self-excited dust-density waves are present and with no wave activity in small dust clouds. The focus lies upon the question, if the dust-density wave can be synchronized by the modulation, and how the modulation affects the spatial propagation of the wave. It is found that a sloshing and stretching motion of the entire dust cloud can be excited at low frequencies, showing a resonance-like behavior. The dust-density wave in large dust clouds can be synchronized at the fundamental frequency of the external modulation within a specific frequency range, but also subharmonic and superharmonic synchronization is observed. Furthermore, the three-dimensional structure of a dust-density wave is reconstructed with the aid of the external modulation. The dispersion relation of dust-density waves within a finite dust cloud was measured revealing differing group and phase velocity of the wave and a cutoff frequency for the long wavelength limit. The dispersion relation can be described by a cylindrical waveguide theory, which includes boundary effects of the dust cloud.

The second part is focused on the understanding of the formation of torus-shaped dust clouds. Therefore, a systematic variation of the discharge parameters was performed to gain an overview on the general behavior of the formation process. The confinement and the rotation of dust particles are described in terms of a hierarchical single-particle model. The forces are divided into radial and azimuthal components. The radial force balance of electric field force and ion drag force describes the confinement condition of the torus and agrees well with the observed diameter of the void. The azimuthal component of the ion drag force, which is caused by the Lorentz force, and the gravitational force are accountable for the onset of the particle rotation, where the gravitational force defines a threshold that has to be exceeded by the ion drag force. While the velocity is still overestimated by this model, the general variation of the velocity distribution along the torus is well described.

Contents

1 Introduction

A dusty or complex plasma consists of electrons, ions, neutrals and macroscopic dust particles of nanometer up to micrometer size. Complex plasmas naturally occur in the environment of the interstellar medium [1], they play a role in technological plasma processes [2–5] and in fusion research [6–9]. The interest in fundamental research on complex plasmas has quickly arisen after the discovery, in 1994, of so-called plasma crystals [10–14]. In a plasma crystal, dust particles arrange themselves in a regular order. The advantage of this system is that the interaction of dust particles can be investigated on a microscopic level with a comparably simple setup consisting of a laser beam and a video camera. Furthermore, it is interesting to note that the plasma crystals show similarities to Coulomb crystals of colloidal suspensions [15–17] and of ions in particle traps [18–21].

In the beginning of the research on complex plasmas, the main focus laid on the structure of the plasma crystals [22–24], but also their dynamics like melting [24–26], Mach cones [27–31] and wave activity [32–40] were of interest. A special formation of plasma crystals are finite dust clouds with a small number of dust particles. These cluster can be ordered in a two-dimensional plane [41, 42] or in a three-dimensional nested shell structure, i.e., so-called Coulomb balls (aka Yukawa balls) [43, 44]. The investigations on the two-dimensional dust clusters cover their structure [41, 42, 45], eigenmodes [46, 47] and a forced rotation of the cluster [48–51]. The rotation of the cluster can be achieved either directly by applying a laser manipulation [48] or indirectly by the effect of a weak magnetic field, which induces a torque of the ion drag force (Lorentz force) on the dust particles [49–51].

Typical plasma crystals are levitated in the sheath of a radio-frequency (rf) plasma, because the large gravitational force can only be balanced by the electric field force in the sheath, where the electric field is strong enough. This limitation can be overcome by using nanometer-sized particles [52, 53], performing experiments under microgravity conditions [54, 55] or by applying an additional force (thermophoretic force) [56]. Then, the dust particles can fill the bulk plasma. Surprisingly, it was found that the central region remains dust-free, i.e., a "void" appears. The first observation of a void was reported for experiments with nanometer-sized particles [52], and later in microgravity experiments [54, 57] for micrometer-sized particles. The explanation for the formation of a void is an outward-streaming ion flow that exerts an ion drag force onto the dust particles and pushes them out of the central region until an inward-directed electric field force counterbalances the ion drag force [54, 57]. Recently, a closure of this void could be realized at low discharge power [58], and was also studied by means of simulations [59].

The described ordering of dust particles in a plasma crystal occurs when the thermal energy of the particles is small compared to the electrostatic interaction

between the dust particles, which are then called strongly coupled. On the other hand, for a weaker coupling of the dust particles, the particles behave rather like a fluid. A specific observation in a weakly coupled system are dust acoustic waves [60–65]. These waves are self-excited compressional waves, which take their energy from streaming ions [66,67]. In this thesis, the term "dust-density wave" will be used, which is more general. For the understanding of these waves the experiments have to be compared with theoretical approaches that range from fluid theories [60,68–71] to kinetic theories [66, 72, 73] including several effects like charge variation [69, 74–77], boundary effects [68, 70, 71], and a finite temperature of the dust particles [73]. Therefore, the dispersion relation, i.e., the relation between the angular frequency ω of the wave and the wavenumber k, is commonly measured. A suitable method is to apply an external modulation [78–82], and measure the wavenumber depending on the external frequency. Although this method was successfully used, the mechanism behind a synchronization due to the external modulation is still an unknown issue.

The synchronization of oscillating systems caused by an external force is well known and widely studied in nonlinear dynamics [83–87]. The simplest model of a driven oscillator is the damped harmonic oscillator. Due to the external forcing, the periodical motion of this oscillator is defined by the properties of the external driver after a transient behavior. Nevertheless, this type of oscillator does not provide the ability to interact with the external modulation. A special need for an interaction of an oscillating system is that the oscillator has to be self-excited. This feature is an intrinsic property of, for example, the parametric oscillator and the van der Pol oscillator. For instance, an external modulation of the van der Pol oscillator leads to a couple of differing oscillating states like harmonic synchronization at the fundamental of the eigenfrequency, sub- and superharmonic synchronization for multiples of the eigenfrequency, quasiperiodic oscillations, and an incomplete synchronization, where the phase as well as the amplitude of the oscillator varies periodically. On the other hand, the parametric oscillator also provides sub- and superharmonic regions where the wave is excited, but the common behavior is not as complex as it is for the van der Pol oscillator. Therefore, the investigation of the synchronization of self-excited dust-density waves opens an interesting branch of the dynamical properties of these waves.

In the field of complex plasmas only a few works [82,88,89] addressed the question of the synchronization of dust-density waves. The synchronization of the self-excited dust-density wave was recently investigated in Ref. [82] in terms of an "amplification" of the wavenumber that corresponds to the external modulation frequency. It was found that it is possible to synchronize the dust-density wave, when the wavenumber lies within the natural spectrum of wavenumbers of the self-excited wave.

In this thesis, two different dynamical situations of the particle motion are addressed. The first topic is focused on self-excited dust-density waves and the effect of an external modulation with respect to synchronization. The purpose is to gain a better understanding of the influence of the external modulation on the dust-density wave. Therefore, the response is studied both in the frequency domain and with respect to its spatial properties. The second topic addresses the formation of torus-shaped

dust clouds. There, the phenomenon of void formation in the presence of a magnetic field and the origin of the particle streaming motion are interesting novel aspects. In particular, two basic questions arise: First, is the principle void mechanism similar to the voids in rf plasmas, and second, is the streaming of dust particles related to the ion drag force, since the dust particles are not directly affected by the magnetic field. Finally, is it possible to combine both questions within the same model?

The present work is a cumulative thesis and structured as follows: A brief introduction regarding the physics on complex plasmas and the experimental setup, including a description of the anodic plasma and the structure of trapped dust clouds, is given in Chap. 2. For the understanding of the synchronization of dust-density waves, a short introduction about aspects of synchronization obtained in nonlinear dynamics is presented in Chap. 3. The experiments on the external modulation of dust clouds are discussed in Chap. 4, and the formation of torus-shaped dust clouds is studied in Chap. 5. A summary is given in Chap. 6.

2 Properties of Dust Particles in a Plasma

For studying the dynamics or the interaction of dust particles in a plasma, it is necessary that these particles are confined within the plasma. Furthermore, the understanding of the confinement of the dust particles itself is of interest, which is intimately related to the understanding of the acting forces on a dust particle. In this Chapter, a brief introduction into the physics of dust particles in a plasma is presented. For a more detailed description, the reader is referred to textbooks [90–93] and review articles [94–96].

In Sec. 2.1 a general description of the basic aspects of charging of dust particles and the forces acting on a dust particle in a plasma is given. The specific details regarding the situation in an anodic plasma is presented in Sec. 2.2. There, a short introduction of the experimental setup, the properties of an anodic plasma, and the confinement of a dust cloud is described. In the last Section the main aspects are summarized.

2.1 Basic Description of a Dusty Plasma

The intention of this Section is to provide a brief description of the theoretical background, which is needed for the discussion of the results obtained in this work.

A basic property of a plasma is its quasineutrality,

$$n_\mathrm{e} - n_\mathrm{i} \ll n_\mathrm{e} \ . \tag{2.1}$$

Here, n_e is the electron density and n_i the density of singly positively charged ions. In good approximation, it is justified to write this relation as $n_\mathrm{e} = n_\mathrm{i}$. When dust particles are immersed in the plasma, they become charged. In laboratory plasmas, the charge of dust particles is mainly defined by the collection of electrons and ions. Due to the higher mobility of electrons, the charge of a dust particle is typically negative, and the quasineutrality reads then as:

$$n_\mathrm{e} + Z_\mathrm{d} n_\mathrm{d} - n_\mathrm{i} = 0 \ . \tag{2.2}$$

Here, Z_d is the number of elementary charges on the dust particles and n_d the density of the dust particles.

The potential of a dust particle with particle charge $q_\mathrm{d} = -Z_\mathrm{d} e$ at radial distance r from its center is described by the Debye-Hückel potential (aka Yukawa or screened Coulomb potential) [90]:

$$\Phi(r) = \frac{q_\mathrm{d}}{4\pi\epsilon_0 r} \exp\left(-\frac{r}{\lambda_\mathrm{D}}\right) \ . \tag{2.3}$$

The typical range of the screening is given by the linearized Debye length

$$\lambda_{\mathrm{D}} = \left(\lambda_{\mathrm{De}}^{-2} + \lambda_{\mathrm{Di}}^{-2}\right)^{-1/2} \tag{2.4}$$

with the electron λ_{De} and the ion Debye length λ_{Di}:

$$\lambda_{\mathrm{De}} = \sqrt{\frac{\epsilon_0 k_{\mathrm{B}} T_{\mathrm{e}}}{n_{\mathrm{e}} e^2}} \ , \quad \lambda_{\mathrm{Di}} = \sqrt{\frac{\epsilon_0 k_{\mathrm{B}} T_{\mathrm{i}}}{n_{\mathrm{i}} e^2}} \ , \tag{2.5}$$

where k_{B} is the Boltzmann constant, T_{e} the electron and T_{i} the ion temperature. In case of streaming ions with ion velocity v_{i}, the ion Debye length is modified by its kinetic energy and the screening is described by an effective screening length [97,98],

$$\lambda_{\mathrm{D,eff}} = \left[\lambda_{\mathrm{De}}^{-2} + \lambda_{\mathrm{Di}}^{-2}\left(1 + \frac{m_{\mathrm{i}} v_{\mathrm{i}}^2}{k_{\mathrm{B}} T_{\mathrm{i}}}\right)\right]^{-1/2} \ . \tag{2.6}$$

For the screening of an object within the plasma, it is necessary that the number N_{D} of electrons and ions within a sphere with radius λ_{De} is comparably large,

$$N_{\mathrm{D}} = \frac{4\pi}{3} n_{\mathrm{e}} \lambda_{\mathrm{De}}^3 \ . \tag{2.7}$$

A plasma is called ideal, when the relation $N_{\mathrm{D}} \gg 1$ is satisfied, which is justified in the pure anodic plasma of the present experiment. However, for a complex plasma this condition is, in general, not fulfilled since the dust system provides the ability of strong coupling.

A different and important quantity of a plasma is its plasma frequency $\omega_{\mathrm{p}l}$ for the electrons, ions and dust particles ($l = \mathrm{e}, \mathrm{i}, \mathrm{d}$):

$$\omega_{\mathrm{p}l} = \sqrt{\frac{n_l q_l^2}{\epsilon_0 m_l}} \ . \tag{2.8}$$

Here, m_l is the mass and q_l the charge of the plasma component. In view of the charge-to-mass ratio, the ordering of the plasma frequencies is given as ω_{pe} (GHz) $\gg$ ω_{pi} (MHz) $\gg$ ω_{pd} (Hz).

2.1.1 Charging of a Dust Particle

In laboratory plasmas, dust particles typically carry a negative charge by initially collecting more electrons than ions until an equilibrium is reached, in which the electron current is reduced by the repulsive field. Other charging mechanisms that can lead to a positive charge are, e.g., photoionization and secondary electron emission [1,92,99]. These charging mechanisms are important for astrophysical plasmas but can be neglected here.

The charge q_{d} of a dust particle with radius r_{d} is calculated by the capacitance model*:

$$q_{\mathrm{d}} = 4\pi\epsilon_0 r_{\mathrm{d}} \Phi_{\mathrm{f}} = C\Phi_{\mathrm{f}} \ . \tag{2.9}$$

*In general: $C = 4\pi\epsilon_0 r_{\mathrm{d}}(1 + r_{\mathrm{d}}/\lambda_{\mathrm{D}}) \approx 4\pi\epsilon_0 r_{\mathrm{d}}$ for $r_{\mathrm{d}} \ll \lambda_D$

The surface potential Φ_f of a dust particle is determined by the floating condition, which is given by the equilibrium of the ion current I_i and electron current I_e reaching the dust particle, $I_\mathrm{i}(\Phi_\mathrm{f}) + I_\mathrm{e}(\Phi_\mathrm{f}) = 0$.

This is a similar problem corresponding to the determination of the probe potential, i.e., floating potential, in probe diagnostics [90, 91, 100]. The first approach describing the currents upon an object in a plasma was given by Mott-Smith and Langmuir [100] in terms of the Orbital Motion Limited (OML) theory.

The electrons can be treated as thermalized. The electron current on a sphere is then described by means of the OML theory as [100]

$$I_\mathrm{e} = -\pi r_\mathrm{d}^2 n_\mathrm{e} e v_\mathrm{e,th} \exp\left(\frac{e\phi_\mathrm{f}}{k_\mathrm{B} T_\mathrm{e}}\right) , \tag{2.10}$$

where $v_\mathrm{e,th} = (8k_\mathrm{B}T_\mathrm{e}/\pi m_\mathrm{e})^{1/2}$ is the mean thermal electron velocity.

Due to an electric field in the present experiment, the ions are streaming, and the OML current of the ions is calculated for a shifted Maxwellian velocity distribution [99],

$$I_\mathrm{i} = \pi r_\mathrm{d}^2 n_\mathrm{i} e v_\mathrm{i} \Bigg[\left(1 + \frac{v_\mathrm{i,T}^2}{2v_\mathrm{i}^2} - \frac{2e\Phi_\mathrm{f}}{m_\mathrm{i} v_\mathrm{i}^2}\right) \mathrm{erf}\left(\frac{v_\mathrm{i0}}{v_\mathrm{i,T}}\right) + \ldots \tag{2.11}$$

$$+ \frac{v_\mathrm{i,T}}{\sqrt{\pi} v_\mathrm{i}} \exp\left(-\frac{v_\mathrm{i}^2}{v_\mathrm{i,T}^2}\right) \Bigg] . \tag{2.12}$$

Here, v_i is the ion drift velocity, m_i the ion mass, $v_\mathrm{i,T} = (2k_\mathrm{B}T_\mathrm{i}/m_\mathrm{i})^{1/2}$, and $\mathrm{erf}(x)$ the error function.

By using the floating condition, $I_\mathrm{e}(\Phi_\mathrm{f}) + I_\mathrm{i}(\Phi_\mathrm{f}) = 0$, an implicit equation for the floating potential Φ_f is obtained that can be numerically solved, and the charge q_d of the dust particle is then calculated by using the capacitance model (2.9) as well.

2.1.2 Forces on a Dust Particle

Force of Gravity: The gravitational force acting on a dust particle reads as follows:

$$\vec{F}_\mathrm{g} = m_\mathrm{d}\vec{g} = \frac{4}{3}\pi r_\mathrm{d}^3 \rho_\mathrm{d} \vec{g} , \tag{2.13}$$

where m_d is the mass of a dust particle with radius r_d and mass density ρ_d, and $\vec{g}$ the gravitational acceleration. The force of gravity is a considerably large force for particles with a radius of some micrometers, while it can be neglected for nanometer-sized particles. In the present experiment, the force of gravity on a dust particle is $F_\mathrm{g} = 0.6 \times 10^{-14}$ N, which is small compared to the total net force of the electric field force and the ion drag force.

Electric Field Force: The electric field force is

$$\vec{F}_\mathrm{el} = q_\mathrm{d}\vec{E} . \tag{2.14}$$

The charge of the particle is estimated with the capacitance model with the electric field $\vec{E}$ ($|E| \approx 200$ V/m). The magnitude of order of the electric field force is of about $F_\mathrm{el} \approx 10^{-13}$ N, and hence considerably larger than the gravitational force.

Neutral Friction Force: In most experiments it is valid to assume that the neutral drag force is a friction force. The force is due to collisions of neutrals with the dust particles. For a moving dust particle with velocity v_d, the force can be written in the following form,

$$F_\mathrm{n} = -m_\mathrm{d}\beta v_\mathrm{d} \ , \tag{2.15}$$

with the Epstein coefficient $\beta = \delta(8/\pi)p(r_\mathrm{d}\rho_\mathrm{d}v_\mathrm{n,th})^{-1}$ [101], gas pressure p, and the thermal velocity of neutrals $v_\mathrm{n,th} = \sqrt{8k_\mathrm{B}T_\mathrm{n}/\pi m_\mathrm{n}}$. The parameter δ is in the range between 1 (for specular reflection) and 1.44 (for diffuse reflection).

Ion Drag Force: The ion drag force on a dust particle was studied analytically [97,102–104], numerically by means of simulations [105,106] as well as experimentally [107–111]. The main task for calculating the ion drag force analytically is to specify an appropriate value for the radial distance between ions and the dust particle up to that the ions still contribute to the ion drag force. The first description [102] used the Debye length, but that led to an underestimation of the ion drag force. This could be improved by choosing the electron Debye length, which results in a larger ion drag force [103]. By now, it is accepted to take a velocity-dependent cutoff [104]. Moreover, the influence of collisions on the ion drag force is still an active topic of research [112–115].

The ion drag force F_i is composed of a collection part F_c and an orbital part F_o,

$$F_\mathrm{i} = F_\mathrm{c} + F_\mathrm{o} \ . \tag{2.16}$$

The collection part is caused by the momentum transfer of ions directly hitting the dust particle, and the orbital part is due to the momentum transfer of scattered ions by the Coulomb interaction.

The OML collection force for a shifted Maxwellian distribution of the ion velocity is given by

$$F_\mathrm{c} = n_\mathrm{i} r_\mathrm{d}^2 m_\mathrm{i} v_\mathrm{i,T}^2 \frac{\sqrt{\pi}}{2u^2} \Bigg\{ u(2u^2+1+2\chi)\mathrm{e}^{-u^2} + \quad \ldots \\ + \left[4u^4+4u^2-1-2(1-2u^2)\chi\right] \frac{\sqrt{\pi}}{2}\mathrm{erf}(u) \Bigg\} \ . \tag{2.17}$$

Here, $u = v_\mathrm{i}/v_\mathrm{i,T}$ is the normalized flow velocity of the ions and $v_\mathrm{i,T} = \sqrt{2k_\mathrm{B}T_\mathrm{i}/m_\mathrm{i}}$ the thermal ion velocity. The normalized potential is given by $\chi \equiv -e\phi_\mathrm{f}/k_\mathrm{B}T_\mathrm{i}$.

An analytical expression for the ion drag force for superthermal ions was given by Daugherty and Graves [116],

$$F_\mathrm{o}(v_\mathrm{i}) = \frac{2n_\mathrm{i}m_\mathrm{i}}{v_\mathrm{i}v_\mathrm{i,T}\sqrt{\pi}} \int_0^\infty \sigma(v) v^3 \exp\left(-\frac{v^2+v_\mathrm{i}^2}{v_\mathrm{i,T}^2}\right) \times \ldots \tag{2.18}$$

$$\times \left[\cosh\left(\frac{2v_\mathrm{i}v}{v_\mathrm{i,T}^2}\right) - \frac{v_\mathrm{i,T}^2}{2v_\mathrm{i}v}\sinh\left(\frac{2v_\mathrm{i}v}{v_\mathrm{i,T}^2}\right)\right] \mathrm{d}v \ . \tag{2.19}$$

Herein, the cross-section for Coulomb scattering is given by

$$\sigma(v) = 4\pi\rho_0(v)^2\Lambda(v) \tag{2.20}$$

with $\rho_0(v) = -q_\mathrm{d}e/4\pi\epsilon_0 m_\mathrm{i}v^2$ and the Coulomb logarithm $\ln\Lambda(v)$ [104].

For the Coulomb logarithm $\ln\Lambda$ the expression from Khrapak *et al.* [104] is used:

$$\ln\Lambda = \ln\left(\frac{b_{90}+\lambda_\mathrm{s}}{b_{90}+r_\mathrm{p}}\right) \ , \tag{2.21}$$

where $b_{90} = r_\mathrm{d}e\phi_\mathrm{f}/m_\mathrm{i}v_\mathrm{i}^2$ is the impact parameter for 90° scattering in Coulomb collisions and $\lambda_\mathrm{s}^2 = r_\mathrm{d}^2 + \lambda_\mathrm{De}^2/[1+2k_\mathrm{B}T_\mathrm{e}/m_\mathrm{i}v_\mathrm{i}^2]$ the effective Debye length.

Hutchinson [105] studied the ion drag force numerically with a particle-in-cell code. For comparison, the following analytical expression for the orbital part F_o was used [105]:

$$F_\mathrm{o} = n_\mathrm{i}\frac{q_\mathrm{i}^2\phi_\mathrm{f}^2}{m_\mathrm{i}v_\mathrm{i,T}^2}r_\mathrm{d}^2 8\pi G(u)\ln\Lambda \ , \tag{2.22}$$

where $G(u) \equiv [\mathrm{erf}(u) - 2ue^{-u^2}/\sqrt{\pi}]/(2u^2)$ is the Chandrasekhar function [117]. A good agreement between the analytic expressions and the simulations was found, when the following expression for an effective drift velocity v_eff [105] is taken:

$$\begin{aligned} m_\mathrm{i}v_\mathrm{eff}^2 =& 2k_\mathrm{B}T_\mathrm{i} + m_\mathrm{i}v_\mathrm{i}^2 \times \quad \ldots \\ &\times\left\{1+\left[\frac{v_\mathrm{i}/\sqrt{k_\mathrm{B}T_\mathrm{e}/m_\mathrm{i}}}{0.6+0.05\ln(M)+(\lambda_\mathrm{De}/5r_\mathrm{d})(\sqrt{k_\mathrm{B}T_\mathrm{i}/k_\mathrm{B}T_\mathrm{e}}-0.1)}\right]^3\right\} \ , \end{aligned} \tag{2.23}$$

M being the ion mass in units of hydrogen mass.

The ion drag force acts along the direction of the ion flow, which is determined by the stationary equation of motion,

$$m_\mathrm{i}\nu_\mathrm{in}\vec{v}_\mathrm{i} = e\left(\vec{E}+\vec{v}_\mathrm{i}\times\vec{B}\right). \tag{2.24}$$

Here, ν_in is the ion-neutral collision frequency. For a homogeneous magnetic field $\vec{B} = (0,0,B)$, the ion drift velocity is then given by

$$\vec{v}_\mathrm{i} = \begin{pmatrix} \frac{1}{1+\mu^2B^2} & \frac{\mu B}{1+\mu^2B^2} & 0 \\ -\frac{\mu B}{1+\mu^2B^2} & \frac{1}{1+\mu^2B^2} & 0 \\ 0 & 0 & 1 \end{pmatrix} \mu\vec{E} \tag{2.25}$$

with $\mu = e/m_\mathrm{i}\nu_\mathrm{in}$ being the mobility of ions. The mobility of argon ions in their parent gas was experimentally determined by Frost [118],

$$\mu(E,p) = \bar{\mu}\frac{p_0}{p}\left(1+A\frac{E}{p}\right)^{-\frac{1}{2}} \ , \tag{2.26}$$

with $\bar{\mu} = 0.146\ \mathrm{m^2/Vs}$, $p_0 = 133\ \mathrm{Pa}$ and $A = 0.035\ \mathrm{Pa\ m/V}$.

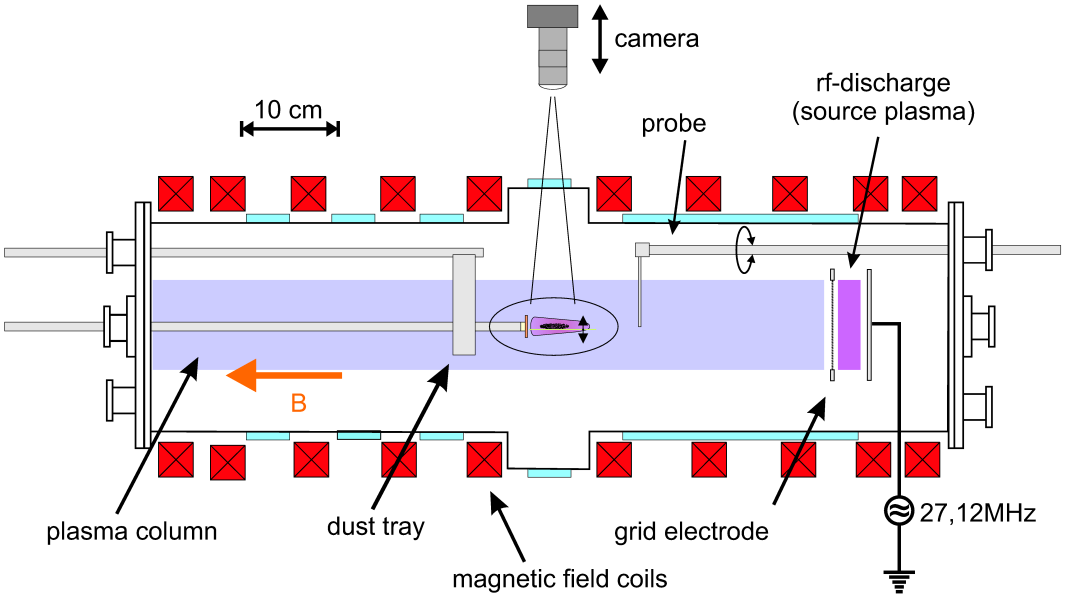

Figure 2.1: Sketch of the Matilda-II device.

Due to the axial magnetic field, the matrix describing the ion flow contains off-diagonal elements. These elements lead to a curvature of the ion flow, i.e., an ion velocity component $v_{\mathrm{i},\varphi}$ pointing in azimuthal direction. Depending on the strength of the magnetic field, this component is only about a few percent for a weak magnetic field, as it is in the present experiment, or dominates the ion motion at high magnetic fields. Then, the ions become magnetized and are mainly streaming in axial direction with a helical shape of the ion flow. The decomposition of the ion drag force into its components is needed for the understanding of the formation of the torus-shaped dust clouds.

2.2 The Anodic Plasma

In this Section, a brief description of the experiment, the plasma parameters, and the confinement of dust particles in an anodic plasma is given.

2.2.1 Experimental Setup

The experiments were performed in the Matilda-II setup, which is sketched in Fig. 2.1. The typical magnetic field strength was about $B = 20$ mT for the investigations on the dust-density waves, and the parameter study on torus-shaped dust clouds was performed within a range of $B = (5{-}150)$ mT. The experiments were performed in argon gas at a gas pressure of about $p = (3{-}8)$ Pa. An rf source plasma was produced at typical power of $P_{\mathrm{rf}} = 1$ W and $P_{\mathrm{rf}} = 3$ W for the observation of the dust-density waves and the torus-shaped dust clouds, respectively.

The anodic plasma, i.e., a dc plasma, is generated in front of a stainless-steel disk with a diameter of $d = 30$ mm, which is referred to as anode. The anode is positively

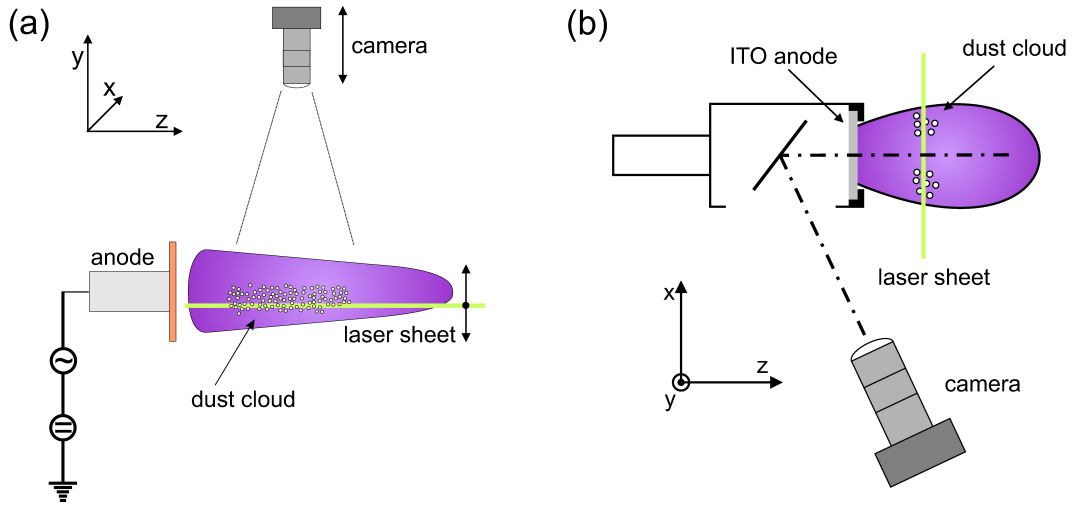

Figure 2.2: Enlarged views of the anode and the observation geometry. For clarification, the used coordinate system are shown in both sketches. (a) The stainless-steel anode is driven with a dc voltage, and for an external modulation a sinusoidal ac voltage can be superimposed. The dust particles are illuminated by a horizontal laser sheet (x−z plane), and the scattered light is recorded with a camera located at the top section. (b) Setup of the indium-tin-oxide (ITO) anode. The dust particles are illuminated by a vertical laser sheet (y−x plane), and the scattered light is recorded via a mirror behind the ITO anode.

biased at voltages of $U_\mathrm{A} = (60{-}90)$ V [$I_\mathrm{A} = (5{-}14)$ mA]. For an external modulation of a dust cloud, a sinusoidal signal of $\Delta U_\mathrm{A} = 10$ $\mathrm{V_{pp}}$ can be superimposed on the dc bias.

The plasma parameters can be measured with an emissive probe and a cylindrical Langmuir probe. The probes are axially movable and rotatable, thus a two-dimensional profile can be measured assuming rotational symmetry. Typical plasma parameters are density $n_\mathrm{e} = 10^{15}$ $\mathrm{m^{-3}}$, electron temperature $T_\mathrm{e} = 3$ eV and ion temperature $T_\mathrm{i} = 0.1$ eV.

The temperature of the ions exceeds the neutral gas temperature T_n due to a drift motion of the ions within an electric field that leads to ion heating [79, 119]:

$$T_\mathrm{i}(v_\mathrm{i}) = T_\mathrm{n} + \frac{\pi - 2}{6}\frac{1}{k_\mathrm{B}} m_\mathrm{i} v_\mathrm{i}^2 \ . \tag{2.27}$$

The dust particles (melamine formaldehyde) used in the experiments were spherical and monodisperse with a diameter of $d_\mathrm{d} = (0.97 \pm 0.05)$ μm [120]. For the observation of the dust particles, they were illuminated by a horizontal laser sheet ($\lambda = 532$ nm, $P = 200$ mW), and the scattered light was recorded at right angle with a camera located at the top section of the experiment, as sketched in Fig. 2.2 (a) along with the used coordinate system. Here, the x- and the z-coordinates span the horizontal observation plane, where the x-direction is orientated parallel to the anode disk, and the z-direction coincides with the magnetic field direction. The y-direction defines the vertical scanning direction. Most results were obtained with this horizontal observation geometry, where the anodic plasma is generated by the stainless-steel anode.

For the torus-shaped dust clouds, a radial section would be desirable. This could be achieved by using an indium-tin-oxide coated glass disk (ITO anode). This electrode is transparent but also electrically conducting. By placing a mirror behind the ITO anode, a dust cloud can now be observed in axial direction [121]. The setup with the ITO anode is sketched in Fig. 2.2 (b) together with the used coordinate system. The ITO anode has an exposed diameter of the conducting material of $d = 26$ mm.

2.2.2 Basic Properties of the Anodic Plasma

In this Section, the main characteristics of the anodic plasma are reported. The first comprehensive study on such type of discharge was performed by Malter, Johnson and Webster [122]. Their work describes the principle behavior of low pressure arcs and gives a classification of the observed discharge modi.

Depending on the anode voltage, the anodic discharge is divided in three modes: The anode-glow mode at low voltages, the ball-of-fire mode and the temperature-limited mode, where a constant anode current for increasing anode voltage is found.

For the anode-glow mode, the plasma production only takes place in the small region of the Debye sheath in front of the anode surface, where the electric field is strong enough to accelerate the electrons to high thermal velocity, and a faint glow close to the anode surface can be found [122–124].

In the ball-of-fire mode, the plasma is generated in an expanded volume in front of the anode. The shape of the plasma is spherical and forms a ball, when no magnetic field is present [122, 125, 126]. If a uniform magnetic field is applied, the ball is stretched in direction of the magnetic field lines, and forms an elongated plasma glow, which is referred to as "firerod" [127]. The present experiments were performed in the ball-of-fire mode.

The temperature-limited mode is characterized by a constant anode current with increasing anode voltage. In this regime, the ionization within the volume is not further increased with rising anode voltage. The term "temperature-limited" has its origin from the thermionic discharge, where the maximum electron current depends on the temperature of the emitting material, e.g., tungsten or tantalum filaments. The limitation of the anode current in this experiment is determined by the ambient source plasma. Thus, the maximum value of the anode current depends on the external discharge parameters, e.g., an increase of the rf power of the source plasma leads to an increase of the anode current as well.

A phenomenon in current carrying discharges is the development of "double layers" [128, 129] due to the preference of a plasma to screen electric fields. Double layers describe a thin region, where a large potential drop of a few volts within a small distance occurs. This potential drop arises due to counterpropagating flows of electrons and ions along an electric field. The double layers are located at the boundary of a plasma region and a sharp boundary of the plasma glow is observed. In anodic plasmas, these double layers were verified and studied [126, 127], and dust clouds could be confined within an anodic plasmas that supports double layers [130]. Nevertheless, in the present setup at the used discharge parameters no double layers

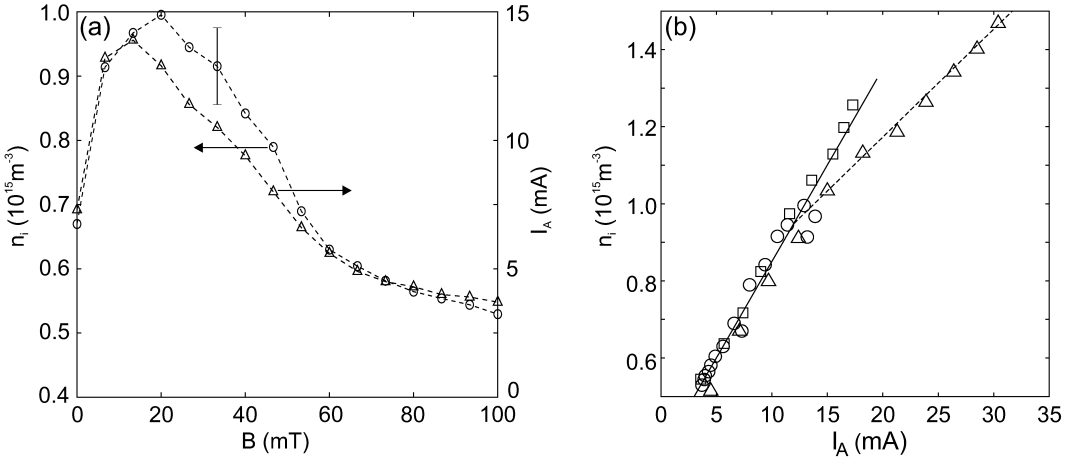

Figure 2.3: (a) The measured ion density n_i (circles) and the anode current I_A of the discharge (triangles) are plotted vs. the magnetic field strength. A non-monotonous dependence of the magnetic field on the ion density with a maximum at $B \approx 20$ mT is found. (b) The ion density is plotted vs. the anode current for a variation of the magnetic field strength (circles), the anode voltage (squares), and the rf power (triangles). Additionally, lines of best fits are shown for low anode currents (solid line) and higher anode voltages (dashed line). A close correlation between the anode current and the ion density is found. (Adapted from Ref. [131])

are detected. However, a discharge mode that supports these double layers can be achieved by changing the discharge parameters [79].

For the understanding of the confinement of dust particles, it is necessary to know the plasma parameters of the anodic plasma. The two-dimensional measurements of the plasma potential [see Appendix B.2, Fig. 7 and Fig. 2.4 (a)] have revealed a convex curvature of the plasma potential, where the electric field close to the central axis points in axial direction. For distances larger than 5 mm away from the central axis, a sufficiently large electric field in radial direction is apparent.

The ion density in the central region of the anodic plasma was measured with a Langmuir probe. For a characterization of the anodic plasma, the ion density was determined depending on the discharge parameters, i.e., anode voltage, rf power and magnetic field strength [131]. In Fig. 2.3 (a) the behavior of the ion density depending on the magnetic field is shown. In this diagram, the ion density n_i as well as the variation of the anode current I_A is plotted vs. the magnetic field strength B. A non-monotonous influence of the magnetic field strength on the ion density is found with a maximum at $B \approx 20$ mT. The similarity between the general behavior of the anode current and the ion density implies a correlation between both.

In Fig. 2.3 (b) the ion density for different discharge parameters is plotted vs. the discharge current. Here, the parameter variation of the magnetic field strength (circles), the anode voltage (squares), and the rf power (triangles) are shown. It is found that the ion density depends linearly on the anode current for low anode currents (solid line). For the variation of the rf power a knee at an anode current of about $I_\mathrm{A} \approx 15$ mA is found. There, the ion density can be described by a straight line

with lower slope (dashed line). Hence, the anode current is a good approximation of the ion density.

2.2.3 Confinement of Dust Particles in an Anodic Plasma

A first estimate of the confining forces on dust particles in an anodic plasma was given by Barkan and Merlino [130]. They have studied a spherical dust cloud confined in the double layer of the anodic plasma. Based on the measurement of a two-dimensional plasma potential, the forces acting upon a particle were calculated. In that experiment polydisperse dust particles were used, whereas the averaged radius of the particles was determined as $r_\mathrm{d} = 5\ \mu$m. In this case, the equilibrium of gravitational force and electric field force was deduced for the confinement of the dust cloud. Additionally, the influence of a neutral gas drag and the ion drag force on the dust particles were discussed.

In contrast, the confinement of dust particles in the present anodic plasma is defined by a force equilibrium of the electric field force and the ion drag force [79,98]. The electric field, as described in Sec. 2.2.2, points away from the anode, so that the electric field force, acting on the negatively charged particles, points towards the anode. Hence, the dust particles are attracted to the anode. The ions are flowing along the electric field lines, and therefore, the ion drag force F_i on the dust particle is opposed to the electric field force F_el. Due to the small dust particles, the force of gravity is small compared to the above mentioned forces, and hence, negligible for the confinement of dust particles.

The model described by Trottenberg *et al.* [79,98] is more sophisticated compared to a determination of the force equilibrium of a dust particle. Here, the confinement potential was calculated along the central axis. The radial confinement was supposed to be due to the high electric fields in radial direction that act as a barrier for the dust particles. A non-conservative trap potential energy W was derived from the total net force $F = F_\mathrm{i} + F_\mathrm{el}$. The ion drag force was determined following the approach of Daugherty and Graves [116], see Eq. (2.18).

A force equilibrium of the electric field force and the ion drag force was found at an electric field strength of about $E \approx 200$ V/m. For smaller electric fields, the ion drag overcomes the electric field force and vice versa. In Fig. 2.4 (a) a measurement of the two-dimensional plasma potential is shown. The corresponding forces acting on a dust particle and the resulting axial confinement potential are given in Fig. 2.4 (b). The calculated potential well (thick solid line) has a minimum close to 20 mm, and the region, where dust can be confined (hatched region), is found to agree very well with the observed location of the dust cloud, shown in Fig. 2.4 (a).

The model in Refs. [79,98] is a good basis for the understanding of the confinement of dust particles in an anodic plasma. It has turned out that the responsible forces are the electric field force and the opposing ion drag force. The radial confinement is due to the high radial electric fields.

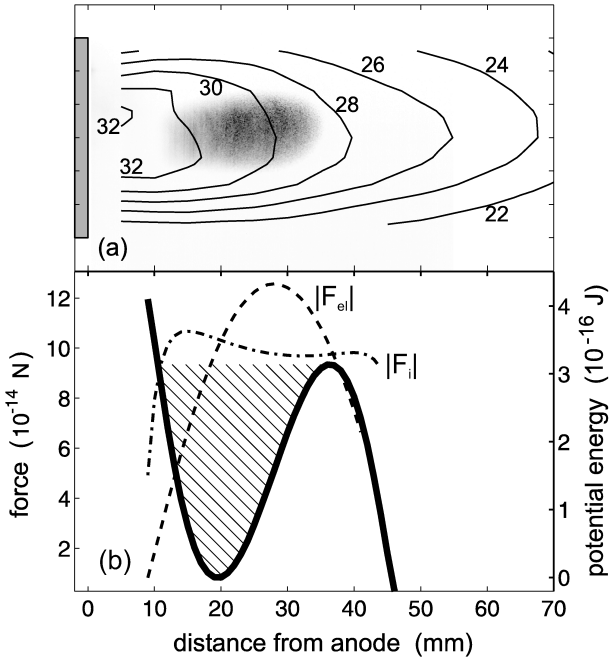

Figure 2.4: (a) A two-dimensional diagram of the plasma potential is shown. On the left-hand side the anode is placed, and the location of a dust cloud is indicated. (b) The calculated forces of the electric field force (dashed line) and the ion drag force (dashed-dotted line) are plotted vs. the axial distance from the anode. The confinement potential (solid thick line), resulting from the force balance of these forces, is shown, and the region, where dust particles can remain, is indicated by the hatched region. (Adapted from Ref. [79])

Overview on Observed Dust Clouds

Before the specific details of the investigations are described, first, an overview of the observed dust clouds and their general structure is given. In Fig. 2.5, snapshots of the dust clouds are shown. The snapshots (a)-(c) were taken in the horizontal section representing the $x-z$ plane; whereas image (d) was taken in the vertical section, and the plasma was generated in front of the ITO anode.

At first glance, the dust clouds can be divided into compact dust clouds [Fig. 2.5 (a)-(c)] and torus-shaped dust clouds [Fig. 2.5 (d)]. In case of the torus-shaped dust cloud, the particles are arranged in a ring-like structure with the ring plane orientated parallel to the anode surface. A dust-free region, i.e., the void, is clearly visible. The dust particles are not at rest, rather, they rotate about the torus axis in clockwise direction with a higher velocity on the downward-streaming branch (in direction of gravity) than on the upward-streaming one (against direction of gravity), as can be conjectured from the imaging of the dust particles. On the left-hand side, the shape of a dust particle is point-like, whereas, on the right-hand side, the dust particles appear streak-like due to a displacement of the dust particles during the exposure time of the camera. The details of the torus-shaped dust clouds are described in Sec. 5 in terms of the experimental results and a hierarchical

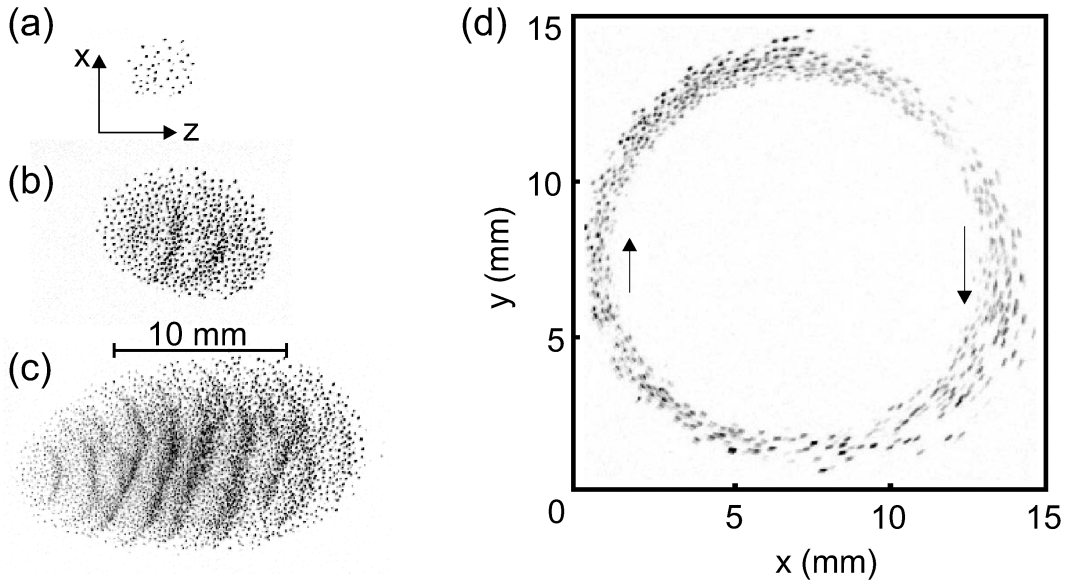

Figure 2.5: Snapshots of observed dust clouds. A horizontal section ($x-z$ plane) is shown for compact dust clouds of varying sizes: (a) small, (b) medium-sized and (c) large dust clouds. Self-excited dust-density waves are found in medium-sized and large dust clouds, whereas no wave activity is observed in a small dust cloud. (d) The snapshot of the torus-shaped dust cloud was taken in the vertical observation geometry using the ITO anode. The dust particles are streaming in clockwise direction with a higher velocity at the down-streaming branch than at the up-streaming one.

single-particle model.

The compact dust clouds are further divided into (a) small, (b) medium-sized, and (c) large dust clouds. This classification refers to the observation that in medium-sized and large dust clouds self-excited dust-density waves emerge. Therefore, the clouds are specified by the ratio of cloud length d and wavelength λ of a typical dust-density wave:

(a) $d < \lambda$: small,

(b) $d \gtrsim \lambda$: medium-sized,

(c) $d \gg \lambda$: large.

The small dust cloud is nearly spherical in shape with a diameter of about 4 mm. The medium-sized dust cloud has an elliptical shape with a length of about 8 mm, and two wave crests can be recognized. Both the small and the medium-sized dust cloud are not centered on the anode axis but are shifted downward in vertical direction, i.e., in the direction of the gravitational force. This vertical shift is related to the observation of the torus-shaped dust cloud with a void in the center. It is suggested that the ion drag force on the dust particle is responsible for the shift because the force of gravity is of second order. In contrast, the large dust cloud is aligned with the central axis of the anode. The cross-section of the cloud is elliptical but in

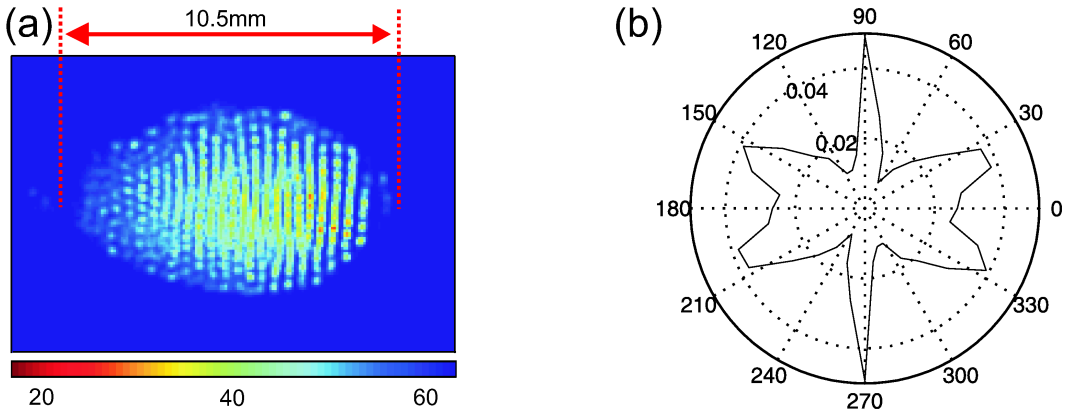

Figure 2.6: (a) A phase-synchronous averaged frame at vertical position $y = -3$ mm and (b) the bond orientational order determined by an average of 100 single images. A pronounced alignment in stripes perpendicular to the magnetic field is found. The bond-orientational order reveals a mixture of fourfold and sixfold symmetry.

vertical direction the dust cloud is stretched in electric field direction. Furthermore, several wave crests are well reproduced.

A vertical scan through an externally modulated dust cloud of medium size (see Appendix B.1, Fig. 3) has revealed a kind of crystalline or rather an ordered state at the top section of the dust cloud. For lower positions, wave activity is found. In Fig. 2.6 (a), a phase-synchronous averaged image of the dust cloud at vertical position of $y = -3$ mm is shown. In this figure, a clear preference to an alignment of particles perpendicular to the magnetic field direction is found. In the central region the strips of particles are more disturbed compared to the boundary region of the cloud, resulting in a blurred region due to the time-averaging.

The ordering of the particles can be analyzed in more detail by calculating the bond-orientational order angle θ_{ij} of next neighbors. The angle is defined by

$$\theta_{ij} = \arctan\left(\frac{z_i - z_j}{x_i - x_j}\right) \quad , \tag{2.28}$$

where (x_i, z_i) denotes the position of the particle i. The particles included for the calculation have a distance of less than 130 % of the average interparticle distance. A histogram

$$h(\theta)\Delta\theta = \sum_{i=1}^{N} \sum_{i \neq j} \delta(\theta - \theta_{ij})\Delta\theta \tag{2.29}$$

was calculated by an average over 100 frames and normalized to unity.

In Fig. 2.6 (b), the histogram is shown as a polar diagram. Sharp peaks at angles of 90° and 270° are found, which is the orientation perpendicular to the magnetic field. There are four other lobes present, whereas the histogram at angles of 0° and 180° does not vanish. Hence, the particles are ordered in a mixture of fourfold and sixfold symmetry with a preferred alignment of particles in stripes perpendicular to the magnetic field direction. It is suggested that the ordering in stripes perpendicular

to the magnetic field can be explained by a slow rotation of the dust cloud, thus a preference to an arrangement in "flow"-direction exist.

Details of the external modulation of these compact dust clouds are given in Chap. 4.

2.3 Summary

In this Chapter, the basics of the confinement of dust particles in an anodic plasma were briefly described. The confinement of the dust particles is well understood in terms of a force equilibrium of the ion drag force and the electric field force. The gravitational force is negligible for the confinement.

The ion density can be approximated by the magnitude of the anode current, and it is found that the ion density varies according to a variation of the magnetic field in a non-monotonous behavior. The presence of the magnetic field also gives rise to a small azimuthal component of the ion flow.

Besides the compact dust clouds, torus-shaped dust clouds are observed which emerge due to the magnetic field. The compact dust clouds are studied regarding self-excited dust-density waves and the response to an external modulation. The results will be presented in Chap. 4. The properties of the torus-shaped dust clouds will be described in more detail in Chap. 5.

3 Synchronization of Oscillating Systems

The periodic motion of an oscillating system and its dynamical evolution in time and space is a general problem in a large variety of physical systems. Of specific interest is the interaction of such systems with others of the same kind or with an external modulation that is applied to achieve control of the system.

In this Chapter, a brief description of the synchronization of dynamical systems is presented. The intention of this Chapter is to introduce basic aspects of synchronization*. For a comprehensive discussion, the reader is referred to textbooks of nonlinear dynamics [83–87, 132].

A general definition of synchronization can be given as follows [84]:

> "Synchronization is an adjustment of the time scales of oscillations due to interaction between the oscillating processes."

This statement includes three basic aspects: First, synchronization is a phenomenon of oscillating systems. Second, it is an interaction of at least two oscillators. Third, due to this interaction, the time (or spatial) scales, i.e., frequency (or wavelength), of the oscillating systems are adjusted. The latter one is an effect that can directly be measured. For the others, it is necessary to define which type of oscillator can describe the present system, and what kind of interaction has to be considered. In the following, the interaction of one oscillating system with an external driving term acting as a "control parameter" will be studied.

The standard example of a linear oscillator in mechanics is the harmonic oscillator. The differential equation of the driven harmonic oscillator with damping term γ and eigenfrequency ω_0 reads:

$$\ddot{x} + \gamma\dot{x} + \omega_0^2 x = B\cos(\omega_\mathrm{i} t) \ . \tag{3.1}$$

The dynamics of this oscillator caused by the external modulation with amplitude B and frequency ω_i is described in terms of resonance. This means that, after a transient behavior, the motion of the harmonic oscillator is only defined by the properties of the external driving force, i.e., frequency and amplitude. Without the external forcing term no oscillation would appear, and further, if the driving force would be "switched off", the oscillator would be damped until it comes to rest. It is evident that such an oscillator does not provide the ability to interact with

*The literature of nonlinear dynamics commonly uses a couple of different terms for synchronization like entrainment, mode-lock, phase locking, and frequency locking. In this work, these terms will be used synonymously.

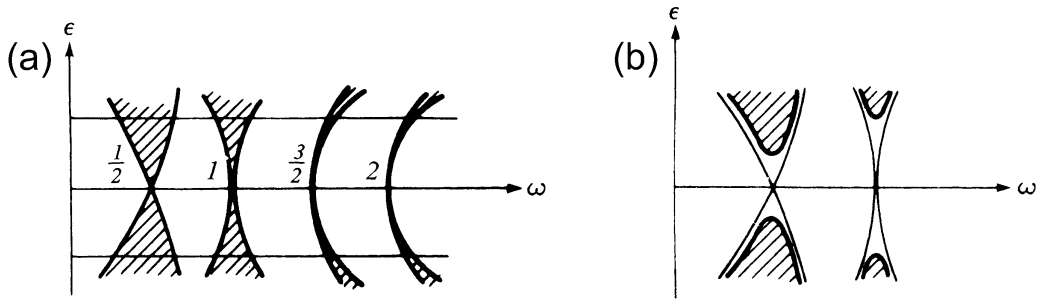

Figure 3.1: Schematic representation of the stability chart of a parametric oscillator: (a) without friction and (b) with friction. The parameter ω is the frequency and ϵ a measure for the modulation degree. The shaded region denotes unstable solution where the amplitude of the oscillator is growing, whereas the other regions provide stable solutions. When friction is included, a threshold of the modulation amplitude is needed to excite unstable solutions. (Adapted from [133])

the external driving force. Therefore, the properties of an oscillating system that possesses the feature to support synchronization has to be of a different type.

For studying the dynamical interaction between oscillating systems so-called self-oscillations have to be considered. These dynamical systems are described by some basic properties. The self-oscillation does neither stop its motion, although damping is present, nor grow unboundedly. Therefore, this oscillator has to be self-excited (aka self-sustained) due to a constant force, which can vary in time but is not periodic in time. The shape, amplitude and time scale of the oscillations are defined by the properties of the oscillating system itself. Hence, a self-excited system comprises dissipation, a power source, and a nonlinear coupling between the power source and the dissipation. For a linear coupling, the amplitude of the oscillator would be either continuously amplified, i.e., energy sustain exceeds damping, or equal to zero (no oscillation), i.e., damping exceeds energy sustain.

In the following, examples of dynamical systems are briefly introduced: The parametric oscillator, which is commonly described by the Mathieu equation [87, 133], the circle map and a relaxation oscillator of van der Pol type [134].

Parametric Resonance: In this case, the oscillation is forced by an internal parameter that is periodically modulated[†]. A standard example is a swing that has a periodically modulated effective length by a variation of the center of mass by the person sitting on it. A parametric excitation including friction can be described by Mathieu's equation [133] as follows:

$$\ddot{x} + \gamma\dot{x} + \omega^2[1 + \epsilon\cos(t)]x = 0 \ . \tag{3.2}$$

ϵ and ω are real numbers that describe the periodic change of the length and the frequency of the system. In dependence on the parameters (ω, ϵ) stable and unstable

[†]Note that the periodic modulation is not necessarily equal to an external periodical forcing of the system, but rather a property of the system itself.

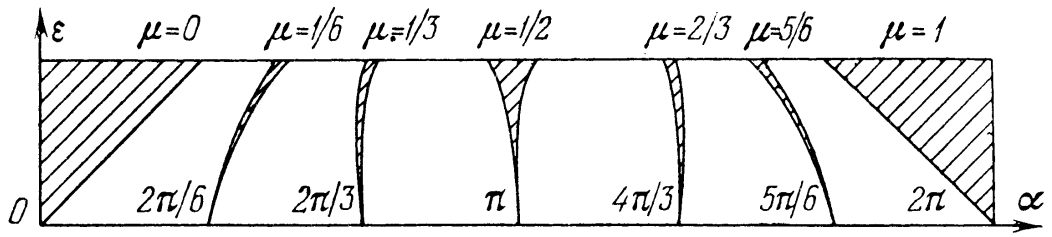

Figure 3.2: Diagram of the $\epsilon-\alpha$ plane of the circle map where ϵ denotes the strength and α the frequency of the driving force. The shaded regions depict the range where the oscillator is synchronized, and these regions are referred to as Arnol'd tongues. For driving amplitudes $\epsilon > 1$ a complex behavior with a transition to chaotic oscillations is found. (Adapted from [135])

solutions are possible. The stability chart of the oscillator is schematically shown in form of a $\omega - \epsilon$ plane in Fig. 3.1 (a) without an influence of friction ($\gamma = 0$), and Fig. 3.1 (b) depicts the influence of friction ($\gamma > 0$) on the stability of the parametric oscillator. The shaded regions mark the parameters where the oscillator is unstable, and the other regions refer to stable solutions. For unstable solutions, the amplitude of the oscillator is growing without limits. Nevertheless, in real systems only finite amplitudes can be attained because nonlinear effects become effective. It is found that the parametric oscillator is amplified when the frequency ν fulfills $\omega/\nu = k/2$ ($k = 1, 2, \ldots$)[‡]. A feature of parametric resonance is that the amplification is strongest when the exciting frequency is twice the characteristic frequency ($\nu = 2\omega$). When a friction term is included, it is found that the unstable regions are vertically shifted, and a threshold value of ϵ has to be overcome to amplify the oscillator. Without friction, an arbitrarily small disturbance is sufficient to force an oscillation.

The Circle Map: For studying the basic properties of synchronization the circle map is a suitable model. This map describes the phase evolution and interaction of two oscillators with nonlinear coupling in terms of a one-dimensional mapping on the unit circle:

$$\Phi_{n+1} = \Phi_n + \alpha + \epsilon \sin(\Phi_n) \ . \tag{3.3}$$

The angle Φ_n is defined on the interval $[0\ 2\pi]$. The interaction of the oscillator is described by the ratio of the frequencies of both oscillators $\alpha = f_\mathrm{i}/f_0$, where f_i is the frequency of the external driver and f_0 the frequency of the modulated oscillator. The parameter ϵ is proportional to the amplitude of the external modulation and is a measure of the nonlinear coupling between the oscillators. The dynamical behavior of the circle map is determined by these parameters, and a diagram of the parameter plane $\epsilon-\alpha$ is schematically shown in Fig. 3.2. At this point, it is suitable to introduce the concept of the rotational (winding) number μ, which is the time-averaged angular

[‡]In Eq. (3.2) the frequency ν is normalized to 1

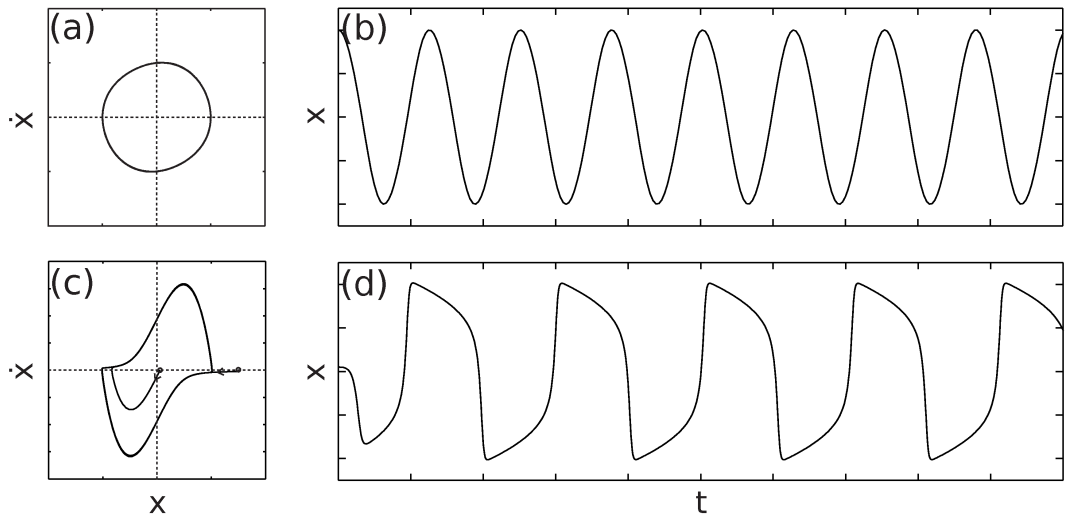

Figure 3.3: Phase space $(x, \dot{x})$ diagram and time-dependent behavior of the amplitude of the van der Pol oscillator for $\beta = 1$ and (a,b) $\epsilon = 0.1$ and (c,d) $\epsilon = 4$. The limit cycle is attained for initial amplitudes lying inside (outside) of the limit cycle, because of amplification (damping) of the system, as indicated in (c). For small values of ϵ, the limit circle is well described by a circle and a sinusoidal oscillation is found. For larger values of ϵ, the influence of the nonlinearity becomes apparent and anharmonicity is observed for the limit cycle and the oscillation.

rate of rotation of the oscillator [86]:

$$\mu = \lim_{i \to \infty} \frac{\Phi_i - \Phi_0}{2\pi i} \ . \tag{3.4}$$

When the rotational number is rational, it is found that the oscillator is locked to the driver frequency. In the diagram, these regions are shaded and they are referred to as Arnol'd tongues. In case of the linear circle map, i.e., $\epsilon = 0$, the rotational number simplifies for the locking condition to $\mu = f_\mathrm{i}/f_0 = p/q$ $(p, q \in \mathbb{N})$, where p and q denote the ratio of the frequencies. Hence, it is found that it is possible to synchronize an oscillator not only at its fundamental frequency, i.e., $\mu = 1/1$, but also for rational multiples of its fundamental. For parameters lying outside of these Arnol'd tongues, the rotation number is irrational and quasiperiodic states are found. The described behavior is found for amplitudes of $\epsilon < 1$. For $\epsilon = 1$ the Arnol'd tongues cover the interval $[0\ 2\pi]$ densely; and, for higher amplitudes, the Arnol'd tongues can overlap each other, and a transition to a chaotic behavior is observed.

van der Pol Oscillator: This relaxation oscillator is a so-called integrate-and-fire oscillator, meaning that a constant force is acting upon the oscillator until a threshold is reached, and the oscillator relaxes [83, 86, 87, 136]. For example, a vessel is constantly and slowly filled with water (integration) as soon as the threshold is reached, the vessel tips over and is quickly depleted (firing), and a new cycle begins.

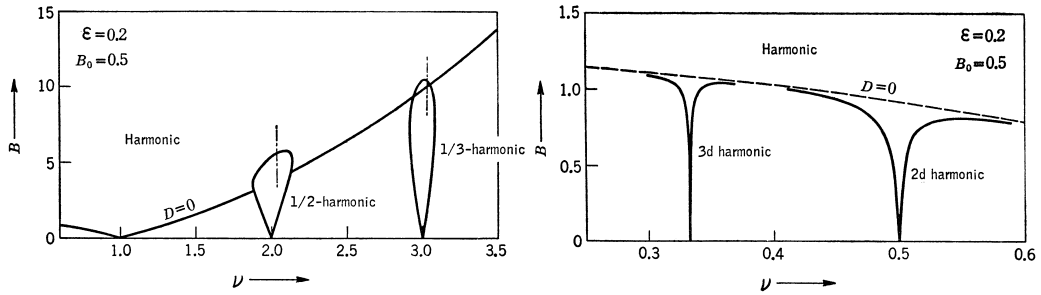

Figure 3.4: Diagram for the synchronization regimes of the van der Pol oscillator. The driver amplitude B is plotted vs. the normalized driver frequency $\nu = \omega_0/\omega_\mathrm{i}$. On the left hand side the Arnol'd tongues for harmonic and subharmonic synchronization and on the right hand side the higher-harmonic synchronization is shown. (From [87])

The forced van der Pol equation reads:

$$\ddot{x} - \epsilon(1 - \beta x^2)\omega_0 \dot{x} + \omega_0^2 x = B\cos(\omega_\mathrm{i} t) \ . \tag{3.5}$$

The special feature of the van der Pol oscillator is its dependence of the amplitude x on the damping. The parameter ϵ and β in the damping term denote the degree of nonlinearity and the energy feeding of the system, respectively. For small amplitudes ($\beta x^2 < 1$) the system is amplified, whereas for large amplitudes ($\beta x^2 > 1$) the system is damped. Because of the interplay of friction and energy sustain, the undriven van der Pol oscillator ($B = 0$) attains a limit cycle in the phase space $(x, \dot{x})$. For small values of ϵ, the oscillator has a nearly harmonic behavior, and the limit cycle is represented by a circle, see Fig.3.3 (a,b). For higher values of ϵ, the limit cycle becomes anharmonic, and the van der Pol oscillator behaves as a relaxation oscillator with two markedly different time scales, see Fig. 3.3 (c,d).

The solution of equation (3.5) reveals a manifold behavior depending on the amplitude B and the frequency ω_i of the external modulation. In so doing, it can be distinguished between three ranges of synchronization:

- $\omega_\mathrm{i} < \omega_0$: subharmonic synchronization,
- $\omega_\mathrm{i} \approx \omega_0$: harmonic synchronization,
- $\omega_\mathrm{i} > \omega_0$: superharmonic (higher-harmonic) synchronization.

In analogy to the circle map, the regions where the oscillator can be synchronized are shown in Fig. 3.4. Here, the amplitude B of the external modulation is plotted vs. the normalized frequency $\nu = \omega_0/\omega_\mathrm{i}$ of the driver. On the left hand side, the diagram for subharmonic synchronization and, on the right hand side, for superharmonic synchronization are schematically shown. The harmonic synchronization region is indicated in both diagrams. In agreement with the synchronization ranges of the circle map, these regions are also termed Arnol'd tongues. The Arnol'd tongue of the harmonic spans a broad region and overlaps with the subharmonic as well as

the superharmonic synchronization regions. The width of the Arnol'd tongues decreases for an increasing multiple (fraction) of the eigenfrequency for superharmonic (subharmonic) synchronization. For that reason, these Arnol'd tongues are difficult to detect, and the driving frequency has to be nearly commensurate to the multiple (fraction) of the eigenfrequency.

For the regions outside the Arnol'd tongues, quasiperiodic behavior with two independent frequencies is observed. Close to the edge of an Arnol'd tongue, incomplete synchronization, i.e., periodic pulling [137], of the oscillator is found, in which the phase angle as well as the amplitude of the oscillator varies periodically. Similar to the circle map, the van der Pol oscillator also provides the ability to chaotic behavior.

To summarize, in this Chapter basic aspects of oscillating systems with emphasis on the properties of the self-excited oscillator and the interaction of an oscillator with an external force was described by means of the circle map and the van der Pol oscillator. The self-excited oscillator requires friction, an energy source and a nonlinear coupling between these quantities. For a periodical forcing of this type of oscillator, harmonic as well as sub- and superharmonic synchronization can be found. This means that it is possible to drive the oscillator with frequencies not only close to its eigenfrequency but also with multiples or fractions of the eigenfrequency.

It is worth mentioning that the described behavior of the van der Pol oscillator was successfully adopted to describe the dynamical behavior of waves with and with no external forcing, e.g., Refs. [138–141]. Furthermore, it was shown that an excitation of dust-particle oscillations in the sheath of an rf plasma can be understand in terms of a parametric excitation [142, 143].

The concept of synchronization of an oscillator caused by an external force is captured in Chap. 4, where the response of small dust cloud and of self-excited dust-density waves to an external modulation will be studied.

4 Dynamical Response of Dust Clouds to an External Modulation

A periodic external stimulus of a dust particle or of the entire dust cloud is a useful tool to gain more information about the dynamical response of the system. The modulation or excitation can be achieved electrically via a biased wire [33–35] or by a low frequency modulation of the voltage superimposed to the dc bias of an electrode [144–146], by laser manipulation [36, 49, 147] or by a neutral drag [51, 148]. By applying such an external modulation, it was possible to determine the charge of dust particles [12, 144, 149, 149] or the interaction force between dust particles [49, 147]. Furthermore, it was possible to excite Mach cones [27–31] and dust lattice waves [33–40], or to study the dispersion of dust-density waves [73, 77–81, 145, 146, 150].

The charge of dust particles levitated in the sheath of an rf plasma was determined by measuring the resonance curve of the oscillation amplitude depending on the applied low frequency modulation [12, 149]. The resonance frequency, which is characterized by an effective parabolic potential well, is proportional to the particle charge.

Laser manipulation was used to study one-dimensional [33, 151] as well as two-dimensional dust lattice waves [36, 39, 40, 152, 153], Mach cones [29, 154, 155] and the intershell rotation of two-dimensional dust clusters [48].

By applying a neutral-gas drag, shock waves could be excited [148] and a rotation of a two-dimensional dust cluster was studied due to a gas drag induced by a rotating disk [51].

The dispersion of dust-density waves could be measured either by synchronizing the self-excited wave [73, 78–81, 145, 146] or by changing the discharge parameters (gas pressure, discharge voltage) [77, 150] and therewith the plasma parameters (density, plasma potential, electron temperature). For the latter technique only a single point of the dispersion relation is determined for a set of plasma parameters, and, for a representation in one diagram, these single measurements have to be normalized. Therefore, the plasma parameters have to be measured for each data point. By using the technique of synchronization, the plasma parameters are equal for all data points, but a small disturbance due to the modulation has to be assumed.

In this Chapter, the influence of an external modulation on small dust clouds is studied in Sec. 4.1. The synchronization of dust-density waves is investigated in Sec. 4.2 regarding the properties of self-excited waves and the range of frequencies, where dust-density waves can be synchronized. The results are discussed in Sec. 4.3.

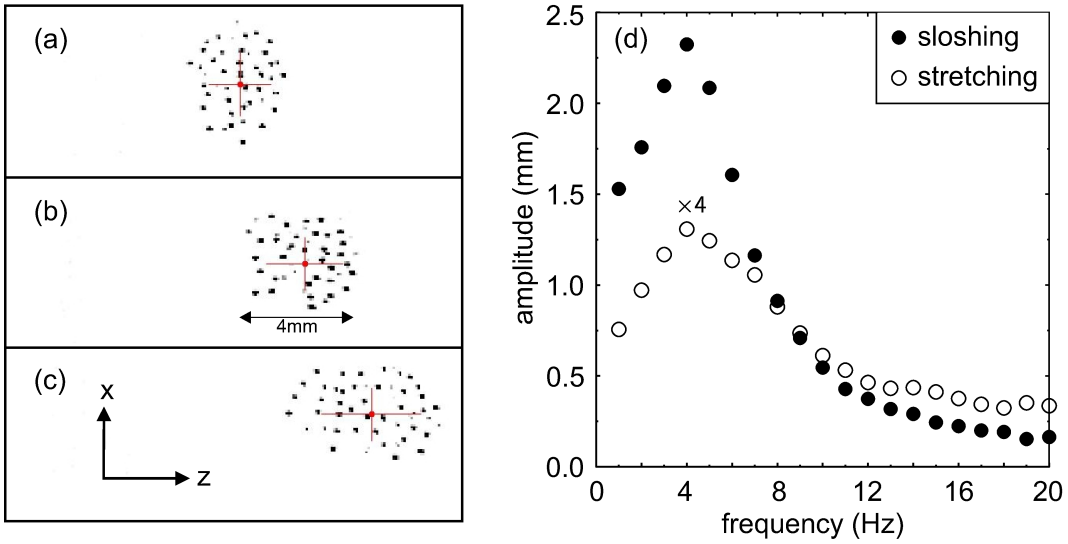

Figure 4.1: Response of a small dust cloud to the external modulation ($f_{\mathrm{mod}} = 4$ Hz): (a) left turning point, (b) equilibrium position and (c) right turning point. The position of the center of mass (red dot) and the second moments (red lines) are indicated. A pronounced shift of the entire dust cloud (sloshing) that is accompanied by a compression and stretching of the cloud length (stretching) is observed. (d) The amplitude of the sloshing and the stretching motion in axial direction are plotted vs. the frequency of the modulation. A resonance-like behavior for both the sloshing and the stretching motion is found. (Adapted from Appendix B.1)

4.1 Sloshing Motion of Small Dust Clouds

In small dust clouds, no self-excited dust-density waves were observed. The particles were found in a gaseous state where they performed a fast irregular motion. The dust cloud was externally modulated with a sinusoidal signal superimposed on the dc voltage of the anode. The external modulation of a small dust cloud is interesting because its behavior to the modulation is determined by the confining potential, and thus, a measure of the qualitative properties of the potential well.

The response of these clouds to an external modulation was studied over a frequency range of (1−65) Hz. It was found that the modulation does not lead to an excitation of dust-density waves in these clouds. Instead, at low frequencies [$f_{\mathrm{mod}} = (1{-}15)$ Hz], a sloshing motion, i.e., a periodic motion of the entire dust cloud, and a stretching motion, i.e., a periodic variation of the cloud boundary, was observed. Snapshots of this motion are shown in Fig. 4.1 (a)-(c), where the anode is located on the left hand side of the image. It can be seen that the position as well as the shape of the dust cloud is affected by the external modulation. The cloud boundary is stretched when the dust cloud moves away from the anode (right turning point), and it is compressed when the cloud moves in direction to the anode (left turning point). The equilibrium position shows a nearly circular cross-section of the dust cloud.

For studying the sloshing and stretching motion in more detail, the center-of-

mass position and the second moment, which is a measure for the deformation of the cloud, were calculated (see Eqs. (2) and (3) in Appendix B.1).

The obtained results for the sloshing (full circles) and the stretching amplitude (open circles), depending on the frequency of the external modulation, are shown in Fig. 4.1 (d). In this diagram, the motions in z-direction, i.e., in axial direction, are represented. The motion in x-direction has a similar behavior but at lower amplitudes. For both motions in z-direction, a resonance-like behavior is found. First, the amplitudes increase with higher modulation frequency until a maximum at about 4 Hz is reached. Then, a steep drop of the sloshing amplitude with increasing frequencies is found, whereas the decrease of the stretching amplitude is more gradual. At modulation frequencies of about 15 Hz, nearly constant values for the amplitudes are reached. These amplitudes are consistent with the amplitudes determined for the motion of the dust cloud without external modulation, i.e., the thermal motion of the dust cloud. For higher modulation frequencies, no excitation of dust-density waves was observed but the dust cloud remained in a state comparable to the thermal motion of the undisturbed dust cloud.

The influence of the sloshing motion on self-excited dust-density waves in a large dust cloud is studied in Sec. 4.2.3.

4.2 Dust-Density Waves

Dust-density waves emerge spontaneously in dust clouds due to streaming ions [66]. These waves are compressional waves at low frequencies of tens of Hertz. In this thesis, a main objective is the analysis of the interaction between an external modulation and the self-excited a dust-density wave.

A short overview on the research of dust-density waves is given in Sec. 4.2.1; the properties of a self-excited dust-density wave are described in Sec. 4.2.2, and the results of the external modulation of dust-density waves are given in Sec. 4.2.3.

4.2.1 Status of Research

The existence of a dust-acoustic wave was predicted by Rao *et al.* [60] in terms of a fluid description. The specific property of the dust-acoustic wave is a linear dispersion, i.e., phase and group velocity of the wave coincide, at low wavenumbers. In this thesis, the wave is termed dust-density wave which is a more general term and allows a dispersion for low wavenumbers, i.e., phase and group velocity of the wave are not the same. The first observation of a dust-acoustic wave was described by Chu *et al.* [61] in the edge of an rf discharge, and later interpreted by D'Angelo as a dust acoustic wave [62]. In anodic plasmas, a dust-acoustic wave in front of a positively biased anode was found by Barkan *et al.* [63]. The first measurement of the dispersion relation was made by Thompson *et al.* [78] with the technique of synchronizing the dust-acoustic wave by an external driving force.

On the experimental side, the measurement of the dispersion relation is an important task. Thus, this information can be well compared with theoretical predictions.

There are two attempts to measure the dispersion of a dust-density wave. The first method is to measure the wavenumber and the frequency of the wave at different discharge parameters [77, 156]. This approach has the benefit that the self-excited dust-density wave is studied; on the other hand, it has the disadvantage that for each measurement the plasma parameters have to be measured, because this information is needed for a comparison with theory. The second approach is to apply an external modulation, and to synchronize the dust-density wave at the driving frequency. In this way, the dispersion relation can be measured simply by changing the driving frequency [78–81,145,146]. The benefit of this method is that only one measurement of the plasma parameters is needed to compare the experimental results with the theoretical predictions. The limitation of this technique is that it is necessary to verify that the wave frequency is locked to the driving frequency, and it has to be assumed that the disturbance of the plasma is small.

On the theoretical side, several approaches exist for the description of a dust-density wave including fluid theories [60, 68–71] or kinetic theories [66, 72, 73]. The theories have taken different aspects into account, like a charge variation of dust particles [69,74–77], boundary effects due to the finite size of a dust cloud [68,70,71], and recently the effect of a finite temperature of the dust particles [73].

Not only the experimental measurements of the dispersion relation of dust-density waves are of interest for comparison with the theoretical approaches, but also the dynamics of dust particles within the propagating wave fronts have gained attention [157–159]. By using the particle image velocimetry technique the growth rate of the wave [65, 160, 161] and the dust temperature [81, 162] was measured.

4.2.2 Self-Excited Dust-Density Waves

Before the influence of an external modulation is described, the properties of the self-excited wave are investigated. Here, the self-excited dust-density waves in large dust clouds and the methods for studying the wave dynamics are briefly described.

For obtaining an overview on the propagation of a dust-density wave, the space-time diagram [Fig. 4.2 (c)] is a suitable presentation. For composing such a diagram, a region of interest (ROI) is chosen, see Fig. 4.2 (a), and averaged along the x-direction for each image of a movie. The obtained one-dimensional intensity profile $I_\mathrm{m}(z,t)$ (black solid line) and the time-averaged intensity profile $\langle I_\mathrm{m}(z)\rangle$ (red dotted line) are shown in Fig. 4.2 (b). The time-averaged intensity profile, which is proportional to the averaged density profile, has a parabolic shape. For the one-dimensional profile, it is found that the wave amplitude is increasing from the left to the right. Hence, the wave emerges at the anode facing side of the cloud. The highest modulation is observed in the core region of the dust cloud. At the far side from the anode, particle granulation becomes evident and the density of the modulation of the wave is reduced.

For the analysis of the dust-density wave only the variation of the dust-density, i.e., the dust-density fluctuation $\widetilde{n}_\mathrm{d}(z,t)$, is of interest. The dust density fluctuation is calculated by subtracting the time-averaged intensity from the intensity profile for each time step t, $\widetilde{n}_\mathrm{d}(z,t) = I_\mathrm{m}(z,t) - \langle I_\mathrm{m}(z)\rangle$. This quantity is composed in

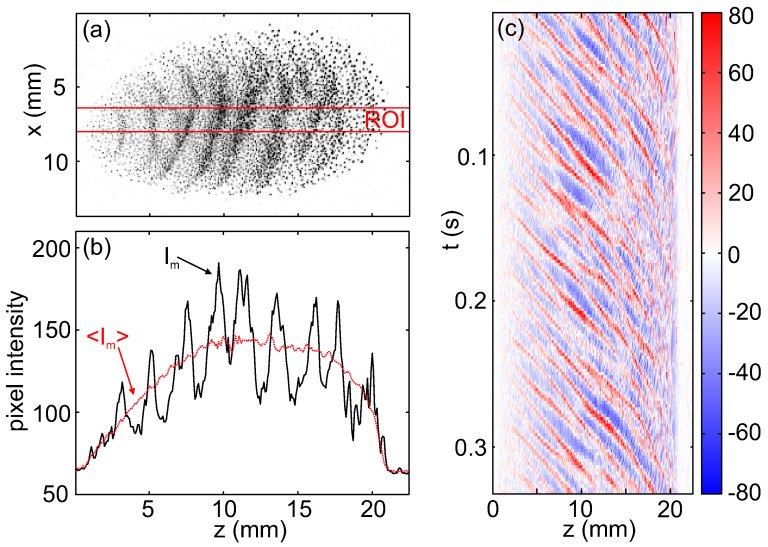

Figure 4.2: (a) A snapshot of a self-excited dust-density wave in a large dust cloud. The region of interest (ROI), chosen for the analysis of the temporal evolution of the dust-density wave, is indicated. (b) The one-dimensional intensity profile I_m (black solid line), obtained by averaging the vertical width of the ROI, and the time-averaged profile $\langle I_\mathrm{m} \rangle$ (red dotted line) are displayed. (c) The space-time diagram, which is composed of the one-dimensional intensity profiles and corrected for the time-averaged profile, $I_\mathrm{m}(t) - \langle I_\mathrm{m} \rangle$. (From Appendix B.3)

the space-time diagram where the time t is plotted vs. the propagation direction z of the dust-density wave. Hence, the color-coded intensity is a measure of the dust-density fluctuation.

The result is shown in Fig. 4.2 (c). Here, the red stripes indicate regions of enhanced dust density and, therefore, are identified as wave crests. The blue stripes are the wave troughs. A regular wave propagation, i.e., constant frequency and wavelength, would be found in the space-time diagram as a set of parallels with constant phase speed $v_\varphi = dz/dt$. Instead, the wave pattern observed for the self-excited dust-density wave shows narrow wave crests of varying slopes. This indicates an incoherent wave pattern with changing propagation speed that leads to changing wavelength and wave frequency. Furthermore, merging of wave fronts is observed, where two or more wave fronts are found to intersect and propagate as a single wave front afterwards. This is a second mechanism that affects the wavelength and frequency.

In this situation, appropriate methods for measuring the local and instantaneous phase speed need to be applied. One suitable method is based on the shift of the wave front in subsequent movie frames, which can be quantitatively extracted by cross correlation analysis. The averaged phase speed is then determined to $v_{\varphi,\mathrm{m}} = (75 \pm 5)$ mm s^{-1}.

Based on the description of the temporal and spatial evolution of the self-excited dust-density wave, it turns out that the frequency of the wave and the spatial distribution of the frequency are of particular interest. The frequency of the self-excited

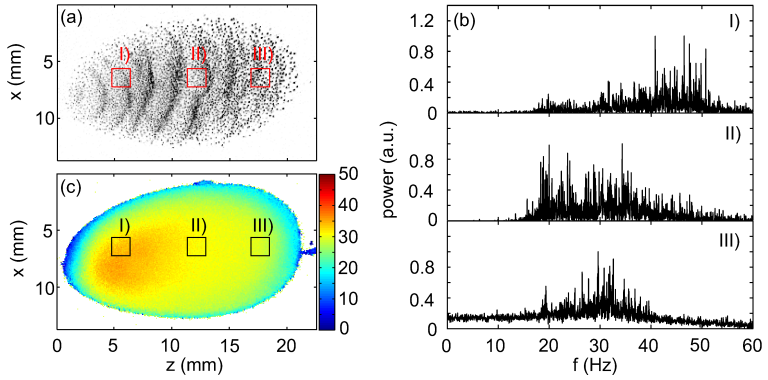

Figure 4.3: (a) Snapshot of a dust-density wave in a large dust cloud. (b) Spectra at different position of the dust cloud, as indicated in the two-dimensional images, (a) and (c), and referred to as with Roman numerals. The spectra were obtained by averaging over a rectangular region, which is indicated as well. (c) The two-dimensional frequency map showing the distribution of the mean frequency. A gradual shift of the mean frequency from higher values at the anode-facing side to lower ones at the far side is found. (Adapted from Appendix B.3)

dust-density wave was calculated with a fast fourier transformation (FFT) algorithm for each pixel position within the frame. The spectrum of a single pixel contains a large number of spectral components, and is therefore inherently noisy. It is assumed that this is due to the incoherent wave pattern as well as an influence of particle granulation.

Therefore, in Fig. 4.3 (b) spectra averaged over rectangular regions of interest are shown for different locations within the dust cloud. The spectra are labelled by Roman numerals and the position is indicated in the two-dimensional frames. It is found that all three spectra show a broad frequency distribution over a range of (20−50) Hz depending on the position. The frequency distribution in spectrum no. I), which is recorded at the front region of the cloud, is shifted to higher frequencies compared to the other two spectra no. II) and III), which represent the middle and the far region of the dust cloud, respectively.

For the calculation of a spatial frequency distribution, the mean frequency $\bar{f}$ of the spectra at each pixel position (x, z) was calculated by the weighted spectral intensity:

$$\bar{f} = \frac{\int P(f')f'\mathrm{d}f'}{\int P(f')\mathrm{d}f'} \ , \tag{4.1}$$

with $P(f)$ being the spectral power density. The mean frequency is color-coded in a two-dimensional diagram, where the color assigns the value of the frequency at that position. This diagram is termed “frequency map”, and the result for the self-excited dust-density wave is shown in Fig. 4.3 (c). Here, it is found that the frequency distribution is not homogeneous, which would have been already expected regarding the time evolution of the wave crests in the space-time diagram. But it is also found that, at the anode-facing side (left-hand side), the frequency is higher compared to the anode-far side (right-hand side). The transition is found to be

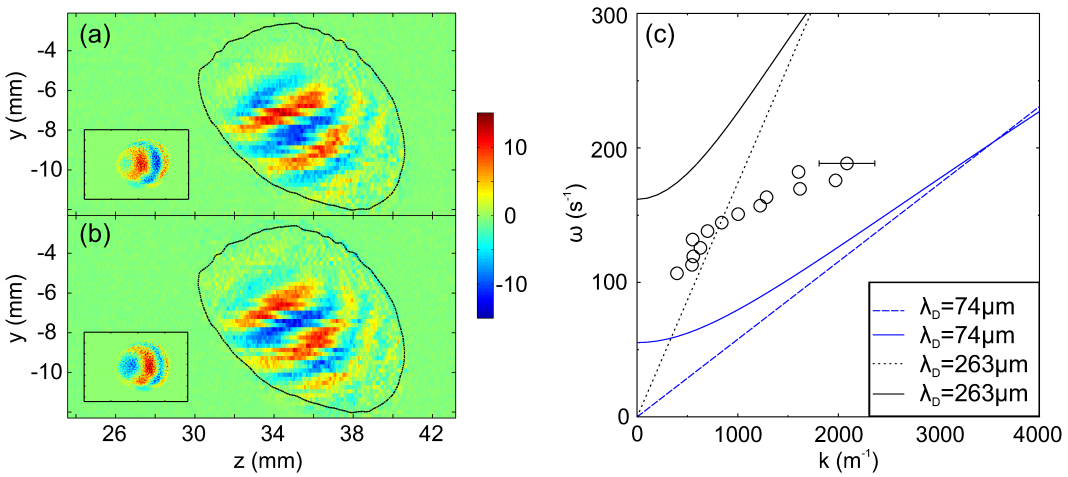

Figure 4.4: Three-dimensional reconstruction of the complex wave function $C(x,z) + iS(x,z)$ of the wave fronts measured in horizontal sections. Displayed are (a) the real part $C(y,z)$ and (b) the imaginary part $S(y,z)$. The insets depict the horizontal reconstruction at $y = -7$ mm for the real part and the imaginary part, respectively. The wave propagates at an angle with respect to the horizontal with a slightly higher wavelength than the one measured in the horizontal section. (c) The measured dispersion of the dust-density wave plotted together with theoretical curves of the dust acoustic wave (dashed and dotted lines) and the cylindrical wave guide mode (solid lines) for two limiting cases of the Debye length λ_D. (Adapted from Appendix B.1)

gradual. This result is in agreement with the observation of the merging of wave fronts in the space-time diagram.

4.2.3 Synchronization of Dust-Density Waves

In this Section, the influence of an external modulation on the self-excited dust-density wave is studied. Regarding to the observed frequency range of a self-excited dust-density wave of (20−50) Hz, the frequency modulation is divided into three domains: First, the range of low frequency modulation ($f \leq 15$ Hz), where sloshing and stretching of a small dust cloud could be excited; the intermediate domain [$f = (16-45)$ Hz], which is close to the frequency range of the self-excited wave and synchronization of a dust-density wave is found; and a high frequency region, where the frequency of the applied modulation is even larger than the frequencies found for the self-excited wave.

The medium-sized clouds are investigated regarding the propagation direction of the wave fronts and the dispersion of a dust-density wave with respect to finite size effects. The investigation of dust-density waves in a large dust cloud is focused on the influence of a sloshing motion and the synchronization of the wave.

Medium-Sized Dust Clouds ($d \gtrsim \lambda$)

The self-excited dust-density wave in the investigated medium-sized dust cloud could be synchronized via the external modulation in a frequency range of $f \approx (18-40)$ Hz. Besides the possibility to measure the dispersion properties by applying an external modulation, the external synchronization is also suitable to determine the three-dimensional structure of a dust-density wave (see Appendix B.1).

For the reconstruction of the three-dimensional wave fronts, it is assumed that the wave can be described by a complex spatial wave function $C(x,z) + iS(x,z)$ with

$$C(x,z) = \sum_{l=1}^{N} B_l(x,z) \cdot \cos(2\pi f_{\mathrm{mod}} t_l) \tag{4.2}$$

$$S(x,z) = \sum_{l=1}^{N} B_l(x,z) \cdot \sin(2\pi f_{\mathrm{mod}} t_l) \ . \tag{4.3}$$

Here, $B_l(x,z)$ is the frame at time step t_l and the modulation frequency f_{mod} is specified by the external modulation signal, but is also verified in the spectra determined with a FFT algorithm. The resulting complex wave function represents a time-averaged snapshot of the dust-density wave.

In Fig. 4.4, the wave fronts in a $y-z$ cross-section for (a) the real and (b) the imaginary part are shown. The cross-section is reconstructed from a set of $x-z$ observations at different height y. The insets depict a horizontal $x-z$ reconstruction of the real and the imaginary part at a vertical position of $y = -7$ mm. The position of the medium-sized dust clouds is specified with respect to the anode center. It is found that the wave fronts of the dust-density wave are propagating in axial as well as in vertical direction at an inclination angle of about $\alpha = 45°$ with respect to the axial direction. The observed propagation direction of the dust-density wave is in accordance with the electric field direction and, therewith, the direction of the streaming ions, as can be seen in Fig. 4.5 for a large dust cloud.

Due to the inclination angle α, the measured wavelength λ^* within the horizontal sections has to be corrected by that inclination, $\lambda = \lambda^* \cos\alpha$, for a determination of the dispersion relation. The resulting dispersion relation is shown in Fig. 4.4 (c), where the applied frequency ($\omega_{\mathrm{mod}} = 2\pi f_{\mathrm{mod}}$) is plotted vs. the wavenumber ($k = 2\pi/\lambda$). A typical error of measurement is indicated. Additionally, the theoretically obtained dispersion relations for the dust acoustic wave [60],

$$\omega = \omega_{\mathrm{pd}} \lambda_{\mathrm{s}} k \ , \tag{4.4}$$

and the cylindrical-waveguide mode [68],

$$\omega = \omega_{\mathrm{pd}} \left(\frac{k^2 + \gamma^2}{k_{\mathrm{s}}^2 + k^2 + \gamma^2} \right)^{1/2} \ , \tag{4.5}$$

are plotted. Here, ω_{pd} is the dust plasma frequency, λ_{s} the shielding length, $k_{\mathrm{s}} = 1/\lambda_{\mathrm{s}}$, $\gamma = 2.4/R$, and R is the radius of the cylinder of the waveguide. The

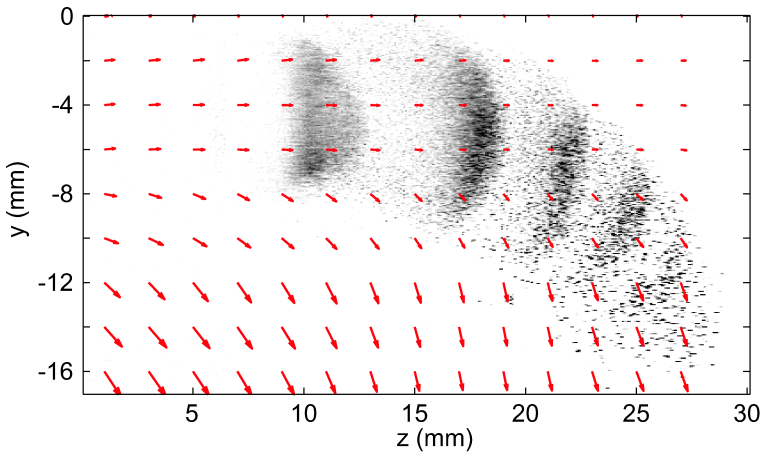

Figure 4.5: A vertical reconstruction of the wave fronts in a large dust cloud. The self-excited dust-density wave was externally synchronized at a frequency of 20 Hz. The electric field (red arrows), calculated from a two-dimensional plasma potential measurement at comparable discharge parameters, is overlaid onto the vertical image of the dust-density wave. The propagation direction of the wave fronts is in good agreement with the electric field direction.

fundamental mode of the waveguide is given by k_s and γ, and in the limiting case, $k = 0$, a cutoff-frequency ω_{min} is found,

$$\omega_{min} = \frac{\omega_{pd}\gamma}{\sqrt{k_s^2 + \gamma^2}} \; . \tag{4.6}$$

Both dispersion curves, i.e., the dust acoustic wave and the waveguide mode, are shown for the limiting case of the ion Debye length λ_{Di} and of the order of the electron Debye length λ_{De}. The first case describes the situation for thermal ions, $T_i = 0.1$ eV, $T_i \ll T_e$; and the shielding length is given by the linearized Debye length as $\lambda_D \approx \lambda_{Di} = 74$ μm. The latter case characterizes the situation for ions streaming with Bohm velocity, $v_B = \omega_{pi}\lambda_{De}$, where the ion Debye length is of the order of the electron Debye length leading to a shielding length in terms of the linearized Debye length of $\lambda_D \approx 2^{-1/2}\lambda_{De} = 263$ μm. The measured data points lie in between these two cases. It is found that the waveguide-mode describes the group velocity of the experimental data better than the dust acoustic wave dispersion. Therefore, it can be concluded that the dispersion of the dust-density wave in a medium-sized dust cloud is affected by its finite size and a cutoff frequency for the long wavelength limit, i.e., $k = 0$, is expected.

Large Dust Clouds ($d \gg \lambda$)

Compared to medium-sized dust clouds, the wave activity in large dust clouds is more pronounced, and emerges in a larger fluctuation amplitude of the wave crests and troughs. Furthermore, longer wavelengths can fit into the cloud because of the extended length of the cloud.

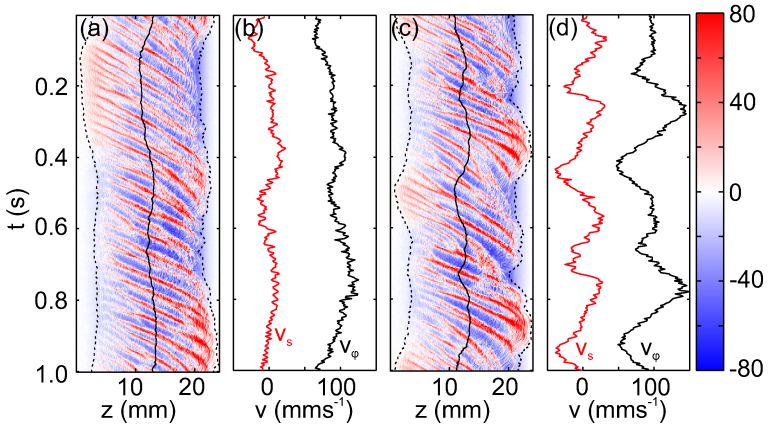

Figure 4.6: Low-frequency response to the external modulation of 1 Hz (a,b) and 2 Hz (c,d). (a) and (c) space-time diagrams in which the center-of-mass position (solid line) and the boundary of the dust cloud (dashed lines) are indicated. (b) and (d) calculated velocities of the center of mass motion v_s (red curve) and the phase velocity of the dust-density wave v_φ (black curve). The sloshing motion is manifested as the periodical motion of the center of mass and the cloud boundary. Furthermore, a periodical modulation of the phase velocity of the wave is observed. (From Appendix B.3)

For comparing the propagation direction of a dust-density wave in a large dust cloud with the direction of the ion flow, a vertical reconstruction is shown in Fig. 4.5 together with the electric field (red arrows) obtained from a two-dimensional plasma potential measurement at comparable discharge parameters. Here, the dust-density wave was synchronized by the external modulation ($f_\mathrm{mod} = 20$ Hz) for studying a coherent wave pattern. The three-dimensional recording was performed by using a scanning video microscopy technique introduced by Menzel *et al.* [163] for self-excited dust-density waves. The dust-density wave was recorded at a framerate of $\nu = 8 \times f_\mathrm{mod}$ in the horizontal section, and the combination of laser sheet and camera was vertically moved. Every eighth image was chosen and composed into a three-dimensional matrix representing a three-dimensional stroboscopic image of the wave.

It is found that the propagation direction is closely aligned with the electric field direction. Close to the anode axis ($y = 0$ mm), the wave fronts are found perpendicular to the z-direction, so that no inclination angle is present and a measured wavelength has not to be corrected. At larger distance, the wave fronts tilt and the wave propagates under an inclination angle. These observations are in agreement with the propagation direction of the dust-density wave found in the medium-sized dust cloud.

In the following, the response of the dust-density wave to the external modulation is studied with emphasis on the different modulation frequencies: low, intermediate and high. Special attention is focused on the question whether the dust-density wave is locked to the modulation frequency, and whether the sloshing motion interacts with the dust-density wave at a low-frequency modulation.

Sloshing Excitation at Low Frequencies: For small dust clouds, the low frequency excitation has led to a distinct sloshing and stretching motion of the entire dust cloud. The response of a large dust cloud is more complex because of the naturally excited dust-density waves, as shown in Fig. 4.6 for an external modulation frequency of (a,b) 1 Hz and (c,d) 2 Hz, respectively.

At low modulation frequencies the effect on the dust cloud is two-fold: On the one hand, the sloshing is verified by the periodical movement of the center of mass, and an oscillation of the cloud boundary is found. The variation of the cloud boundary at the anode-facing side agrees with the period of the modulation frequency, while at the far side, the boundary oscillates at twice the modulation frequency. On the other hand, the phase velocity v_φ of the dust-density wave is periodically modulated due to the sloshing motion, leading to an alternating slope of the wave crests in the space-time diagram. The phase velocity of the wave and the sloshing velocity v_s are found to vary in a range of $v_\varphi = (60{-}120)$ mm s^{-1} and $v_\mathrm{s} = (-25 \ldots 20)$ mm s^{-1}, respectively.

In a first approximation, it is suggested that the sloshing motion and the propagation of the self-excited dust-density wave are independent of each other, so that the observed wave pattern can be described by a superposition of the two effects. Then, the phase velocity of the resulting wave pattern can be estimated as:

$$v_\varphi = v_\mathrm{s} + v_{\varphi,\mathrm{m}} \ . \tag{4.7}$$

The phase velocity of the self-excited dust-density wave was previously determined as $v_{\varphi,\mathrm{m}} = 75$ mm s^{-1}. The addition of the phase velocity of the self-excited wave and the sloshing velocity results in a variation of the phase velocity of about $(50 - 95)$ mm s^{-1}. Comparing this with the obtained phase velocity, it is found that the measured phase velocities are slightly higher than expected from the superposition. It is supposed that this could be understood by an energy gain of the wave through an acceleration of the potential well, which might be similar to a swing-by maneuver (aka gravitational slingshot) of a spacecraft in the gravitational field of a planet. The curves of the sloshing velocity and the phase velocity are found to be in phase, i.e., the acceleration of wave fronts occurs when the dust cloud is shifted in direction of the propagation of the dust-density wave, and deceleration is found when the dust cloud is shifted in opposite direction. This second observation agrees well with the assumption of a superposition of both types of motions.

Synchronization of Dust-Density Waves: The response of the dust cloud to a modulation at higher frequencies is compiled in Fig. 4.7. Here, a combination of diagrams is given for modulation frequencies of 1, 5, 10, 20, 30, and 120 Hz. From top to bottom, a snapshot of a single frame, the space-time diagram, the two-dimensional frequency map, and examples of single spectra are shown, their locations are indicated in the snapshots and in the frequency maps, and, for reference, labelled with Roman numerals. Note that the spectra are normalized by the largest spectral component; hence, a comparison between the intensities of spectra is not possible. The spectra of the modulated dust-density wave show distinct frequency components in

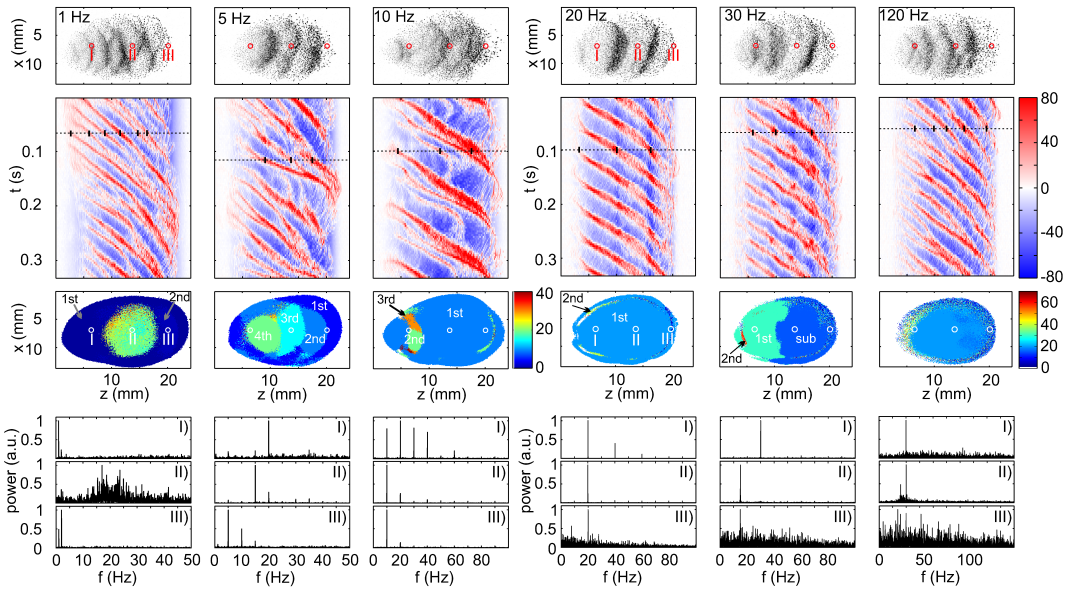

Figure 4.7: Overview of the response of the dust-density wave to an external modulation. From left to right: the results obtained for modulation frequencies of 1, 5, 10, 20, 30, and 120 Hz are shown. From top to bottom an individual snapshot, the space-time diagram, the frequency map and, for instance, single spectra at three positions in the dust cloud are displayed. The spectra are labelled with Roman numerals, and the position is indicated in the snapshot and in the frequency map. The marks sub, 1st, 2nd, 3rd, and 4th are referred to as the subharmonic, first (fundamental), second, third, and fourth harmonic of the applied frequency. (Adapted from Appendix B.3)

contrast to the spectra of the self-excited wave, which have a broad frequency distribution. Therefore, the frequency maps are color-coded by the component with the largest spectral intensity instead of the mean frequency. A more detailed overview on the dynamics is shown in Figs. 4 and 6 of Appendix B.3.

The column depicting the response at a modulation of 1 Hz reveals the previously described behavior. The frequency map represents the observation of a travelling dust-density wave in the core region of the dust cloud. There, a noisy distribution of frequencies is found, as can be seen in more detailed in spectrum II). It is found that the spectrum within the core region is similar to the spectrum obtained for the self-excited dust-density waves. At the outer region of the dust cloud, an oscillation due to the external modulation is observed, see spectra I) and III). The spectra contain not only the first harmonic, i.e., the fundamental of the modulation frequency, but also higher harmonics are present. At the far side, a region with a higher intensity of the second harmonic is found. This is in agreement with the observation within the space-time diagram that, at the far side, the cloud boundary oscillates at twice the modulation frequency.

For higher frequencies, it is found that, even at a low modulation frequency of 5 Hz, the wave is synchronized by the signal, but a complex wave pattern emerges. This is well reproduced in the space-time diagram, and a clear difference to the wave pattern of the self-excited dust-density wave is observed. The influence of the

external modulation is also visible in the frequency map and in the spectra. The frequency map shows a larger number of regions where the higher harmonics have a larger spectral intensity than the fundamental. But, at the outer regions of the dust cloud, the fundamental is still dominant. In the core region, a shift from the anode-facing side, where the fourth harmonic has the highest spectral intensity, towards the far side is found, where lower harmonics become more important.

An interesting observation in the space-time diagram is found for the modulation frequency at 10 Hz. Here, backward travelling wave crests, i.e., against the streaming direction of ions, are observed. For example, a wave crest at position $z \approx 14$ mm and time $t \approx 0.1$ s is propagating backward to the position $z \approx 13$ mm at time $t \approx 0.15$ s. It is found that a faint wave front of weaker intensity is slowed down and propagates towards the anode until the wave front merges with the following wave front.

For intermediate modulation frequencies ($f_{\mathrm{mod}} = 20$ Hz), close to the frequencies of the self-excited dust-density wave, the wave is found to be synchronized at the driving frequency (i.e., the fundamental) over the entire cloud, despite a nested shell structure at the boundary of the cloud in which the second harmonic dominates. This shell structure can be attributed to reflected wave fronts or particle reflection at the cloud boundary [164]. This synchronized state is valid for excitation frequencies in the range of (14−24) Hz. In the space-time diagram regularly propagating wave fronts are found, which means that the wave fronts are parallel to adjacent wave fronts. Further, it can be seen that the slope increases, i.e., the phase velocity of the wave is reduced, close to a z-position of 15 mm.

For a higher frequency of 30 Hz merging of wave crests is found. There, a slower propagating wave front is overtaken by a faster one, and these wave fronts merge to a single wave front, which then propagates with the phase velocity of the slower wave front. This merging of the wave fronts is accompanied by a halving of the frequency of the wave. Thus, the first subharmonic at $f_{\mathrm{mod}}/2$ becomes dominant, and a doubling of the wavelength is observed. The doubling of the wavelength can be seen in the space-time diagram, where the wave crests are marked, as well as directly in the snapshot. The frequency map shows two large regions, indicating a dominant frequency at the 1st harmonic (30 Hz), which is located at the anode-facing side, and a region indicating a dominant spectral component at the first subharmonic (15 Hz).

In case of the modulation at frequencies of 120 Hz, a response at a frequency of 20 Hz is found, which corresponds to the subharmonic at 1/6 of the excitation frequency. This hints at superharmonic synchronization. The modulated dust-density wave is found to be more regular than the self-excited one. For comparison, Thomas *et al.* [80] and Williams *et al.* [81] have observed that the high frequency modulation does not lead to a synchronization of the dust-density wave, and the wave was found to propagate at a frequency similar to the frequency of the self-excited wave. Furthermore, Thomas *et al.* [80] reported a high frequency modulation of the wave fronts superimposed to the self-excited wave. This effect might be attributed to the use of polydisperse dust particles [81].

4.3 Discussion

The external modulation by a variation of the anode voltage was studied for small, medium-sized and large dust clouds. Depending on the applied frequency, i.e., low, intermediate and high frequencies, the response of the dust cloud differs qualitatively.

A simplified picture how the external modulation couples to the dust cloud is as follows: The confinement potential of a dust cloud is defined by the force balance of the electric field force and the ion drag force. An external modulation of the anodic plasma only marginally affects the electric field, but the ion density varies periodically because of the modulation. In good approximation, the electric field force remains nearly constant whereas the ion drag force is periodically modulated because of the variation of the ion density. For a low-frequency modulation, it is reasonable that the effective potential well is adiabatically shifted due to the modulation of the ion drag force. This is justified because the ion plasma frequency ($\omega_{\mathrm{pi}} \sim$ MHz) is large compared to the applied modulation frequency ($\omega_{\mathrm{mod}} \sim$ Hz). This simplified picture can be understood in terms of a parametric excitation since an internal plasma parameter, i.e., the ion density, is periodically modulated.

The low-frequency modulation excites a sloshing and stretching motion in small dust clouds. A resonance frequency at about 4 Hz was obtained. For higher frequencies, no dust-density wave was excited in a small dust cloud. The stretching motion of the dust cloud is an indication that the confinement potential has an anharmonic component, because, for a harmonic confinement potential, only a rigid-body motion would be excited [165]. However, the resonance frequency can be estimated by the curvature of the axial confinement potential, which is of about 12.6 Hz. This difference can be ascribed to a weaker confinement potential at the location of the small dust cloud. Since the estimated frequency depends on the local curvature of the confinement potential at the position of the dust cloud.

An interaction of the excited sloshing motion and the self-excited dust-density wave was found in a large dust cloud. There, the motion of the entire dust cloud in axial direction led to a superposition of the sloshing velocity and the phase velocity of the self-excited dust-density wave. It was found that the phase velocity of the observed dust-density wave could be fairly well described by a superposition of the sloshing velocity and the phase velocity of the self-excited wave for low frequencies of $f_{\mathrm{mod}} = (1{-}3)$ Hz. At the far side, a response at twice the excitation frequency was observed. It is supposed that the weaker curvature of the confinement potential at the far side exerts a smaller force to the dust particles when the potential well is moving towards the anode. Then the dust particles might be slowed down more softly due to their inertia.

A synchronization of the self-excited dust-density wave was found over a wide frequency range. For low frequencies of $f_{\mathrm{mod}} = (4{-}12)$ Hz, a subharmonic synchronization was observed. This means that the low frequency modulation excites higher harmonics and the dust-density wave is propagating at multiples of the modulation frequency. But the modulation does not lead to a monochromatic wave, i.e., a regular wave propagation with fixed frequency and wavelength, rather, it leads to a complex wave pattern with varying phase velocity and merging wave fronts caused

by the external modulation.

In contrast, for the modulation of the dust-density wave at high frequencies of $f_{\mathrm{mod}} = (70-140)$ Hz, the wave pattern is found to be more coherent, and a kind of superharmonic synchronization was observed. Here, the high frequency modulation leads to synchronization at a subharmonic of the modulation frequency.

The intermediate range of the frequency modulation reveals also a complex behavior. It was found that it is possible to synchronize the dust-density wave over a frequency range of about $f_{\mathrm{mod}} \approx (16-40)$ Hz. A synchronization at the fundamental over the entire cloud length was observed for frequencies of $f_{\mathrm{mod}} \approx (16-24)$ Hz, despite a narrow shell structure at the cloud boundary which can be attributed to a reflection of the wave front [164] or particle reflection. For the frequency range of $f_{\mathrm{mod}} \approx (26-40)$ Hz, the dust-density wave is also synchronized by the external modulation, but a spatial merging of wave fronts leads to a halving of the frequency and a doubling of the wavelength.

It is suggested that this observation can be explained by the adjustment of the dust-density wave to the boundary of the dust cloud and an influence of nonlinear effects. For the self-excited dust-density wave, a spatial distribution of the mean frequency was found. There, the mean frequency varies gradually from higher frequencies at the anode-facing side to lower frequencies at the far side. It is assumed that such a variation of the frequency could be ascribed to an adjustment of the wave to the cloud boundary. This assumption is supported by a measurement of the dispersion relation of a self-excited dust-density wave, which was recently reported by Nosenko *et al.* [166] in a comparable experimental setup. At low wavenumbers, a cutoff frequency was measured, and this result was ascribed to the particle confinement, which determines a boundary condition. Therefore, an influence of the cloud boundary in the present situation is reasonable as well. For the synchronized dust-density wave, the frequency of the wave is specified by the external modulation and regions with constant frequency are observed. These regions are related by an integer fraction, and the boundary between the regions is determined by the position of wave-front merging. It is suggested that the regions with different frequencies might occur to satisfy the preferred natural distribution of the wave frequency, as found for the self-excited wave. The existence of these regions is allowed by the wave-front merging, and this effect may be attributed to a nonlinear behavior of the medium.

For the modulation of the medium-sized dust cloud, it was found that the dust-density wave could be synchronized over a frequency range of $f_{\mathrm{mod}} \approx (18-40)$ Hz. The obtained dispersion relation suggests a cutoff frequency for the long wavelength limit, which can be explained by boundary effects of the cloud and is understood in terms of waveguide modes [68].

The mechanism of the synchronization of a dust-density wave is not completely solved by now. Based on the observations of the self-excited dust-density wave, which exhibit a complex structure of merging wave fronts and varying phase velocity, it can be concluded that this wave is certainly a self-oscillating system. Additional experiments, which were performed to find characteristic features of the van der Pol oscillator such as periodic pulling, have given no hint to such a type of synchronization. Instead, it is suggested that a parametric excitation due to the variation of the

ion density is a reasonable model. Compared to the low-frequency excitation of the sloshing motion, which can be understood in terms of a adiabatically shifted potential well, the frequency modulation of dust-density waves might be coupled to the wave via the Debye length, which depends on the ion density. Hence, a modulation of the Debye length would also lead to a variation of the wave velocity*.

A different approach of studying the synchronization was made by Williams *et al.* [81, 82]. There, it was concluded that the dust-density wave can be synchronized by the modulation frequency if the corresponding wave lies within the natural (broad) spectrum of the self-excited wave. A possibility of synchronizing the dust-density wave by sub- or superharmonic frequencies was not reported by now.

*Dust acoustic wave velocity: $c_{\mathrm{DAW}} = \frac{\omega}{k} = \omega_{\mathrm{pd}} \lambda_{\mathrm{D}}$

5 Void Formation in Magnetized Plasmas

The void formation in an unmagnetized rf plasma is a well understood mechanism. The principal reason for the appearance of the dust-free region is based on the force balance of the outward-directed ion drag force and the inward-directed electric field force.

In a magnetized plasma, the motion of the plasma components, i.e., electrons, ions and dust particles ($l = \mathrm{e}, \mathrm{i}, \mathrm{d}$) is constrained by the magnetic field, which induces a rotation of the plasma components. The strength of this influence can be characterized by the Hall parameter $h_l = \omega_{\mathrm{c}l}/\nu_{l\mathrm{n}}$, which is the ratio of the cyclotron frequency $\omega_{\mathrm{c}l}$ and the collision frequency $\nu_{l\mathrm{n}}$. The plasma components can perform a complete gyro orbit when $h_l > 1$. However, for even lower values of $h_l > 0.1$ the Hall effect becomes noticeable, whereas a $E \times B$ drift requires large values, $h_l \gg 1$.

The low magnetic fields in the Matilda-II device lead to magnetized electrons and weakly magnetized ions, while the dust particles remain unmagnetized. Therefore, the electrons propagate mainly in direction of the magnetic field (z-direction). The ions are mainly following the electric field line, but they also have a small azimuthal drift component perpendicular to the electric field $\vec{E}$ and the magnetic field $\vec{B}$ due to the Hall effect. This Hall component of the ions is responsible for a torque of the ion drag force and results in new effects in dusty plasma experiments.

For a strong magnetic field, it is possible that the dust particles become magnetized and their gyromotion can be studied [167]. The influence of a weak magnetic field, where the dust particle are unmagnetized and do not perform a gyromotion, on a two-dimensional dust cluster, confined in an rf sheath, was studied by Konopka *et al.* [49]. It was found that the dust cluster performs either a rigid-body rotation or a sheared rotation depending on the discharge parameters. The driving mechanism was attributed to a torque of the ion drag force caused by the magnetic field. Recently, a similar experiment was conducted by Carstensen *et al.* [51]. There it was found that the cluster rotation can be opposite to the local ion Hall-motion. This effect could be explained by a global rotation of the neutral gas background.

The influence of a weak magnetic field on three-dimensional dust clouds in dc plasmas was also investigated [130, 168–170], and it was generally concluded that the ion drag force is responsible for an induced rotation of the dust particles. For instance, in an anodic plasma [130] a dust ball was found to rotate in the direction of the $E \times B$ drift of the ions.

The physical principles of torus-shaped dust clouds with a central dust-free region, i.e., void, are analyzed in this Chapter, which is organized as follows: In Sec. 5.1 the existence of voids in dusty plasmas is described with emphasis on the experi-

mental findings. The experimental results on the existence range and the variation of external plasma parameters of torus-shaped dust clouds as well as the theoretical approaches on the confinement and the particle rotation are presented in Sec. 5.2. In Sec. 5.3 the results are summarizing discussed.

5.1 Void Phenomena in Dusty Plasmas

The first observation of a void was described in an rf plasma with nanometer-sized carbon particles in terms of a "great void mode", where the void was azimuthally rotating [52]. The nanometer-sized dust particles fill the plasma volume, because the weight force is so small that sedimentation in the rf sheath becomes negligible; but a direct observation of single particles is not possible because of the small particle size.

A void surrounded by micrometer-sized dust particles was described in rf plasmas under microgravity conditions [54, 57]. There, the force of gravity is absent and the particle fill the plasma except for a region in the center of the chamber. Contrary to the "great void mode" a stable void boundary can be observed. Due to the ambipolar diffusion, which is the main loss mechanism in low-pressure discharges, the ions are streaming from the center outwards to the chamber walls, and by means of Coulomb collisions transfer a momentum on the dust particles. Therefore, the dust particles are pushed out of the central region until an inward-directed electric field force balances that ion drag force.

Besides the experiments under microgravity conditions, it is also possible to study three-dimensional dust clouds by applying a thermophoretic force, via a temperature gradient, that is able to counterbalance the gravitational force [56].

The void formation in the rf discharge was also studied theoretically [57, 171–173] as well as in terms of simulations [174–176]. Recently, the closure of the void under microgravity conditions was reported [58] and also described by means of simulations [59].

A similar observation of a void was found around negatively biased Langmuir probes [177–179], which were positioned in a dust cloud. The mechanism of the void formation is similar to the void formation under microgravity, but the ion drag force points inward and the electric field force outward.

5.2 Torus-Shaped Dust Clouds

The discovery of torus-shaped dust clouds was surprising [180, 181], but the mechanism of the formation was not studied in detail so far. The dust particles rotate about the major axis of the torus and a dust-free region in the center appears, which corresponds to a formation of a void in a weakly magnetized plasma. For the understanding of the responsible mechanisms, a systematic analysis of the experimental conditions is needed, and the forces, which are accountable for the formation of the torus-shaped dust cloud, are of particular interest.

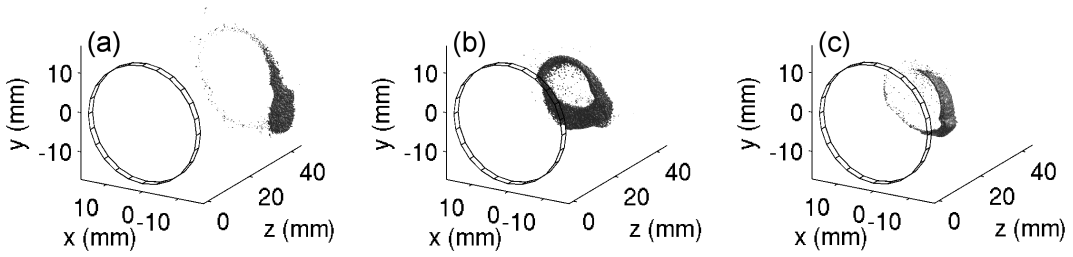

Figure 5.1: Overview of the formation of a torus-shaped dust cloud. The three-dimensional reconstruction of a dust cloud is shown for varying magnetic field strength of (a) low $B = 10$ mT, (b) medium $B = 20$ mT, and (c) high magnetic field strength $B = 74$ mT. A torus exists for a medium magnetic field strength, whereas for lower and higher values a, in direction of the ion Hall motion, shifted dust cloud with few particles rotating about the torus axis is observed. (From Appendix B.2)

Therefore, the behavior of the torus-shaped dust clouds is studied regarding the variation of external plasma parameters. Moreover, it is the aim to develop a simple model that describes, in principle, the mechanism of the formation of a torus-shaped dust cloud and the streaming of dust particles.

5.2.1 Experimental Results

By reason of the knowledge that the ion drag force in combination with a weak magnetic field is able to exert a torque on a dust cloud, which causes a rotation of it, the formation of the torus-shaped dust clouds depending on the magnetic field, and hence the strength of the Hall component of the ion drag force, is of specific interest. Therefore, the shape of a torus-shaped dust cloud is studied with respect to the variation of the magnetic field strength, while other discharge parameters ($p \approx 5.4$ Pa, $P_{\mathrm{rf}} = 3$ W, $U_{\mathrm{A}} \approx 65$ V) were kept constant, whereas the anode current I_{A} adjusts itself to a set of discharge parameters. The three-dimensional structure of the cloud was reconstructed using a vertical scanning technique, which is described in Appendix B.2, and the results of the reconstruction are shown in Fig. 5.1.

For a low magnetic field strength of $B = 10$ mT ($I_{\mathrm{A}} = 14.1$ mA), no fully-formed torus is observed. Instead, an azimuthally shifted dust cloud is found, where only a few particles are rotating about the torus axis. A nearly symmetric torus-shaped dust cloud with balanced branches is found for a medium magnetic field strength of $B = 20$ mT ($I_{\mathrm{A}} = 12.3$ mA). For higher magnetic field strength $B = 74$ mT ($I_{\mathrm{A}} = 4.8$ mA), the branches of the torus-shaped dust cloud become asymmetric again.

By switching the polarity of the magnetic field, it could be shown that the azimuthal component, i.e., the Hall component, of the ion drag force determines the direction of the displacement of the cloud as well as the direction of the particle streaming. Since, for an inverted magnetic field, the dust cloud is shifted in the opposite direction (see Fig. 3 of Appendix B.2).

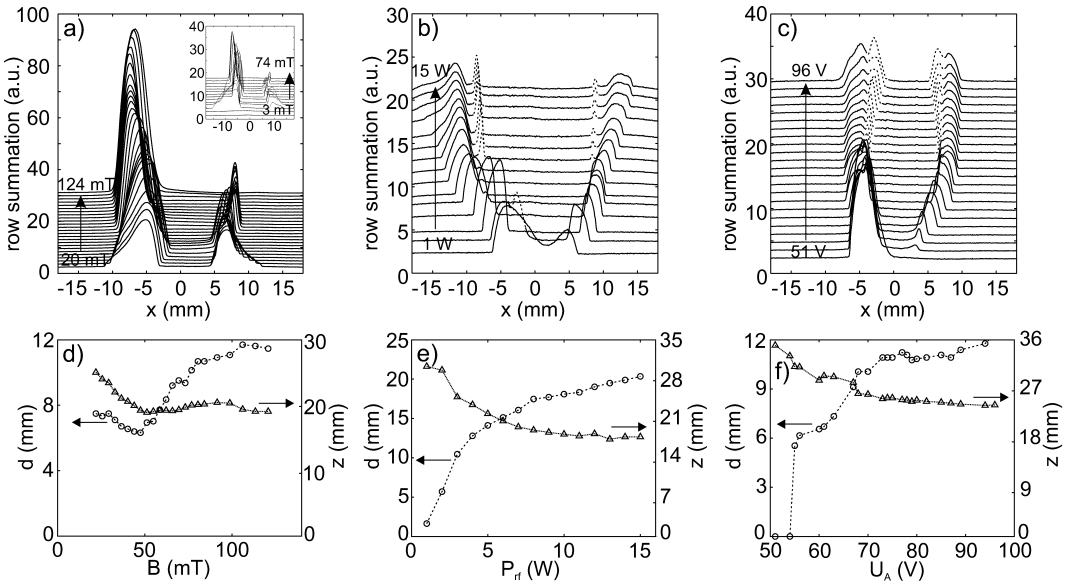

Figure 5.2: Waterfall diagrams of the integral dust-density distribution for a variation of (a) the magnetic field, (b) the primary discharge rf power, and (c) the anode voltage. The void diameter d (circles) and the axial distance z (triangles) of the torus from the anode are shown for (d) the magnetic field variation, (e) the rf power variation and (f) the anode voltage variation. An increase of the magnetic field leads to an increase of the void diameter, whereas the branches become strongly asymmetric. With rising rf power, and hence, increasing ion density, the void diameter increases and the torus branches remain nearly symmetric. The rise of the anode voltage leads to a reduction of the asymmetry of the torus branches, and the void diameter increases until a saturation is reached. (From Appendix B.2)

Dependence of Torus-Shaped Dust Clouds on External Parameters: To gain a comprehensive overview of the formation of a torus-shaped dust cloud while varying the discharge parameters, i.e., magnetic field, rf power and anode voltage, a fixed midsection was chosen to observe the dust cloud. The interesting quantities of the torus-shaped dust cloud are its axial position, void diameter and the time-averaged dust density of the torus branches. For a qualitative representation of the differences, the intensity of time-averaged images is summed up along the z-direction. The resulting intensity profile is a measure of the dust-density distribution of the torus branches. For an overview, the results of the parameter variation are compiled in terms of a waterfall diagram in Figs. 5.2 (a)-(c) for varied magnetic field, rf power and anode voltage. The typical discharge parameters were pressure $p = 5.4$ Pa, magnetic field $B = 20$ mT, rf power $P_{\mathrm{rf}} = 3$ W and anode voltage $U_{\mathrm{A}} = 67$ V. A more quantitative analysis of the diameter of the void (circles) and the axial distance z of the center of mass of the dust cloud (triangles) is shown in Figs. 5.2 (d)-(f).

In Figs. 5.2 (a) and (d) the results obtained for the magnetic field variation are shown. The inset shows a second measurement of the parameter variation. For both variations the same general behavior is found. At low magnetic field strengths the branches are nearly symmetric in shape. For an increasing magnetic field the

torus-shaped dust cloud becomes asymmetric with an enhanced intensity in the left branch of the torus. In Fig. 5.2 (d) it is seen that the diameter of the torus increases with the magnetic field strength until a constant value of about 11 mm is reached. The distance of the torus-shaped dust cloud from the anode decreases down to a constant value of about 20 mm.

The changes of the torus-shaped dust cloud on a variation of the rf power is shown in Figs. 5.2 (b) and (e). For a low rf power of 1 W two peaks can be seen but the center is not dust-free. These peaks are separating with increasing rf power, and represent the intersection with the formed torus. For low rf power, the torus is asymmetric and the left peak has a larger amplitude than the right one. For even higher rf power, the torus-shaped dust cloud becomes nearly symmetric. However, two additional peaks (dashed peaks) also appear, and represent a secondary torus that is located between the anode and the primary torus. This secondary torus is of smaller diameter and it contains much finer dust particles that, e.g., originate from sputtering of the monodisperse melamine particles. The presence of the secondary torus was neglected for the quantitative measure of distance and diameter, which are shown in Fig. 5.2 (e). The diameter of the torus-shaped dust cloud continuously increases with rising rf power, whereas for higher rf power the slope decreases and a trend towards a constant value can be suggested. The distance from the anode decreases while the rf power is increased until a constant value of approximately 18 mm is reached.

In Figs. 5.2 (c) and (f) the diagrams for the variation of the anode voltage are shown. These measurements were directly performed after the variation of the rf power. Hence, finer dust particles are still present and form also a secondary torus-shaped dust cloud (dashed peaks). For a low anode voltage of 51 V, only a displaced dust cloud is observed. For higher anode voltages, a torus-shaped dust cloud is formed with nearly symmetric branches. The diameter of the primary torus increases with increasing anode voltage up to a value of $d \approx 12$ mm, and the distance from the anode decreases until a value of about 24 mm is reached.

Streaming of Dust Particles along the Torus: The mean velocity of the streaming dust particles was determined using a particle image velocimetry (PIV) algorithm. For the analysis the software package MatPiv [182] was chosen. As previously described, the torus-shaped dust cloud was mainly observed in horizontal sections. Because of this observation geometry, only the horizontal velocity component is obtained. Nevertheless, it is reasonable to assume that in a top and a bottom section the velocity is mainly defined by its horizontal component, and the vertical component is small compared to the horizontal component.

The results of the analysis are shown in Fig. 5.3 for (a) the top section and (b) the bottom section, as sketched in the insets. The image axis are scaled in millimeters but do not refer to the position of the anode. The measurements of the velocity confirm the rotation of dust particles. In the top section, a positive sign of the velocity is found, and in the bottom section the sign of the velocity is inverted. Thus, the particles are flowing in opposite direction in the top and the bottom section. Furthermore, a velocity gradient with increasing velocity in flow

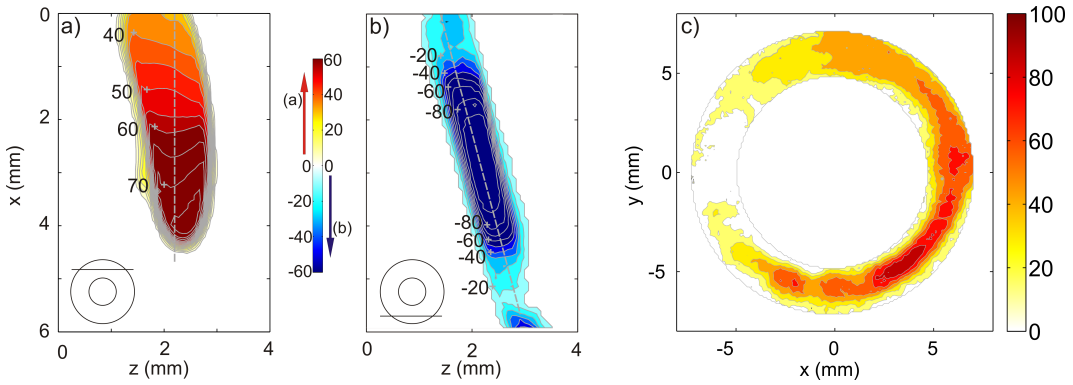

Figure 5.3: Particle-image-velocimetry (PIV) measurement of the horizontal component of the particle velocity (a) in the upper part and (b) in the lower part of the torus, as indicated by the insets. (c) Vertical PIV measurement of the velocity for a different torus-shaped dust cloud. A pronounced velocity gradient along the torus is found. (Adapted from Appendix B.2 and Ref. [121])

direction, i.e., in direction towards larger x values, is obtained. It is found that the slope is linear. Different from this finding, the velocity profile in the bottom section is parabolic with a negative extremum. The absolute value of the velocity is found higher in the bottom section ($|v_{\max}| \approx 100$ mm s^{-1}) than in the top section ($|v_{\max}| \approx 80$ mm s^{-1}).

In Fig. 5.3 (c) a measurement of a vertical section through a torus-shaped dust cloud is shown. Here, the absolute value of the velocity is presented. A similar gradient of the velocity in the top section is found. For the down-streaming particles, i.e., the right branch, the particle velocity is further increased. A maximum value of the velocity is found close to the "five o'clock" position and is about 90 mm s^{-1}. Then, the velocity decreases and even a velocity close to zero at the "nine o'clock" position for the up-streaming branch is observed.

5.2.2 Model of the Torus-Shaped Dust Cloud

For the understanding of the formation of a torus-shaped dust cloud, a single-particle model to describe the particle motion is proposed. The acting forces on a dust particle are sketched in Fig. 5.4, and the origin of the rotation angle φ is defined at the "nine o'clock" position with increasing angle in clockwise direction. The forces are splitted up into a radial component and an azimuthal component. The radial components (10^{-13} N) of the acting forces are larger than the azimuthal components (10^{-14} N). The confinement of the particles is determined by the radial forces (first-order approximation), whereas the streaming of the dust particles is caused by the azimuthal components (second-order approximation). In this sense, the proposed model gives a hierarchy of processes involved.

Confinement of Torus-Shaped Dust Clouds: The axial confinement of dust particles is described, in Sec. 2.2.3, by a force equilibrium of electric field force

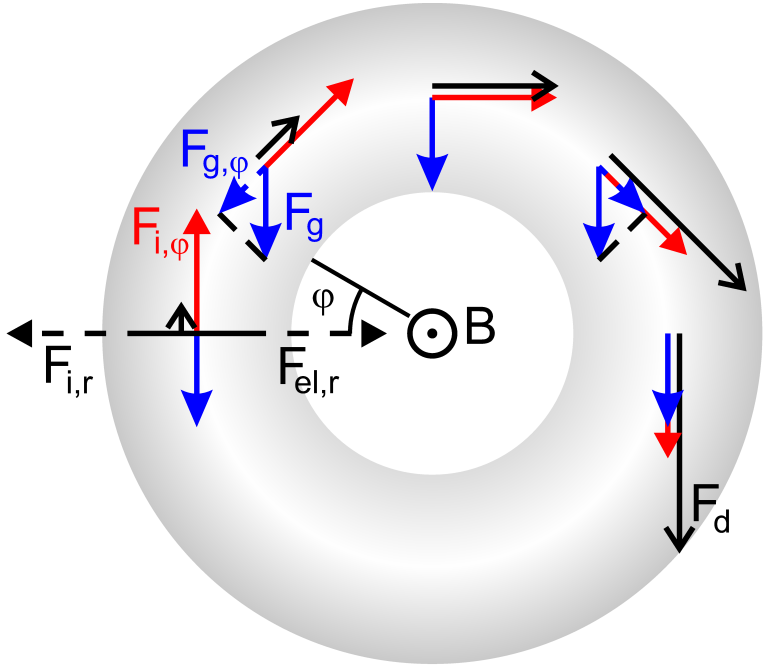

Figure 5.4: A sketch of the forces acting on dust particles, which are confined within a torus-shaped dust cloud. The first-order approximation describes the force equilibrium given by the radial component of the ion drag force $F_{\mathrm{i,r}}$ and the electric field force $F_{\mathrm{el,r}}$. The second-order approximation describes the driving mechanism of the rotation of dust particles about the torus axis. The azimuthal component of the ion drag force $F_{\mathrm{i},\varphi}$ has to exceed the gravitational force F_{g} at the position of "nine o'clock". The rotation angle φ has its origin at "nine o'clock", and the angle increases in clockwise direction. The gravitational force $F_{\mathrm{g},\varphi}$ depends on the rotation angle, whereas the absolute value of the azimuthal component of the ion drag force is constant for any angle position. The resulting force F_{d} on a dust particle is depicted.

and ion drag force [98]. The confinement potential is calculated along the central axis. In case of the torus-shaped dust clouds, it is found that no dust particles are confined there. Instead, a dust-free region is observed. For a calculation of the force equilibrium, the forces have to be calculated along the flow direction of the ions, i.e., along the electric field lines.

A measurement of the plasma potential obtained with an emissive probe is shown in Fig. 5.5 (a). The electric field lines are indicated with arrows, whereas the length of an arrow represents the electric field strength. Additionally, two electric field lines are highlighted to reflect the curvature of the electric field, and hence, the main flow direction of the ions.

The ion drag force is calculated using Hutchinson's formula, Eq. (2.23), in streaming direction of the ions, Eq. (2.25).

A radial profile of the total forces is shown in Fig. 5.5 (b). The axial position is indicated in Fig. 5.5 (a) by a dashed vertical line. The distance is chosen at $z = 25$ mm, where the torus was found. Here, the ion drag force is shown for three different ion densities of $n_{\mathrm{i}} = 4 \times 10^{14}$ m^{-3} ($\bigtriangledown$), $n_{\mathrm{i}} = 6 \times 10^{14}$ m^{-3} ($\Diamond$) and

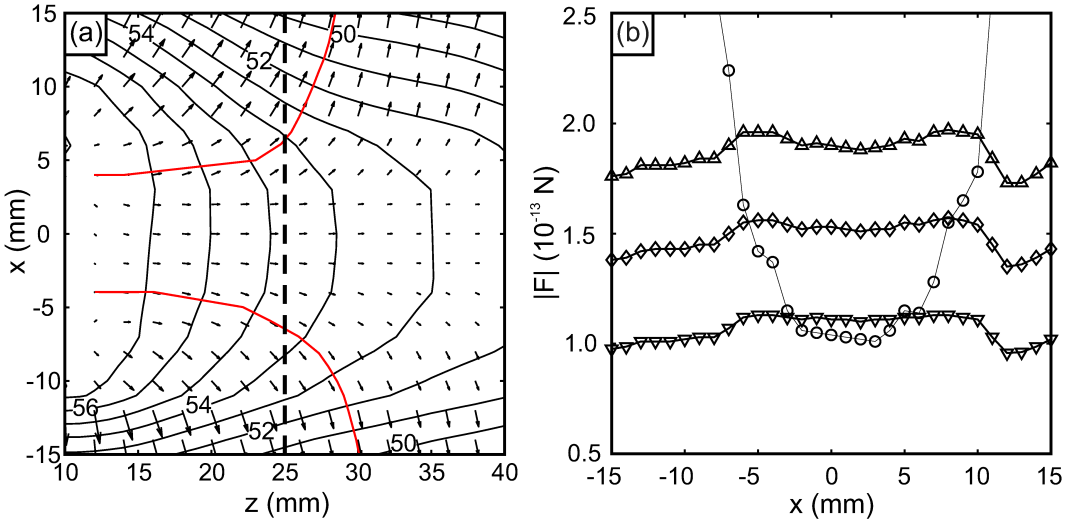

Figure 5.5: (a) Measurement of the plasma potential. The plasma potential is given in units of volts. The electric field lines are indicated by arrows and the length is a measure of the field strength. Two examples of electric field lines are given by the red lines. (b) Total electric field force (○) and total ion drag force plotted vs. x at an axial distance $z = 25$ mm, as indicated by a dashed line in (a). The ion drag force is shown for different ion densities of $n_\mathrm{i} = 4 \cdot 10^{14}$ m^{-3} (▽), $n_\mathrm{i} = 6 \cdot 10^{14}$ m^{-3} (◊), and $n_\mathrm{i} = 8 \cdot 10^{14}$ m^{-3} (△). (Adapted from Appendix B.2)

$n_\mathrm{i} = 8 \times 10^{14}$ m^{-3} (△). The electric field force (○) has a parabolic shape with a steep slope at the outer edges of the anodic plasma. In the central region, the ion drag force exceeds the electric field force, so that the particles are pushed out of this region. Due to the steep slope of the electric field force, the intersection of the ion drag force and the electric field force is less dependent on the ion density. However, the ion density determined for the experimental conditions is the mean value of the shown ion densities. The intersection points are at approximately 7 mm. This value is in agreement with the location of the torus branches found in the experiment.

Model of the Azimuthal Dust Particle Motion: In first-order approximation, the force equilibrium is described by the radial component of the ion drag force $F_\mathrm{i,r}$ and the opposing electric field force $F_\mathrm{el,r}$. The azimuthal component of the forces are not taken into account for the approximation of the force balance.

In second-order approximation, it is suggested that the azimuthal ion drag force is responsible for the streaming of the dust particles along the torus. This force is balanced by the gravitational force, and for an onset of the streaming of dust particles the azimuthal component of the ion drag force has to exceed the gravitational force $F_\mathrm{g} = 0.6 \times 10^{-14}$ N at an angle of $\varphi = 0°$ (nine o'clock).

The azimuthal component of the ion drag force is constant for all angular positions. Contrariwise, the gravitational force varies in azimuthal direction with the angle φ, $F_{\mathrm{g},\varphi} = -F_\mathrm{g} \cos(\varphi)$. At the upward-streaming branch, the gravitational and the azimuthal ion drag force are opposing; whereas at the downward-streaming branch,

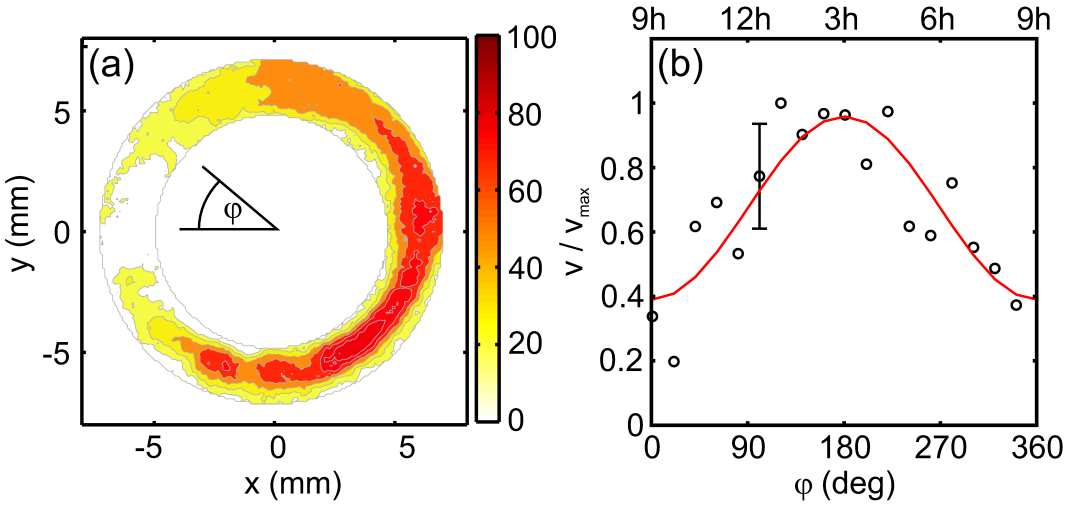

Figure 5.6: (a) PIV measurement within the vertical observation geometry. The absolute values of the rotation velocity are given in units of millimeter per second. The origin of the rotation angle φ is at "nine o'clock" position and the angle increases in clockwise direction, which agrees with the flow direction of the dust particles. (b) The velocity at different angular positions is plotted vs. the rotation angle. The velocity is normalized to its maximal value and the theoretical angular velocity (red line) is shown. (Adapted from Refs. [121, 183])

they are parallel. It is obvious that a minimum value of the ion drag force is required to overcome the gravity in the "nine o'clock" position. This defines a threshold condition, which separates the state of an azimuthally displaced compact cloud from a torus-shaped dust cloud. At the top and the bottom section, the gravitational force is perpendicular to the streaming direction and does not contribute to the streaming velocity of the particles.

The threshold condition can also be used to estimate the particle velocities: Suggesting that the azimuthal ion drag force has at least to be equal to the value of the gravitational force, it is possible to estimate the expected velocity of a dust particle. The forces acting on a dust particles are given by

$$F_{\mathrm{i},\varphi} + F_{\mathrm{g},\varphi} + F_{\mathrm{n}} = 0 \ . \tag{5.1}$$

Here, the azimuthal ion drag force $F_{\mathrm{i},\varphi}$ and the gravitational force $F_{\mathrm{g},\varphi}$ is balanced by the neutral gas friction $F_{\mathrm{n}} = -m_{\mathrm{d}}\beta v_{\mathrm{d},\varphi}$, Eq. (2.15).

A typical value of the azimuthal component of the ion drag force is $F_{\mathrm{i},\varphi} = 0.8 \times 10^{-14}$ N. This leads to an azimuthal velocity of a dust particle of $v_{\mathrm{d},\varphi} \approx (60{-}420)$ mm s^{-1} depending on the angular position. For the top ($\varphi = 90°$) and the bottom position ($\varphi = 270°$) a value of 240 mm s^{-1} is found. In the downward-streaming direction ($\varphi = 180°$) the dust velocity has its largest and in the upward-streaming direction ($\varphi = 0°$) its lowest value.

Comparing this value with the one obtained in the experiment in the top and bottom section [$v_{\mathrm{d},\varphi} \approx (80{-}100)$ mm s^{-1}], it is found that they are of the same order of magnitude but a factor of about three larger.

The vertical observation geometry allows a more detailed analysis of the streaming velocity of the dust particles. In Fig. 5.6 (a), the PIV measurements within the vertical section is shown again. Here, the absolute value of the particle velocity is color-coded, keeping in mind that the streaming direction is in clockwise direction. The measured velocities are in agreement with the one obtained in the horizontal top and bottom section, respectively. The particle velocities at different angular positions are shown in Fig. 5.6 (b). Here, the velocity obtained by the PIV measurement is plotted vs. the angle φ. The velocities are normalized by its largest value, and a cosine function (red line) showing the expected theoretical behavior is displayed. In general, the theoretical curve resembles the obtained curvature of the velocity. But the theoretically expected values of the velocities are still too large, and the maximum of the rotation velocity is found at an angular position of about 240° (five o'clock).

5.3 Discussion

The description of the torus-shaped dust clouds in terms of a single-particle model makes predictions for the confinement, the onset of particle streaming, and the expected velocities. The model is hierarchical with two orders of approximation based on the magnitude of the acting forces.

In the first-order approximation, the confinement of dust particles is described in terms of the force equilibrium on a dust particle by the large force components of the ion drag force and the electric field force in the $x-z$ plane. The force equilibrium is calculated along the electric field lines, i.e., the streaming direction of the ions. It was found that the ion drag force exceeds the electric field force in axial direction; thus, dust particles cannot remain there. Instead, an equilibrium position of the forces at $|x| \approx 7$ mm is found, which is in agreement with the location of the torus branches.

In the second-order approximation, the mechanism of the particle streaming is described by the minor forces of the azimuthal ion drag force and the gravitational force. There, a threshold exists for the onset of the particle streaming. The threshold is defined by an exceeding of the azimuthal ion drag force $F_{\mathrm{i},\varphi}$ on the dust particle to its gravitational force F_{g}. This assumption gives a minimum value for the azimuthal ion drag force, and hence, an estimate for the particle velocity. However, the estimated velocity of a dust particle is by a factor of about three larger than the measured velocity. A reason for this difference could be "collective effects" between the dust particles, e.g., the Coulomb repulsion. These effects are not considered in the single-particle model, which would reduce the threshold condition and the corresponding velocity scale.

The variation of the particle velocity in angular direction can be generally described in terms of the single-particle model. The influence of the gravitational force varies with the angular position, because only the component in azimuthal direction has to be considered for the driving mechanism of a dust particle. This leads to a cosine modulation of the particle velocity, which is in good agreement

with the measured velocity distribution. A small difference remains with respect to the angular position of the maximum speed, which is at the "three o'clock" position in the single-particle model and at the "five o'clock" position in the experiment.

The crucial parameter for the formation of a torus-shaped dust cloud is the azimuthal ion drag force. This force varies with the product of the radial electric field strength and the magnetic field strength and with the ion density. A variation of the radial electric field strength does not lead to a considerable change in the ion drag force, therefore this influence can be neglected. Whereas an increase of the magnetic field strength would lead to an increase of the ion drag force for constant ion density. But, as described in Sec. 2.2, the ion density depends non-monotonously on a variation of the magnetic field with a maximum of the ion density at a magnetic field strength of about 20 mT. When the magnetic field is further increased, the ion density decreases until a constant value is reached. Hence, the correlation of the ion density and the magnetic field strength explains why the torus-shaped dust cloud disappears for higher magnetic field strength.

In comparison to the void formation in unmagnetized rf discharges (i.e., under microgravity conditions [54, 57, 174–176], studying nanometer-sized particles [52, 184], and around Langmuir probes [177–179]), the formation of the described torus-shaped dust cloud in a weakly magnetized anodic plasmas reveals one basic similarity. The general mechanism of the void formation, and hence, the determination of the equilibrium position of the void edge, is the same and defined by the force equilibrium of the electric field force and the opposing ion drag force. This aspect is included in the single-particle model in the first-order approximation, which describes the confinement condition in terms of the mentioned force equilibrium. The new aspect of the torus-shaped dust cloud is that the visibility of the void is due to the fact that the dust particles are streaming via an azimuthal component of the ion drag force, which is caused by the magnetic field, acting as the driving force. The streaming of the dust particles is only present if a threshold ($F_{\mathrm{i},\varphi} > F_{\mathrm{g}}$) is exceeded. When the threshold is not exceeded, only an out of the central region shifted dust cloud is found.

6 Summary and Conclusions

In this work, the dynamical properties of dust clouds in a magnetized anodic plasma for naturally occurring motions, i.e., self-excited dust-density waves and dust-particle rotation, were studied. Moreover, the influence of an external modulation on the dynamics of dust-density waves was of particular interest. The dust clouds were classified into two structures, forming so-called compact and torus-shaped dust clouds. The response of compact dust clouds to an external modulation was investigated in terms of a sloshing motion of the entire dust cloud and synchronization of dust-density waves over a large frequency range, which includes sub- and superharmonic synchronization regions. Furthermore, the formation of torus-shaped dust clouds was experimentally investigated regarding a variation of the discharge parameters. By means of a hierarchical single-particle model, the mechanism of both the formation of a torus-shaped dust cloud and the onset of particle rotation about the torus axis could be clarified.

Self-Excited Dust-Density Waves in Compact Dust Clouds: The dust-density waves in compact dust clouds are spontaneously excited. It was found that the dust cloud has to exceed a minimum size of at least one typical wavelength for wave emergence. It is pointed out that the self-excited wave can be understood in terms of the self-oscillations described in nonlinear dynamics. The energy to feed the wave is provided by the ion streaming through a two-stream instability of Buneman-type [185, 186]. The damping of the wave is determined by the neutral gas friction. Such a nonlinear coupling of damping and feeding is observed in many plasma situations.

The self-excited dust-density wave was found as an incoherent wave pattern. In general, two mechanisms can be deduced for the occurrence of the local frequency and wavenumber: First, a variation of the phase speed, and second, defect structures, in which wave-front merging occurs. The latter effect is predominant, whereas the variation of the phase velocity leads to a weaker disturbance of the wave pattern.

Three-Dimensional Structure of Wave Fronts and Finite Size Effects: It was possible to reconstruct the three-dimensional structure of the wave fronts of medium-sized and large dust clouds by applying the technique of synchronization. It was found that, at larger distances from the anode center, the wave propagates at an inclination angle. This behavior is explained by the fact that the propagation direction of the wave coincides with the electric field direction, and therewith the streaming direction of the ions.

Finite size effects were identified by a cutoff frequency at the long wavelength limit in terms of a waveguide-mode theory [68]. The cutoff frequency explains the

difference of phase and group velocity.

Sloshing Motion of Dust Clouds: It was possible to excite a sloshing motion of a small dust cloud at low frequencies. This sloshing motion is accompanied by a stretching motion and a resonance-like behavior with a resonance frequency at about 4 Hz is found. The stretching motion indicates that the confinement potential has an anharmonic component. Otherwise, a rigid-body motion of the dust cloud should have been observed. The measurement of a resonance curve shows that, at low modulation frequencies, the dust cloud behaves like a driven harmonic oscillator, which is a linear oscillator.

An interaction of the sloshing motion and a self-excited dust-density wave in a large dust cloud was found for low frequencies of (1−3) Hz. The observed wave pattern is fairly well described by a superposition of both motions. It is reasonable to relate the excess of the wave velocity over the sum of the linear effects to an exchange of energy from the accelerated potential well and the dust cloud, which might be similar to the speedup that a spacecraft can gain in a swing-by maneuver with a planet.

Synchronization of Dust-Density Waves: The synchronization of the dust-density wave in a large dust cloud has revealed a complex dynamic. First, at low modulation frequencies, the interaction of the sloshing and wave motion in terms of a linear superposition was found, but also a subharmonic synchronization of the wave was observed, which is a nonlinear effect. However, the space-time diagram revealed an irregularly propagating wave, and the spectra have shown various components at multiples of the modulation frequency. Thus, the complex wave pattern has its origin in the interplay of the large number of frequency components.

Second, the range of harmonic synchronization, where the dust-density wave is synchronized at the modulation frequency over the entire dust cloud, covers only a small frequency range of (14−24) Hz. For larger frequencies, a spatial wave decay to the subharmonic of the modulation frequency is observed, which is accompanied by a doubling of the wavelength. It is suggested that this effect is intimately related to the gradual distribution of the mean frequency of the self-excited dust-density wave. The observed monotonous variation of the mean frequency can be described by the properties of the medium, e.g., the dust-density profile or boundary effects. For instance, Nosenko *et al.* [166] have attributed their measurement of a cutoff frequency, for a self-excited dust-density wave in a large dust cloud, to the particle confinement, which defines the properties of the cloud boundary. The external modulation causes a synchronized state of the dust-density wave, and the previously gradual variation of the frequency has changed to regions with constant frequency that are separated by merging of wave fronts. These regions are related by an integer fraction, and the preference to form such regions could be ascribed to an effect of the nonlinearity of the system.

Finally, the modulation at high frequencies has shown that a superharmonic synchronization is also possible. At least, the external modulation leads to a more coherent wave pattern compared to the self-excited dust-density wave.

This complex findings modify the generally expected model of linear waves, where the external modulation specifies the frequency of the wave and the wavelength adjusts to the variation of the inhomogeneous medium. For the nonlinear waves in the present experiment other rules apply: Different regions of the wave field can synchronize to different multiples of the modulation frequency. The coexistence of these regions are allowed by the process of wave-front merging.

In addition, it is worth mentioning that nonlinear waves that are excited by a Buneman-type instability still fulfill the linear dispersion relation to a good degree of accuracy [187]. Thus, an effect of nonlinearity does not contradict the comparison of the dispersion properties with linear models.

On the Coupling of the External Modulation to the Cloud Dynamics: The main influence of the external modulation on the plasma parameters of the anodic discharge is a periodical modulation of the ion density and therewith the ion drag force. The variation of the ion drag force would lead to a periodically shifted confinement potential. Such a modulation of an internal parameter is known as parametric excitation. A specific feature of a parametric oscillator is the existence of instability regions for sub- and superharmonic frequencies of the eigenfrequency. Therefore, the mechanism of a parametric excitation is a possible and reasonable process for the coupling.

Formation of Torus-Shaped Dust Clouds: The torus-shaped dust clouds were qualitatively and quantitatively analyzed for a variation of the external discharge parameters. A transition from an azimuthally shifted dust cloud to a fully-formed torus-shaped dust cloud was observed. The azimuthal ion drag force, which is caused by the magnetic field, is responsible for this shift and the particle rotation about the major axis of the torus.

The mechanism of the formation of a torus-shaped dust cloud is understood in terms of a single-particle model with a hierarchical order of forces. The first order determines the confinement of the torus-shaped dust cloud by the electric field force and the ion drag force in the $x-z$ plane. The second-order approximation defines the threshold condition for the onset of particle streaming. It is found that the threshold is determined by the gravitational force, and the azimuthal component of the ion drag force has to exceed this threshold for an onset of the particle streaming.

The experimental results are in good agreement with the estimated void diameter. The calculated particle velocities, however, are overestimated by the single-particle model, while the general behavior of the velocity distribution is well described. It can be concluded that the general mechanism of the void formation, in comparison to rf discharges and around Langmuir probes, is preserved while for the formation of the void the torque of the ion drag force is essential, because the dust particles have to be lifted against the gravitational field.

In this thesis two different dynamical states of dust clouds, i.e., dust-density waves and streaming of dust particles in torus-shaped dust clouds, were studied. At first glance, both situation appear unrelated. Nevertheless, the mechanism of the dy-

namics is similar. It can be summarized that the driving force for the motion of dust particles is caused by the streaming of ions and the transfer of momentum by ion drag. The flow direction of the ions is mainly directed along the electric field lines, but a small azimuthal motion, which originates from the weak magnetic field, is present. In case of the dust-density wave, the influence of the azimuthal component is negligible, and the wave activity is defined by the resonant coupling with ions streaming along the electric field lines. On the contrary, for the formation of torus-shaped dust clouds both components of the ion motion become essential in terms of the ion drag force. The major component defines the equilibrium position and therewith the void diameter, whereas the minor component is responsible for the streaming of the dust particles.

The investigations on the synchronization of dust-density waves have shown that the dynamical response of the wave is an interesting topic itself for studying the dynamic by means of techniques of nonlinear dynamics. For instance, the influence of noise on a self-excited dust-density wave could lead to a coherent wave pattern via stochastic resonance. Moreover, the experiments focused on the mechanism of synchronization have just started, and further interesting results regarding the synchronization could be expected. For the understanding of the synchronization of dust-density waves, it would also be beneficial to study the effect of an external modulation by means of analytical models or simulations.

The basic mechanism of the formation of torus-shaped dust clouds is described by means of the hierarchical single-particle model. However, differences between the model and the experimental findings still exist. A possible reason could be collective effects like Coulomb forces between the dust particles. Modelling of torus-shaped dust clouds by means of computer simulation will certainly help clarifying the remaining questions.

In conclusion, the streaming of ions and the influence of a momentum transfer of the ions are of particular importance for the understanding of different types of dust clouds and the observed particle motion. The emergence of dust-density waves is caused by the resonant coupling of ions via a two-stream instability. The main influence on the process of synchronization was ascribed to the variation of the ion density by the external modulation. Such a variation leads to an adiabatically shifted potential well and to a modulation of the Debye length, which varies the phase velocity of a dust-density wave. For the formation of torus-shaped dust clouds with a void in the center, the ion drag force determines the equilibrium position of the void edge in balance with the electric field force. Moreover, the Hall component of the ion drag force is essential for the streaming of dust particles and the appearance of the void.

A Bibliography

[1] C. K. Goertz. Dusty plasmas in the solar system. *Rev. Geophys.* **27**, 271 (1989).

[2] Ch. Hollenstein. The physics and chemistry of dusty plasmas. *Plasma Phys. Control. Fusion* **42**, R93 (2000).

[3] A. Bouchoule. *Dusty plasmas: physics, chemistry, and technological impacts in plasma processing.* John Wiley & Sons Ltd, New York, 1999.

[4] Dennis M. Manos and Daniel L. Flamm. *Plasma Etching: An Introduction.* Academic Press, San Diego, 1989.

[5] Stephen M. Rossnagel, Jerome J. Cuomo, and William D. Westwood. *Handbook of plasma processing technology: fundamentals, etching, deposition, and surface interactions.* Noyes Publications, Park Ridge, New Jersey, 1989.

[6] J. Winter. Dust: A new challenge in nuclear fusion research? *Phys. Plasmas* **7**, 3862 (2000).

[7] G. Federici, C.H. Skinner, J.N. Brooks, J.P. Coad, C. Grisolia, A.A. Haasz, A. Hassanein, V. Philipps, C.S. Pitcher, J. Roth, W.R. Wampler, and D.G. Whyte. Plasma-material interactions in current tokamaks and their implications for next step fusion reactors. *Nuclear Fusion* **41**, 1967 (2001).

[8] M. Rubel, M. Cecconello, J.A. Malmberg, G. Sergienko, W. Biel, J.R. Drake, A. Hedqvist, A. Huber, and V. Philipps. Dust particles in controlled fusion devices: morphology, observations in the plasma and influence on the plasma performance. *Nuclear Fusion* **41**, 1087 (2001).

[9] J. Winter. Dust in fusion devices - a multi-faceted problem connecting high- and low-temperature plasma physics. *Plasma Phys. Control. Fusion* **46**, B583 (2004).

[10] H. Ikezi. Coulomb solid of small particles in plasmas. *Phys. Fluids* **29**, 1764 (1986).

[11] J. H. Chu and Lin I. Direct observation of Coulomb crystals and liquids in strongly coupled rf dusty plasmas. *Phys. Rev. Lett.* **72**, 4009 (1994).

[12] A. Melzer, T. Trottenberg, and A. Piel. Experimental determination of the charge on dust particles forming Coulomb lattices. *Phys. Lett. A* **191**, 301 (1994).

[13] H. Thomas, G. E. Morfill, V. Demmel, J. Goree, B. Feuerbacher, and D. Möhlmann. Plasma crystal: Coulomb crystallization in a dusty plasma. *Phys. Rev. Lett.* **73**, 652 (1994).

[14] Y. Hayashi and K. Tachibana. Observation of Coulomb crystal formation from carbon particles grown in a methane plasma. *Jpn. J. Appl. Phys.* **33**, L804 (1994).

[15] P. Pieranski. Colloidal crystals. *Contemp. Phys.*, **24**, 25 (1983).

[16] J. E. Hug, F. van Swol, and C. F. Zukoski. The freezing of colloidal suspensions in confined spaces. *Langmuir* **11**, 111 (1995).

[17] H. Löwen. Twenty years of confined colloids: from confinement-induced freezing to giant breathing. *J. Phys.: Condens. Matter* **21**, 474203 (2009).

[18] D. J. Wineland, J. C. Bergquist, Wayne M. Itano, J. J. Bollinger, and C. H. Manney. Atomic-ion Coulomb clusters in an ion trap. *Phys. Rev. Lett.* **59**, 2935 (1987).

[19] F. Diedrich, E. Peik, J. M. Chen, W. Quint, and H. Walther. Observation of a phase transition of stored laser-cooled ions. *Phys. Rev. Lett.* **59**, 2931 (1987).

[20] M. Drewsen, C. Brodersen, L. Hornekær, J. S. Hangst, and J. P. Schifffer. Large ion crystals in a linear Paul trap. *Phys. Rev. Lett.* **81**, 2878 (1998).

[21] Daniel H. E. Dubin and T. M. O'Neil. Trapped nonneutral plasmas, liquids, and crystals (the thermal equilibrium states). *Rev. Mod. Phys.* **71**, 87 (1999).

[22] A. Melzer, V. A. Schweigert, I. V. Schweigert, A. Homann, S. Peters, and A. Piel. Structure and stability of the plasma crystal. *Phys. Rev. E* **54**, R46 (1996).

[23] R. A. Quinn, C. Cui, J. Goree, J. B. Pieper, H. Thomas, and G. E. Morfill. Structural analysis of a Coulomb lattice in a dusty plasma. *Phys. Rev. E* **53**, R2049 (1996).

[24] H. Thomas and G.E. Morfill. Melting dynamics of a plasma crystal. *Nature* **379**, 806 (1996).

[25] H. Totsuji. Structure and melting of two-dimensional dust crystals. *Phys. Plasmas* **8**, 1856 (2001).

[26] A. V. Ivlev, U. Konopka, G. Morfill, and G. Joyce. Melting of monolayer plasma crystals. *Phys. Rev. E* **68**, 026405 (2003).

[27] Daniel H. E. Dubin. The phonon wake behind a charge moving relative to a 2d plasma crystal. *Phys. Plasmas* **7**, 3895 (2000).

[28] O. Havnes, F. Li, F. Melandso, T. Aslaksen, T. W. Hartquist, G. E. Morfill, T. Nitter, and V. Tsytovich. Diagnostic of dusty plasma conditions by the observation of mach cones caused by dust acoustic waves. *J. Vac. Sci. Technol. A* **14**, 525 (1996).

[29] A. Melzer, S. Nunomura, D. Samsonov, Z. W. Ma, and J. Goree. Laser-excited mach cones in a dusty plasma crystal. *Phys. Rev. E* **62**, 4162 (2000).

[30] D. Samsonov, J. Goree, Z.W. Ma, A. Bhattacharjee, H. M. Thomas, and G. E. Morfill. Mach cones in a Coulomb lattice and a dusty plasma. *Phys. Rev. Lett.* **83**, 3649 (1999).

[31] D. Samsonov, J. Goree, H. M. Thomas, and G. E. Morfill. Mach cones in a two-dimensional yukawa solid in a dusty plasma. *Phys. Rev. E* **61**, 5557 (2000).

[32] F. Melandsø. Lattice waves in dust plasma crystals. *Phys. Plasmas* **3**, 3890 (1996).

[33] S. Peters, A. Homann, A. Melzer, and A. Piel. Measurement of dust particle shielding in a plasma from oscillations of a linear chain. *Phys. Lett. A* **223**, 389 (1996).

[34] J. B. Pieper and J. Goree. Dispersion of plasma dust acoustic waves in the strong-coupling regime. *Phys. Rev. Lett.* **77**, 3137 (1996).

[35] M. Zuzic, H. Thomas, and G. E. Morfill. Wave propagation and damping in plasma crystals. *J. Vac. Sci. Technol. A* **14**, 496 (1996).

[36] A. Homann, A. Melzer, S. Peters, R. Madani, and A. Piel. Laser-excited dust lattice waves in plasma crystals. *Phys. Lett. A* **242** 173 (1998).

[37] T. Misawa, S. Nunomura, N. Ohno, and S. Takamura. Observation of transverse dust lattice wave excited by unstable vertical oscillations of dust particles in an ion sheath with low gas pressure. *Jpn. J. Appl. Phys.* **39**, 551 (2000).

[38] M. S. Murillo. Critical wave vectors for transverse modes in strongly coupled dusty plasmas. *Phys. Rev. Lett.* **85**, 2514 (2000).

[39] S. Nunomura, D. Samsonov, and J. Goree. Transverse waves in a two-dimensional screened-Coulomb crystal (dusty plasma). *Phys. Rev. Lett.* **84**, 5141 (2000).

[40] S. Nunomura, D. Samsonov, S. Zhdanov, and G. Morfill. Heat transfer in a two-dimensional crystalline complex (dusty) plasma. *Phys. Rev. Lett.* **95**, 025003 (2005).

[41] V. A. Schweigert and F. Peeters. Spectral properties of classical two-dimensional clusters. *Phys. Rev. B* **51**, 7700 (1995).

[42] W.-T. Juan, Z.-H. Huang, J.-W. Hsu, Y.-J. Lai, and Lin I. Observation of dust Coulomb clusters in a plasma trap. *Phys. Rev. E* **58**, R6947 (1998).

[43] O. Arp, D. Block, and A. Piel. Dust Coulomb balls: three dimensional plasma crystals. *Phys. Rev. Lett.* **93**, 165004 (2004).

[44] O. Arp, D. Block, M. Klindworth, and A. Piel. Confinement of Coulomb balls. *Phys. Plasmas* **12**, 122102 (2005).

[45] Y.-J. Lai and Lin I. Packing and defects of strongly coupled two-dimensional Coulomb clusters: numerical simulation. *Phys. Rev. E* **60**, 4743 (1999).

[46] A. Melzer, M. Klindworth, and A. Piel. Normal modes of 2d finite clusters in complex plasmas. *Phys. Rev. Lett.* **87**, 115002 (2001).

[47] S. G. Amiranashvili, N. G. Gusein-zade, and V. N. Tsytovich. Spectral properties of small dusty clusters. *Phys. Rev. E* **64**, 016407 (2001).

[48] M. Klindworth, A. Melzer, A. Piel, and V. A. Schweigert. Laser-excited intershell rotation of finite Coulomb clusters in a dusty plasma. *Phys. Rev. B* **61**, 8404 (2000).

[49] U. Konopka, D. Samsonov, A. V. Ivlev, J. Goree, V. Steinberg, and G. E. Morfill. Rigid and differential plasma crystal rotation induced by magnetic fields. *Phys. Rev. E* **61**, 1890 (2000).

[50] F. Cheung, A. Samarian, and B. James. The rotation of planar-2 to planar-12 dust clusters in an axial magnetic field. *New J. Phys.* **5**, 75.1 (2003).

[51] J. Carstensen, F. Greiner, L. J. Hou, H. Maurer, and A. Piel. Effect of neutral gas motion on the rotation of dust clusters in an axial magnetic field. *Phys. Plasmas*, **16** 013702 (2009).

[52] G. Praburam and J. Goree. Experimental observation of very low-frequency macroscopic modes in a dusty plasma. *Phys. Plasmas* **3** 1212 (1996).

[53] M. Mikikian and L. Boufendi. Experimental investigations of void dynamics in a dusty discharge. *Phys. Plasmas* **11** 3733 (2004).

[54] G. E. Morfill, H. M. Thomas, U. Konopka, H. Rothermel, M. Zuzic, A. Ivlev, and J. Goree. Condensed plasmas under microgravity. *Phys. Rev. Lett.* **83**, 1598 (1999).

[55] M. Mikikian, L. Couedel, M. Cavarroc, Y. Tessier, and L. Boufendi. Self-excited void instability in dusty plasmas: plasma and dust cloud dynamics during the heartbeat instability. *New J. Phys.* **9**, 268 (2007).

[56] H. Rothermel, T. Hagl, G. E. Morfill, M. H. Thoma, and H. M. Thomas. Gravity compensation in complex plasmas by application of a temperature gradient. *Phys. Rev. Lett.* **89**, 175001 (2002).

[57] J. Goree, G. E. Morfill, V. N. Tsytovich, and S. V. Vladimirov. Theory of dust voids in plasmas. *Phys. Rev. E* **59**, 7055 (1999).

[58] A. M. Lipaev, S. A. Khrapak, V. I. Molotkov, G. E. Morfill, V. E. Fortov, A. V. Ivlev, H. M. Thomas, A. G. Khrapak, V. N. Naumkin, A. I. Ivanov, S. E. Tretschev, and G. I. Padalka. Void closure in complex plasmas under microgravity conditions. *Phys. Rev. Lett.* **98**, 265006 (2007).

[59] V. Land and W. J. Goedheer. How to make large, void-free dust clusters in dusty plasma under micro-gravity. *New J. Phys.* **10**, 123028 (2008).

[60] N. N. Rao, P. K. Shukla, and M. Y. Yu. Dust-acoustic waves in dusty plasmas. *Planet. Space Sci.* **38**, 543 (1990).

[61] J. H. Chu, J. B. Du, and Lin I. Coulomb solids and low–frequency fluctations in rf dusty plasmas. *J. Phys. D: Appl. Phys.* **27**, 296 (1994).

[62] N. D'Angelo. Coulomb solids and low-frequency fluctuations in rf dusty plasmas. *J. Phys. D: Appl. Phys.* **28**, 1009 (1995).

[63] A. Barkan, R. L. Merlino, and N. D'Angelo. Laboratory observation of the dust-acoustic wave mode. *Phys. Plasmas* **2**, 3563 (1995).

[64] H. R. Prabhakara and V. L. Tanna. Trapping of dust and dust acoustic waves in laboratory plasmas. *Phys. Plasmas* **3**, 3176 (1996).

[65] E. Thomas, Jr. Measurements of spatially growing dust acoustic waves in a dc glow discharge plasma. *Phys. Plasmas* **13**, 042107 (2006).

[66] M. Rosenberg. A note on ion-dust streaming instability in a collisional dusty plasma. *J. Plasma Phys.* **67**, 235 (2002).

[67] R. L. Merlino. Dust-acoustic waves driven by an ion-dust streaming instability in laboratory discharge dusty plasma experiments. *Phys. Plasmas* **16**, 124501 (2009).

[68] P. K. Shukla and M. Rosenberg. Boundary effects on dust-ion-acoustic and dust-acoustic waves in collisional dusty plasmas. *Phys. Plasmas* **6**, 1038 (1999).

[69] V. Yaroshenko and G. E. Morfill. Parametric excitation of low frequency waves in complex (dusty) plasmas. *Phys. Plasmas* **9**, 4495 (2002).

[70] N. X. Wei and J. K. Xue. Bounded dust-acoustic waves in a cylindrically bounded collisional dusty plasma with dust charge variation. *Phys. Plasmas* **13**, 052101 (2006).

[71] V. V. Yaroshenko, H. M. Thomas, and G. E. Morfill. Dust density waves in a complex plasma layer. *Phys. Plasmas* **14**, 082104 (2007).

[72] M. Rosenberg and P. K. Shukla. A note on dust-acoustic instability in an inductive gas discharge plasma. *Plasma Phys. Control. Fusion* **45**, L31 (2003).

[73] M. Rosenberg, E. Thomas, Jr., and R. L. Merlino. A note on dust wave excitation in a plasma with warm dust: Comparison with experiment. *Phys. Plasmas* **15**, 073701 (2008).

[74] M. R. Jana, A. Sen, and P. K. Kaw. Collective effects due to charge-fluctuation dynamics in a dusty plasma. *Phys. Rev. E* **48**, 3930 (1993).

[75] F. Melandsø, T. Aslaksen, and O. Havnes. A new damping effect for the dust-acoustic wave. *Planet. Space Sci.* **41**, 321 (1993).

[76] A. V. Ivlev and G. Morfill. Acoustic modes in a collisional dusty plasma: Effect of the charge variation. *Phys. Plasmas* **7**, 1094 (2000).

[77] A. Zobnin, A. Usachev, O. Petrov, and V. Fortov. Dust-acoustic instability in an inductive gas-discharge plasma. *JETP* **95**, 429 (2002).

[78] C. Thompson, A. Barkan, N. D'Angelo, and R. L. Merlino. Dust acoustic waves in a direct current glow discharge. *Phys. Plasmas* **4**, 2331 (1997).

[79] T. Trottenberg, D. Block, and A. Piel. Dust confinement and dust-acoustic waves in weakly magnetized anodic plasmas. *Phys. Plasmas* **13**, 042105 (2006).

[80] E. Thomas, Jr., R. Fisher, and R. L. Merlino. Observations of dust acoustic waves driven at high frequencies: Finite dust temperature effects and wave interference. *Phys. Plasmas* **14**, 123701 (2007).

[81] J. D. Williams, E. Thomas, Jr., and L. Marcus. Observations of vertically propagating driven dust acoustic waves: Finite temperature effects. *Phys. Plasmas* **15**, 043704 (2008).

[82] J. D. Williams and J. Duff. Observation of the coupling of the driven dust acoustic wave. *Phys. Plasmas* **17**, 033702 (2010).

[83] Arkady Pikovsky, Michael Rosenblum, and Jürgen Kurths. *Synchronization.* Cambridge University Press, 2001.

[84] A. Balanov, N. Janson, D. Postnov, and O. Sosnovtseva. *Synchronization: From Simple to Complex.* Springer, 2009.

[85] Heinz Georg Schuster. Control of chaos in plasmas. In H. G. Schuster, editor, *Handbook of Chaos Control.* Wiley-CHV, 1999.

[86] E. Atlee Jackson. *Perspectives of nonlinear dynamics.* Cambridge University Press, 1989.

[87] Chihiro Hayashi. *Nonlinear oscillations in physical systems.* Princeton Univ. Press, 1985.

[88] I. Pilch, T. Reichstein, and A. Piel. Synchronization of dust density waves in anodic plasmas. *Phys. Plasmas* **16**, 123709 (2009). (see Appendix B.3).

[89] M. Schwabe, S. K. Zhdanov, H. M. Thomas, A. V. Ivlev, M. Rubin-Zuzic, G. E. Morfill, V. I. Molotkov, A. M. Lipaev, V. E. Fortov, and T. Reiter. Nonlinear waves externally excited in a complex plasma under microgravity conditions. *New J. Phys.* **10**, 033037 (2008).

[90] Francis F. Chen. *Introduction to plasma physics and controlled fusion*. Plenum Press, New York, 1990.

[91] I. H. Hutchinson. *Principles of plasma diagnostics*. Cambridge Univ. Press, Cambridge, 2002.

[92] P. K. Shukla and M. M. Mamun. *Introduction to dusty plasma physics*. IOP, 2002.

[93] M. A. Liebermann and A. J. Lichtenberg. *Principles of plasma discharges and material processing*. John Wiley and Sons Inc., New York, 1994.

[94] A. Piel and A. Melzer. Dynamical processes in complex plasmas. *Plasma Phys. Control. Fusion* **44**, R1 (2002).

[95] V. E. Fortov, A. V. Ivlev, S. A. Khrapak, A. G. Khrapak, and G. E. Morfill. Complex (dusty) plasmas: Current status , open issues, perspectives. *Physics Reports* **421**, 1 (2005).

[96] E. Thomas, Jr. Dust clouds in dc-generated dusty plasmas: Transport, waves, and three-dimensional effects. *Contrib. Plasma Phys.* **49**, 316 (2009).

[97] S. A. Khrapak, A.V. Ivlev, S. K. Zhdanov, and G. E. Morfill. Hybrid approach to the ion drag force. *Phys. Plasmas* **12**, 042308 (2005).

[98] Thomas Trottenberg. *Diagnostik mit Resonanzkegeln, Partikeleinschluss und staubakustische Wellen in magnetisierten komplexen Plasmen*. PhD thesis, Christian-Albrechts-Universität zu Kiel, April 2006.

[99] E. C. Whipple. Potentials of surfaces in space. *Rep. Prog. Phys.* **44**, 1197 (1981).

[100] H. M. Mott-Smith and I. Langmuir. The theory of collectors in gaseous discharges. *Phys. Rev.* **28**, 727 (1926).

[101] P. S. Epstein. On the resistance experienced by spheres in their motion through gases. *Phys. Rev.* **23**, 710 (1924).

[102] M. S. Barnes, J. H. Keller, J. C. Forster, J. A. O'Neill, and D. K. Coultas. Transport of dust particles in glow–discharge plasmas. *Phys. Rev. Lett.* **68**, 313 (1992).

[103] M. D. Kilgore, J. E. Daugherty, R. K. Porteous, and D. B. Graves. Ion drag on an isolated particulate in a low pressure discharge. *J. Appl. Phys.* **73**, 7195 (1993).

[104] S. A. Khrapak, A. V. Ivlev, G. E. Morfill, and H. M. Thomas. Ion drag force in complex plasmas. *Phys. Rev. E* **66**, 046414 (2002).

[105] I. H. Hutchinson. Collisionless ion drag force on a spherical grain. *Plasma Phys. Control. Fusion* **48**, 185 (2006).

[106] V. R. Ikkurthi, K. Matyash, A. Melzer, and R. Schneider. Computation of ion drag force on a static spherical dust grain immersed in rf discharges. *Phys. Plasmas* **16**, 043703 (2009).

[107] C. Zafiu, A. Melzer, and A. Piel. Ion drag and thermophoretic forces acting on free falling charged particles in an rf-driven complex plasma. *Phys. Plasmas* **9**, 4794 (2002).

[108] C. Zafiu, A. Melzer, and A. Piel. Measurement of the ion drag force on falling dust particles and its relation to the void formation in complex (dusty) plasmas. *Phys. Plasmas* **10**, 1278 (2003).

[109] M. Hirt, D. Block, and A. Piel. Measurement of the ion drag force on free falling microspheres in a plasma. *Phys. Plasmas* **11**, 5690 (2004).

[110] V. Nosenko, R. Fisher, R. Merlino, S. Khrapak, G. Morfill, and K. Avinash. Measurement of the ion drag force in a collisionless plasma with strong ion-grain coupling. *Phys. Plasmas* **14**, 103702 (2007).

[111] V. Schneider, T. Trottenberg, I. Teliban, and H. Kersten. An experiment for the investigation of forces on microparticles in ion beams. *Rev. Sci. Instrum.* **81**, 013503 (2010).

[112] A. V. Ivlev, S. K. Zhdanov, S. A. Khrapak, and G. E. Morfill. Kinetic approach for the ion drag force in a collisionial plasma. *Phys. Rev. E* **71**, 016405 (2005).

[113] S. A. Khrapak, S. K. Zhdanov, A. V. Ivlev, and G. E. Morfill. Drag force on an absorbing body in highly collisional plasmas. *J. Appl. Phys.* **101**, 033307 (2007).

[114] M. Chaudhuri, S. A. Khrapak, and G. E. Morfill. Ion drag force on a small grain in highly collisional weakly anisotropic plasma: Effect of plasma production and loss mechanisms. *Phys. Plasmas* **15**, 053703 (2008).

[115] L. Patacchini and I. H. Hutchinson. On negative ion-drag force for dust in collisional plasmas. *Multifacets Of Dusty Plasma* **1041**, 297 (2008).

[116] J. E. Daugherty and B. D. Graves. Derivation and experimental verification of a particulate transport model for a glow discharge. *J. Appl. Phys.* **78**, 2279 (1995).

[117] S. Chandrasekhar. Dynamical friction I. general considerations: The coefficient of dynamical friction. *Ap. J.* **97**, 255 (1943).

[118] L. S. Frost. Effect of variable ionic mobility on ambipolar diffusion. *Phys. Rev.* **105**, 354 (1957).

[119] S. Robertson and Z. Sternovsky. Monte carlo model of ion mobility and diffusion for low and high electric fields. *Phys. Rev. E* **67**, 046405 (2003).

[120] microParticles GmbH. Volmerstr. 9A, D-12489 Berlin, Germany, http://www.microparticles.de/.

[121] Robert Alexander Große-Ahlert. Struktur und Bewegungsvorgänge in magnetisierten staubigen Plasmen. Diplomarbeit, Christian-Albrechts-Universität zu Kiel, October 2009.

[122] L. Malter, E. O. Johnson, and W. M. Webster. Studies of externally heated hot cathode arcs: Part I. - modes of the discharge. *RCA Rev.* **12**, 415 (1951).

[123] W. M. Webster, E. O. Johnson, and L. Webster. Studies of externally heated hot cathode arcs: Part II - the anode-glow mode. *RCA Rev.* **13**, 163 (1952).

[124] E. O. Johnson and W. M. Webster. Studies of externally heated hot cathode arcs: Part III - plasma density distribution on the anode-glow mode. *RCA Rev.* **16**, 82 (1955).

[125] E. O. Johnson. Studies of externally heated hot cathode arcs: Part IV - the low-voltage form of the ball-of-fire mode (the low-voltage arc). *RCA Rev.* **16**, 498 (1955).

[126] B. Song, N. D'Angelo, and R. L. Merlino. On anode spots, double layers and plasma contactors. *J. Phys. D: Appl. Phys.* **24**, 1789 (1991).

[127] T. An, R. L. Merlino, and N. D'Angelo. Cylindrical anode double layers ('firerods') produced in a uniform magnetic field. *J. Phys. D: Appl. Phys.* **27**, 1906 (1994).

[128] I. Langmuir. The interaction of electron and positive ion space charges in cathode sheaths. *Phys. Rev.* **33**, 954 (1929).

[129] C. Charles. A review of recent laboratory double layer experiments. *Plasma Sources Sci. Technol.* **16**, R1 (2007).

[130] A. Barkan and R. L. Merlino. Confinement of dust particles in a double layer. *Phys. Plasmas* **2**, 3261 (1995).

[131] Torben Reichstein. Sondendiagnostik zur Analyse von Einschluss und Dynamik von Staub in magnetisierten Plasmen. Diplomarbeit, Christian-Albrechts-Universität zu Kiel, October 2008.

[132] P. Bergé, Y. Pomeau, and C. Vidal. *Order within Chaos.* John Wiley & Sons, New York, 1984.

[133] V. I. Arnold. *Mathmatical Methods of Classical Mechaniscs.* Springer-Verlag New York Inc., 2nd edition, 1989.

[134] B. van der Pol. Forced oscillations in a circuit with non-linear resistance. *Phil. Mag. S. 7* **3**, 65 (1927).

[135] V. I. Arnold. *Geometrical Methods in the Theory of Ordinary Differential Equations.* Springer-Verlag New York Inc., 1983.

[136] T. Klinger. *Experimentelle Untersuchung der nichtlinearen Dynamik einer thermionischen Entladung.* PhD thesis, Christian-Albrechts-Universität zu Kiel, 1994.

[137] H. Lashinsky. Periodic pulling and the transition to turbulence in a system with discrete modes. In J. Fox, editor, *Symposium on Turbulence of Fluids and Plasmas*, pages 29–46. Polytechnic Institute of Brooklyn, Polytechnic Press, Brooklyn, New York, 1968.

[138] R.H. Abrams, E.J. Yadlowsky, and H. Lashinsky. Periodic pulling and turbulence in a bounded plasma. *Phys. Rev. Lett.* **22**, 275 (1969).

[139] M.E. Koepke, T. Klinger, F. Seddighi, and A. Piel. Periodic nonlinear wave-wave interaction in a plasma discharge with no external oscillatory driving force. *Phys. Plasma* **3**, 4421 (1996).

[140] D. Block, A. Piel, Ch. Schröder, and T. Klinger. Synchronization of drift waves. *Phys. Rev. E* **63**, 056401 (2001).

[141] C. Brandt, O. Grulke, and T. Klinger. Nonlinear interaction of drift waves with driven plasma currents. *Phys. Plasmas* **17**, 032304 (2010).

[142] H. Schollmeyer, A. Melzer, A. Homann, and A. Piel. Dust-dust and dust-plasma interactions of monolayer plasma crystals. *Phys. Plasmas* **6**, 2693 (1999).

[143] A.V. Ivlev, R. Sütterlin, V. Steinberg, and G.E. Morfill. Nonlinear vertical oscillations of a particle in a sheath of a rf discharge. *Phys. Rev. Lett.* **85**, 4060 (2000).

[144] C. Zafiu, A. Melzer, and A. Piel. Nonlinear resonances of particles in a dusty plasma sheath. *Phys. Rev. E* **63**, 066403 (2001).

[145] S. Khrapak, D. Samsonov, G. Morfill, H. Thomas, V. Yaroshenko, H. Rothermel, V. Fortov, A. Nefedov, V. Molotkov, O. Petrov, A. Lipaev, A. Ivanov, and Y. Baturin. Compressional waves in complex (dusty) plasmas under microgravity conditions. *Phys. Plasmas* **10**, 1 (2003).

[146] V. V. Yaroshenko, B. M. Annaratone, S. A. Khrapak, H. M. Thomas, G. E. Morfill, V. E. Fortov, A. M. Lipaev, V . I. Molotkov, O. F. Petrov, A. I. Ivanov, and M. V. Turin. Electrostatic modes in collisional complex plasmas under microgravity conditions. *Phys. Rev. E* **69**, 066401 (2004).

[147] A. Melzer, V.A. Schweigert, and A. Piel. Transition from attractive to repulsive forces between dust molecules in a plasma sheath. *Phys. Rev. Lett.* **83**, 3194 (1999).

[148] V. E. Fortov, O. F. Petrov, V. I. Molotkov, M. Y. Poustylnik, V. M. Torchinsky, A. G. Khrapak, and A. V. Chernyshev. Large-amplitude dust waves excited by the gas-dynamic impact in a dc glow discharge plasma. *Phys. Rev. E* **69**, 016402 (2004).

[149] A. Homann, A. Melzer, and A. Piel. Measuring the charge on single particles by laser-excited resonances in plasma crystals. *Phys. Rev. E* **59**, 3835 (1999).

[150] V. E. Fortov, A. G. Khrapak, S. A. Khrapak, V. I. Molotkov, A. P. Nefedov, O. F. Petrov, and V. M. Torchinsky. Mechanism of dust-acoustic instability in a direct current glow discharge plasma. *Phys. Plasmas* **7**, 1374 (2000).

[151] A. Homann, A. Melzer, S. Peters, R. Madani, and A. Piel. Determination of the dust screening length by laser-excited lattice waves. *Phys. Rev. E* **56**, 7138 (1997).

[152] A. Piel, V. Nosenko, and J. Goree. Laser-excited shear waves in solid and liquid two-dimensional dusty plasmas. *Phys. Plasmas* **13**, 042104 (2006).

[153] S. Nunomura, J. Goree, S. Hu, X. Wang, and A. Bhattacharjee. Dispersion relations of longitudinal and transverse waves in two-dimensional screened Coulomb crystals. *Phys. Rev. E* **65**, 066402 (2002).

[154] V. Nosenko, J. Goree, Z.W. Ma, and A. Piel. Observation of shear-wave mach cones in a 2d dusty-plasma crystal. *Phys. Rev. Lett.* **88**, 135001 (2002).

[155] V. Nosenko, J. Goree, Z. W. Ma, D. H. E. Dubin, and A. Piel. Compressional and shear wakes in a two-dimensional dusty plasma crystal. *Phys. Rev. E* **68**, 056409 (2003).

[156] V. E. Fortov, A. D. Usachev, A. V. Zobnin, V. I. Molotkov, and O. F. Petrov. Dust-acoustic wave instability at the diffuse edge of radio frequency inductive low-pressure gas discharge plasma. *Phys. Plasmas* **10**, 1199 (2003).

[157] M. Schwabe, M. Rubin-Zuzic, S. Zhdanov, H. M. Thomas, and G. E. Morfill. Highly resolved self-excited density waves in a complex plasma. *Phys. Rev. Lett.* **99**, 095002 (2007).

[158] C.-T. Liao, L.-W. Teng, C.-Y. Tsai, C.-W. Io, and Lin I. Lagrangian-eulerian micromotion and wave heating in nonlinear self-excited dust-acoustic waves. *Phys. Rev. Lett.* **100**, 185004 (2008).

[159] L. J. Hou and A. Piel. Trapped particles by large-amplitude waves in 2d yukawa liquids. *Multifacets Of Dusty Plasma* **1041**, 227 (2008).

[160] E. Thomas, Jr. and M. Watson. First experiments in the dusty plasma experiment device. *Phys. Plasmas* **6**, 4111 (1999).

[161] E. Thomas, Jr. Direct measurement of two-dimensional velocity profiles in direct current glow discharge dusty plasmas. *Phys. Plasmas* **6**, 2672 (1999).

[162] J. D. Williams and E. Thomas, Jr. Initial measurement of the kinetic dust temperature of a weakly coupled dusty plasma. *Phys. Plasmas* **13**, 063509 (2006).

[163] K. O. Menzel, O. Arp, D. Caliebe, and A. Piel. The structure of self-excited dust-density waves under microgravity. *IEEE Trans. Plasma Sci.* **38**, 838 (2010).

[164] E. Thomas, Jr. and R. L. Merlino. Dust particle motion in the vicinity of dust acoustic waves. *IEEE Trans. Plasma Sci.* **29**, 152 (2001).

[165] M. Bonitz, K. Balzer, and R. van Leeuwen. Invariance of the Kohn center-of-mass mode in a conserving theory. *Phys. Rev. B* **76**, 045341 (2007).

[166] V. Nosenko, S. K. Zhdanov, S.-H. Kim, J. Heinrich, R. L. Merlino, and G. E. Morfill. Measurements of the power spectrum and dispersion relation of self-excited dust acoustic waves. *Europhys. Lett.* **88**, 65001 (2009).

[167] W. E. Amatucci, D. N. Walker, G. Gatling, and E. E. Scime. Direct observation of microparticle gyromotion in a magnetized direct current glow discharge dusty plasma. *Phys. Plasmas* **11**, 2097 (2004).

[168] N. Sato, G. Uchida, T. Kaneko, S. Shimizu, and S. Iizuka. Dynamics of fine particles in magnetized plasmas. *Phys. Plasmas* **8**, 1786 (2001).

[169] V. Y. Karasev, E. S. Dzlieva, A. Y. Ivanov, and A. I. Eikhvald. Rotational motion of dusty structures in glow discharge in longitudinal magnetic field. *Phys. Rev. E* **74**, 066403 (2006).

[170] V. Y. Karasev, E. S. Dzlieva, A. I. Eikhval'd, M. A. Ermolenko, M. S. Golubev, and A. Y. Ivanov. Single dust-particle rotation in glow-discharge plasma. *Phys. Rev. E* **79**, 026406 (2009).

[171] K. Avinash. "Voids" and phase separation in complex (dusty) plasmas. *Phys. Plasmas* **8**, 2601 (2001).

[172] K. Avinash, A. Bhattacharjee, and S. Hu. Nonlinear theory of void formation in colloidal plasmas. *Phys. Rev. Lett.* **90**, 075001 (2003).

[173] G. Gozadinos, A. V. Ivlev, and J. P. Boeuf. A fluid model for colloidal plasmas under microgravity conditions. *New J. Phys.* **5**, 32 (2003).

[174] M. R. Akdim and W. J. Goedheer. Modelling of voids in colloidal plasmas. *Phys. Rev. E* **65**, 015401 (2002).

[175] M. R. Akdim and W. J. Goedheer. Modeling the effect of dust on the plasma parameters in a dusty argon discharge under microgravity. *Phys. Rev. E* **67**, 056405 (2003).

[176] V. Land and W. J. Goedheer. Effect of large-angle scattering, ion flow speed and ion-neutral collisions on dust transport under microgravity conditions. *New J. Phys.* **8**, 8 (2006).

[177] C. O. Thompson, N. D'Angelo, and R. L. Merlino. The interaction of stationary and moving objects with dusty plasmas. *Phys. Plasmas* **6**, 1421 (1999).

[178] M. Klindworth, A. Piel, A. Melzer, U. Konopka, H. Rothermel, K. Tarantik, and G.E. Morfill. Dust free regions around langmuir probes in complex plasmas under microgravity. *Phys. Rev. Lett.* **93**, 195002 (2004).

[179] E. Thomas, Jr., K. Avinash, and R. L. Merlino. Probe induced voids in a dusty plasma. *Phys. Plasmas* **11**, 1770 (2004).

[180] T. Trottenberg. Private communication (2010). The first observation of a torus-shaped dust cloud was made in October 2004.

[181] I. Pilch, T. Trottenberg, A. Piel, and M. E. Koepke. Dynamics of small dust clouds trapped in a magnetized anodic plasma. *Phys. Plasmas* **14**, 123704 (2007). (see Appendix B.1).

[182] J. K. Sveen. An introduction to MATPIV V.1.6.1. Eprint no. 2, **ISSN** 0809-4403, Dept. of Mathematics, University of Oslo, 2004. http://www.math.uio.no/~jks/matpiv.

[183] T. Reichstein, I. Pilch, R. Grosse-Ahlert, and A. Piel. Toroidal dust clouds and voids in a magnetized anodic plasma. *IEEE Trans. Plasma Sci.* **38**, 814 (2010).

[184] D. Samsonov and J. Goree. Instabilities in a dusty plasma with ion drag and ionization. *Phys. Rev. E* **59**, 1047 (1999).

[185] M. Rosenberg. Ion-dust streaming instability in processing plasmas. *J. Vac. Sci. Technol. A* **14**, 631 (1996).

[186] A. Piel, O. Arp, M. Klindworth, and A. Melzer. Obliquely propagating dust-density waves. *Phys. Rev. E* **77**, 026407 (2008).

[187] Ronald C. Davidson. *Methods in nonlinear plasma theory.* ACADEMIC PRESS, INC., New York, 1972.

B Reprints of Journal Papers

B.1

DYNAMICS OF SMALL DUST CLOUDS TRAPPED IN A MAGNETIZED ANODIC PLASMA

I. Pilch, T. Trottenberg, A. Piel, and M. E. Koepke

Reprinted with permission from
I. Pilch, T. Trottenberg, A. Piel, and M. E. Koepke,
Physics of Plasmas, Vol. 14, Page 123704 (2007).

Dynamics of small dust clouds trapped in a magnetized anodic plasma

Iris Pilch,[a] Alexander Piel, and Thomas Trottenberg
Institut für Experimentelle und Angewandte Physik, Christian-Albrechts-Universität, D-24098 Kiel, Germany

Mark E. Koepke
Department of Physics, West Virginia University, Morgantown, West Virginia 26505-6315, USA

(Received 2 October 2007; accepted 8 November 2007; published online 10 December 2007)

Small dust clouds, which are confined in an anodic plasma, are studied with respect to their structure and their response to modulation of the anode bias. The dust cloud is displaced from the center of the discharge by a process similar to the void mechanism in radio-frequency discharges under microgravity. The top layers of the dust cloud are in a crystalline state and the cloud performs a slow rotation about the magnetic field direction. For modulation frequencies below 15 Hz, a sloshing and stretching motion in the confining potential well is found. Spontaneously excited dust density waves are observed when the dust cloud exceeds a minimum size. The waves are characterized by sickle-shaped wave fronts. No standing waves were found. The wave dispersion shows an influence of the boundedness of the system in terms of a frequency cutoff. © *2007 American Institute of Physics*. [DOI: 10.1063/1.2819315]

I. INTRODUCTION

Dust acoustic waves[1] are very-low-frequency density waves in a dusty plasma which involve the inertia of the dust particles and their shielded interaction force. The first observation of a dust acoustic-like wave was made by Thompson *et al.*[2] as a self-excited mode in a dust cloud trapped in an anodic plasma. The wave was excited by the ion current through the dust cloud and the waves propagated in the direction of the ion flow. Thompson *et al.* measured the dispersion relation of the wave by modulating the anode bias and found an almost acoustic dispersion of the density wave, as expected from the dust acoustic wave model.[1] Other authors studied a dust-acoustic instability in an inductive plasma,[3] the quenching of the unstable dust acoustic wave in a dc glow discharge by collisions,[4,5] or the spatial wave growth by particle-image-velocimetry.[6]

More recent investigations of this phenomenon by Trottenberg *et al.*[7] were focused on the confinement of the dust in the anodic plasma and on a refined analysis of the wave dispersion by comparing with a kinetic model.[8] The classical dust acoustic wave assumes an environment of thermal electrons and ions. Since the self-excited wave in experiments is driven by an ion drift, we prefer to call the waves in this more general situation dust density waves. Very recently, it was found that, in unmagnetized plasmas, dust density waves tend to propagate at an oblique angle to the ion drift when the ion drift speed exceeds the ion thermal speed.[9]

A central question in studying dust density waves is the influence of the system size on the wave propagation. Up to now, the analysis of experimental data was based on the comparison with theories that assume plane waves in an infinite homogeneous medium.[2,4,7] The role of boundaries, that act like a waveguide, on the dispersion of the wave were theoretically discussed with respect to a frequency cutoff.[10–12]

Small confined dust clouds that are embedded in a magnetized plasma and interact with an ion flow are interesting. They have internal structure that, in some ways, is similar and, in other ways, different from Yukawa balls.[13,14]

In the present paper we describe a detailed study of the dynamical behavior of such small dust clouds with respect to their structure, confinement, and internal density waves. The paper is organized as follows. The experimental arrangement is described in Sec. II and the shape and structure of the dust cloud is presented in Sec. III. The dynamics is studied at low modulation frequencies in terms of a "sloshing" motion in Sec. IV and at higher modulation frequencies as wave motion in Sec. V. The different observations are separately checked for consistency in Sec. VII.

II. EXPERIMENTAL SETUP

Figure 1(a) shows a longitudinal section of the plasma chamber. The cylindrical vacuum vessel has 104 cm length and 27 cm inner diameter. Ten magnetic field coils generate a homogenous magnetic field of typically 20 mT in the direction shown. A radio-frequency discharge at $f=27.12$ MHz is generated between a plane powered electrode (E) of 10 cm diameter and a plane grounded grid (G) at a distance of 5 cm, which are positioned at the right end of the device. This primary plasma source is operated at low power (1 W). The plasma expands through the grid and fills a column of 10 cm diameter which extends over the entire length of the vessel. Plasma density or plasma potential can be measured as a function of radius and axial position with a cylindrical Langmuir probe and an emissive probe, respectively, each supported by a shaft having a dog-leg geometry (P).

Our experiments are performed in argon gas at $p=3$ Pa. The plasma has a typical density of $n_e=10^{15}$ m^{-3}, an electron

[a]Electronic mail: pilch@physik.uni-kiel.de.

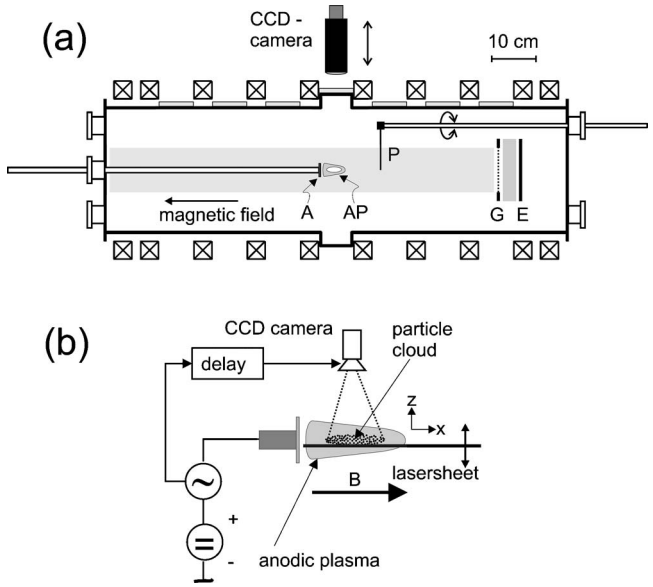

FIG. 1. (a) Cross section of the MATILDA II plasma device. (b) A dust cloud is trapped in the anodic plasma and observed with a combination of horizontal laser fan and camera. For stroboscopic recordings the camera shutter can be triggered from the signal generator.

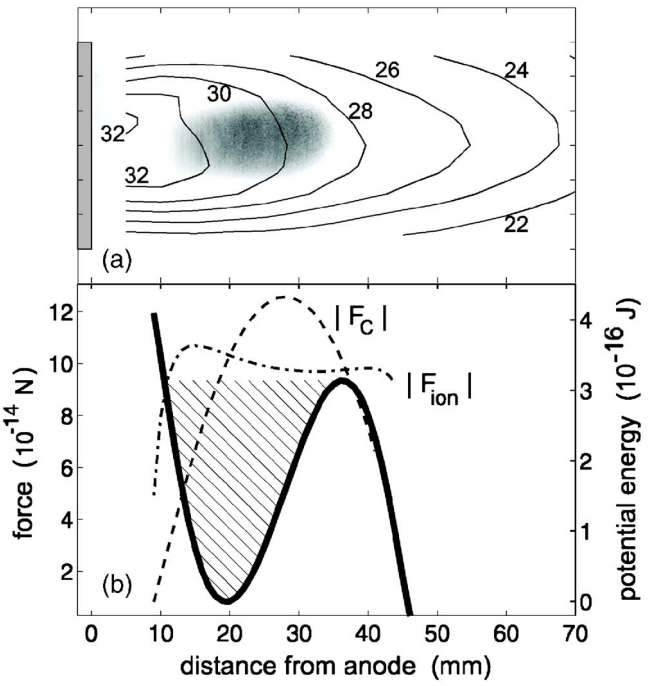

FIG. 2. (Color online) Axial confinement of a dust cloud in the anodic plasma (Ref. 7). (a) Contours of electric potential and top view of the dust cloud. (b) An effective potential well is formed by the electric force F_C and the ion drag force F_{ion}.

temperature of $T_e=3$ eV, and an ion temperature of $T_i=0.1$ eV.[7] We use spherical monodisperse dust particles (melamine formaldehyde) of 0.97 ± 0.05 μm diameter.

A secondary plasma is generated by biasing to high voltage $60\ \text{V} \leqslant U_a \leqslant 75\ \text{V}$ a small disk electrode (A) of 3 cm diameter, which is inserted axially. This phenomenon is known from low-pressure arcs[15] and was used as a plasma contactor.[16] At high values of currents drawn by the disk, a "fireball" is formed which takes the shape of a cylinder, i.e., a "firerod," in the presence of a magnetic field.[17] In the following we refer to the disk as "anode" and call this secondary plasma "anodic plasma." The formation of such an anodic plasma is also found in other experiments on dust acoustic waves with confined dust.[2,18,19]

Dust lying on a small tray below is spontaneously repelled from the tray and attracted into the anodic plasma above a certain anode bias voltage, here $U_a \approx 120$ V. The confinement of dust in front of the anode disk was studied in detail by Trottenberg *et al.*[7] The potential contours in Fig. 2(a), which is reproduced here for further reference, were obtained from measurements of the two-dimensional potential structure with an emissive probe. The dust is trapped in an effective potential well [see Fig. 2(b)], that is formed by an inhomogeneous axial electric field and the ion drag force. Radial confinement is made possible by a moderate magnetic field, which is responsible for an enhancement of the radial electric field compared to the axial electric field, which we understand to be the influence of the different Hall parameters of electrons and ions.

Coherent waves can be generated by Thompson's technique[2] of adding a sinusoidal modulation voltage to the anode bias. We use an ac voltage of $U_{\text{mod}}=10\ V_{pp}$ superimposed on the dc voltage of $60\ \text{V} \leqslant U_a \leqslant 75$ V. The observation geometry and image acquisition method for the structure and dynamics of small dust clouds are sketched in Fig. 1(b). The dust cloud is illuminated by a laser light sheet ($\lambda=532$ nm, 200 mW) and the scattered light is recorded by a camera which is placed above the experiment. The camera has a CCD sensor with 480×640 pixels and a frame rate of 150 fps at maximum resolution. Laser light sheet and camera with a macro lens are mounted on a translation stage and can be vertically positioned to image any horizontal plane of the plasma. In this way, the dust cloud can be scanned volumetrically in a series of horizontal slices.

Phase synchronous recording of the wave can be achieved by triggering the camera shutter from the square-wave output of the signal generator that delivers the modulation voltage. The shutter time of the camera is small (2 ms) with respect to the period of the modulation voltage. This kind of recording gives a stroboscopic image of the wave, which can be either used for averaging the image or for detecting any jitter about the average image. The phase between the trigger pulse and the camera shutter can be varied by a pulse delay unit. In a second mode of operation, the camera is triggered from a signal generator at $f=8\times f_{\text{mod}}$ that is phase-locked with the modulation generator. Such a high frame rate can be achieved by selecting a smaller region of interest.

In the following, we use a coordinate system in which the x-axis is aligned with the magnetic field direction, the y-axis is in the horizontal plane, and the z-axis defines the vertical direction. We will use the terminology of a "small" dust cloud when the dimensions are smaller than a typical wavelength of the dust density wave, $d<\lambda$. The cloud is called "medium" size for $2\lambda<d<3\lambda$ and "large" for $d\gg\lambda$.

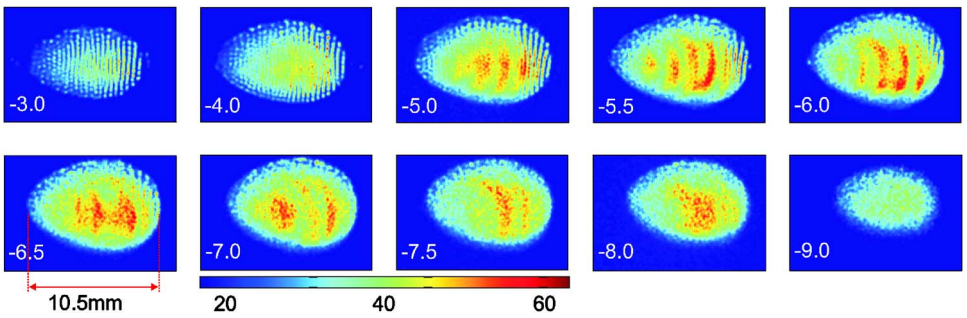

FIG. 3. (Color online) A series of horizontal sections of the dust cloud obtained by stroboscopic recording and averaging of 100 subsequent frames. The numbers refer to the z-position.

III. THE STRUCTURE OF THE DUST CLOUD

Small and medium sized dust clouds in the anodic plasma take the shape of a prolate ellipsoid, which are aligned with the magnetic field direction. A typical dust cloud of medium size is shown in Fig. 3 as a series of horizontal sections. Each image is generated with the stroboscopic technique and represents the average of 100 time-adjacent frames. The dust cloud has a length of 10.5 mm and a diameter of 7.3 mm. The numbers in each image indicate the vertical position of the section in millimeters with respect to the center of the anode disk. Obviously the dust cloud is horizontally centered with the anodic plasma but we note that it is shifted vertically (by 6 mm) to a lower position. The mean interparticle distance is $b=440\ \mu$m, which corresponds to a dust density $n_d \approx b^{-3}=1.2\times10^{10}\ \mathrm{m}^{-3}$. The total number of particles in the dust cloud is $N_d \approx 3.8\times10^4$.

Inspecting the images in Fig. 3, two features become immediately evident. First, there is a pronounced structure of parallel stripes in the sections between −3.0 mm and −6.0 mm, which become increasingly blurred at lower positions. The stripes have a distance of 450 μm, which corresponds to the typical interparticle distance. Second, there are curved wave fronts of a dust density wave visible in the sections between −5.0 mm and −8.0 mm. The wave pattern appears as alternating light and dark sickle-shaped wave fronts.

The stripes are oriented exactly perpendicular to the magnetic field. We interpret the equal spacing and alignment of the stripes as a crystalline ordering in the upper part of the dust cloud. The lower half of the cloud is in a liquid phase. The cloud performs a slow rotation about the magnetic field direction due to the azimuthal component of the ion motion, which exerts a torque on the dust cloud by ion drag. In view of the wave activity, we cannot perform a reliable three-dimensional structural analysis by means of scanning video microscopy, as it was done for Yukawa balls.[13]

However, we can analyze the intrinsic orientational order in each individual frame of the stroboscopic movie. A single frame of the movie corresponding to position $z=-3$ mm is shown in Fig. 4(a). In particular in the right half of the cloud, an intrinsic order can be seen that prefers alignment in a direction perpendicular to the magnetic field. This ordering can be quantified by a histogram of the bond-orientational order. For this purpose we define the bond angle of nearest neighbors (nn) $\theta_{ij}=\arctan[(x_i-x_j)/(y_i-y_j)]$ and a histogram function,

$$h(\theta)=\sum_{i=1}^{N}\sum_{j\in\{\mathrm{nn}\}}\delta(\theta-\theta_{ij}). \tag{1}$$

We define a nearest neighbor as particle having a distance of less than 1.3 b, when b is the mean interparticle distance. At last, the histogram is averaged over 1024 frames and normalized to unity. The polar plot of this histogram in Fig. 4(b) shows a sharp peak in the $\pm y$-direction which indicates the alignment perpendicular to the magnetic field direction. The

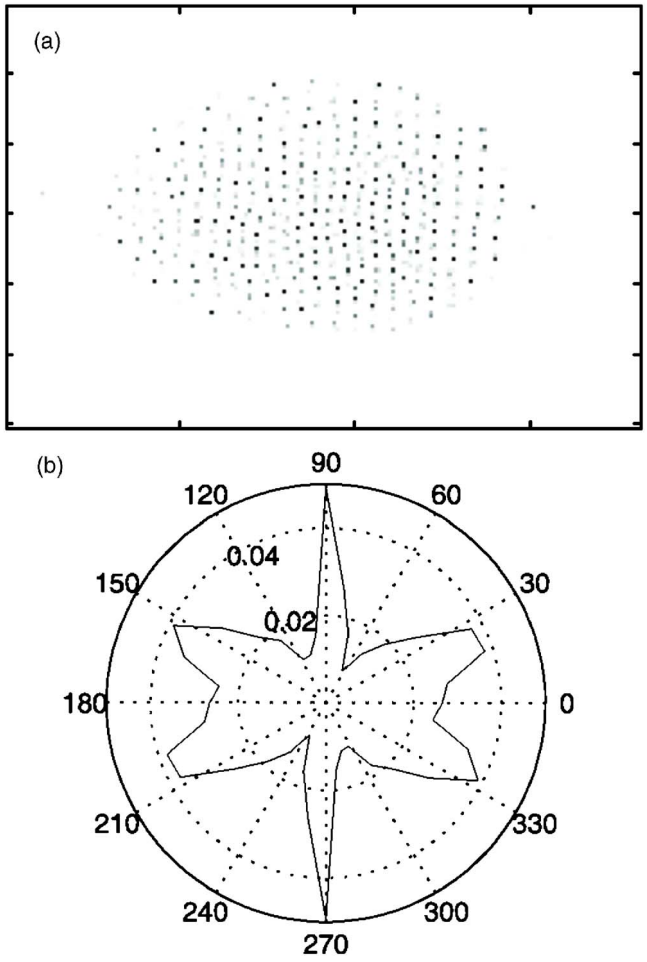

FIG. 4. (Color online) (a) The arrangement of the dust particles in a single frame (corresponding to $z=-3.0$ mm in Fig. 3) hints at a preference to form aligned ordering perpendicular to the magnetic field. (b) Polar plot of the bond-order histogram observed in individual frames, averaged over 100 frames. The sharp peaks at 90°/270° confirm the alignment. The pattern can be interpreted as the superposition of a sixfold and fourfold symmetry.

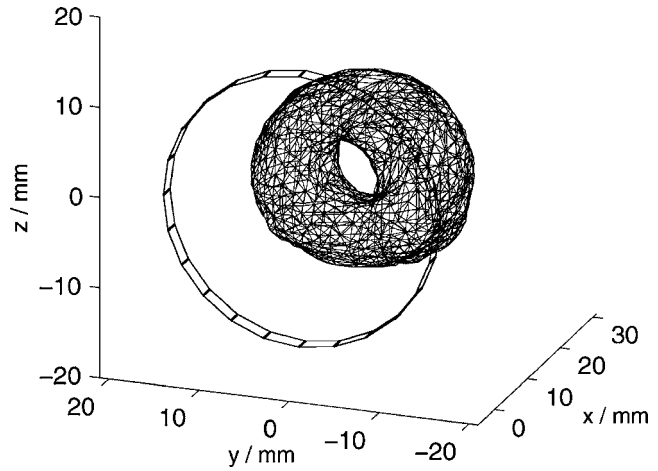

FIG. 5. Equidensity contour of the scattered light from a dust cloud of submicron particles. The central hole of this toroidal shape is interpreted as a void region, in which the ion drag force exceeds the radial electric field force.

polar plot has six pronounced lobes. This indicates a preference for a sixfold symmetry. However, the maxima of the broader lobes form angles of more than 60° with respect to the aligned peaks and the minima between the broader peaks are less deep than the minima adjacent to the sharp peaks. This finding is a hint at the admixture of a fourfold symmetry.

Careful inspection of the dust density distribution in a horizontal section of the cloud (see, e.g., Fig. 3 at $z=-4$ mm) shows a dark gap close to the boundary of the dust cloud which contains no particles. Such a gap was also observed in experiments with large Yukawa balls,[13] which tend to be in a liquid state, and was interpreted as an induced radial order at the surface caused by the strong force gradient of the confinement.

At higher magnetic field (50 mT) and gas pressure (5 Pa), large dust clouds can attain the topology of a torus with a central hole. The shape of the cloud is reconstructed here by measuring the intensity distribution of scattered light in a sequence of vertically displaced slices and calculating three-dimensional contour surfaces. Such an equidensity contour is shown in Fig. 5. This torus is slowly rotating in the $\vec{j}_i \times \vec{B}$ direction. Torus formation requires a sufficient amount of dust in the system and an azimuthal component of the ion drag force that is able to lift the dust against gravity.

IV. SLOSHING MOTION

The dynamical response of a dust cloud of small or medium size to a modulation of the anode bias depends on the applied frequency. For modulation frequencies 1 Hz$\leqslant f_{\mathrm{mod}} \leqslant$15 Hz, these clouds perform a periodic axial motion, which we call "sloshing." For medium-sized clouds, self-excited internal density waves are found, which can be synchronized by the external modulation force at higher frequencies of 20 Hz$\leqslant f_{\mathrm{mod}} \leqslant$40 Hz.

An example for the response of a small dust cloud at different phases during modulation at $f_{\mathrm{mod}}=4$ Hz is shown in Fig. 6. The dc bias was $U_a=70$ V and the modulation voltage

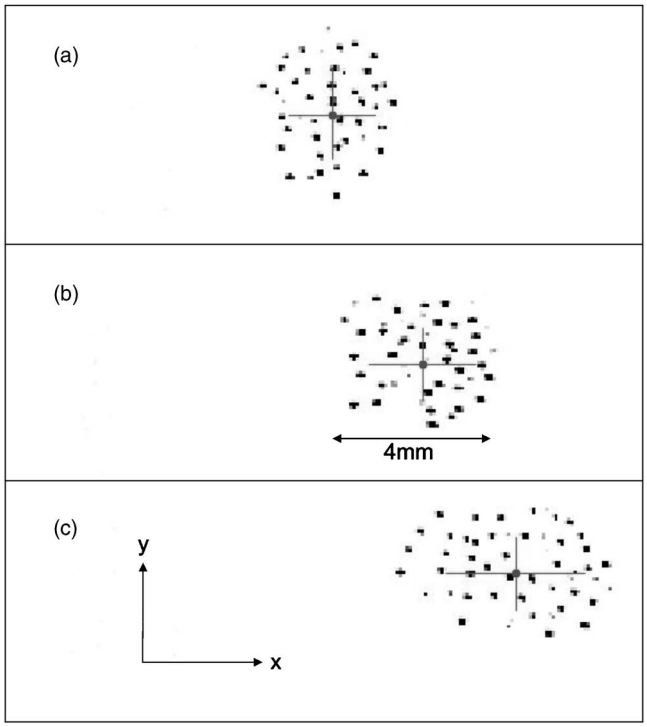

FIG. 6. Inverted-intensity image of the dust cloud in different phases of the motion. (a) Left turning point of the motion, (b) equilibrium position, (c) right turning point. The c.o.m. position x_{com} and the deformations d_x, d_y are indicated with bars.

$U_{\mathrm{mod}}=10$ V_{pp}. We find that the dust particles in this small cloud are not crystallized but perform a fast irregular motion. The figure shows the shape of the dust cloud (a) at the left turning point, (b) at the equilibrium position, and (c) at the right turning point. It becomes evident that the cloud is axially compressed in panel (a) whereas it is stretched in panel (c). Hence we can distinguish two different effects: The cloud performs a periodic center-of-mass motion along the x-direction, which is aligned with the magnetic field. Simultaneously, the cloud experiences a quadrupole-like deformation, which, however, is only seen in a cross section. The two processes can be quantified by studying the center-of-mass (c.o.m.) coordinate of the dust cloud, which we can estimate from the center of scattered light intensity in a movie frame. Let $B_{i,j}$ be the brightness of a pixel at coordinates (x_i, x_j). Then the center of mass becomes

$$x_{\mathrm{com}}(t) = \frac{1}{B_{\mathrm{tot}}(t)} \sum_{i=0}^{N-1} \sum_{j=0}^{M-1} x_j B_{ij}(t), \tag{2}$$

where $B_{\mathrm{tot}}(t)=\Sigma_i \Sigma_j B_{ij}(t)$ is the total intensity in that frame and x_j is the x-coordinate corresponding to pixel index j. Likewise, the stretching of the dust cloud is obtained by calculating the second moment of the intensity distribution

$$d_x^2 = \frac{1}{B_{\mathrm{tot}}(t)} \sum_{i=0}^{N-1} \sum_{j=0}^{M-1} [x_j - x_{\mathrm{com}}(t)]^2 B_{ij}(t). \tag{3}$$

The sloshing amplitude in the x-direction is dependent on the applied frequency (full circles) in Fig. 7. The c.o.m. motion at the lowest frequency ($f_{\mathrm{mod}}=1$ Hz) is representative for the

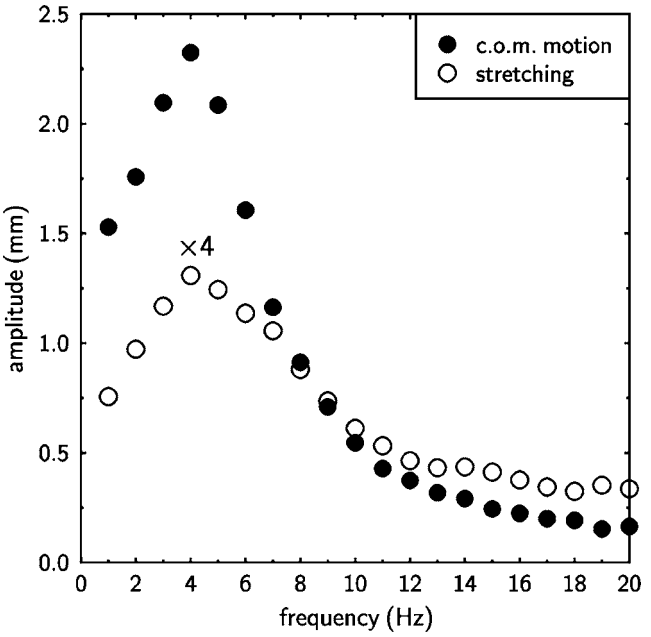

FIG. 7. Sloshing amplitude and stretching amplitude of a small dust cloud as a function of modulation frequency. Both amplitudes show a resonance maximum at 4 Hz.

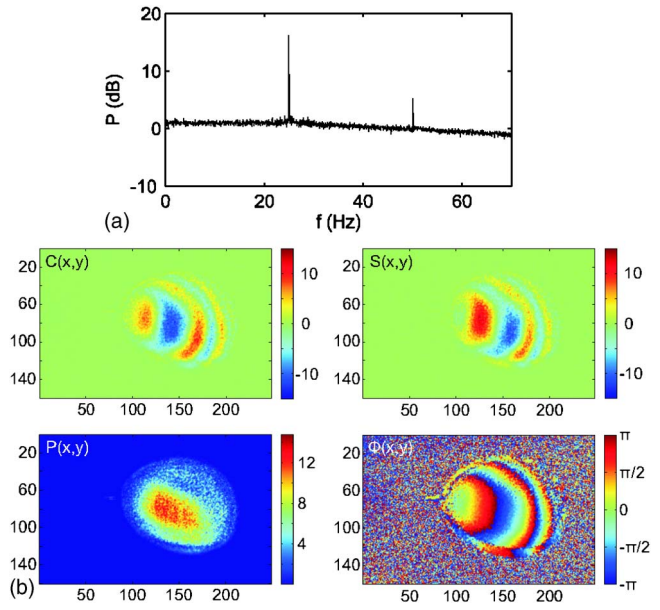

FIG. 8. (Color online) (a) Average spectral power density of the fluctuations of scattered light in a central square of 21×21 pixels. (b) Reconstructed wave function in terms of real part $C(x,y)$ and imaginary part $S(x,y)$ as well as intensity distribution $P(x,y)$ and phase $\phi(x,y)$.

static shift of the dust cloud's equilibrium position with applied anode bias U_a. With increasing frequency, the sloshing amplitude becomes larger and attains a maximum at 4 Hz. For even larger frequencies, the sloshing amplitude decreases slightly more rapidly with increasing frequency. Obviously, the sloshing motion has a resonant response to the external modulation. A similar behavior with a resonance at the same frequency is found for the stretching of the dust cloud (circles in Fig. 7). A periodic motion of the c.o.m. and a quadrupole deformation is also observed in medium sized dust clouds, however, with a lower amplitude than for small clouds.

V. THE PHASE FRONTS OF DUST DENSITY WAVES

Here, we analyze the phase evolution of a dust density wave in the central horizontal section of the dust cloud. We can make use of the wave information contained in a long movie consisting of F frames by observing that the spectral power density has a dominant sharp peak at the frequency f_{mod} and has an additional peak at its harmonic $2f_{\mathrm{mod}}$, which together represent the coherent wave motion, see Fig. 8(a).

For the determination of the phase fronts from a given movie, the brightness distribution in each frame $B_k(x,y)$ of the movie at time t_k is projected on the fundamental modes $\sin(2\pi f_{\mathrm{mod}}t)$ and $\cos(2\pi f_{\mathrm{mod}}t)$. The smaller contribution of the second harmonic is presently neglected. In this way, we obtain the complex spatial wave function $C(x,y)+\mathrm{i}S(x,y)$,

$$S(x,y)=\sum_{k=1}^{F}B_k(x,y)\sin(2\pi f_{\mathrm{mod}}t_k), \tag{4}$$

$$C(x,y)=\sum_{k=1}^{F}B_k(x,y)\cos(2\pi f_{\mathrm{mod}}t_k). \tag{5}$$

From the complex wave function we deduce the phase distribution $\phi(x,y)$ and the wave intensity $P(x,y)$,

$$\phi(x,y)=\arctan\left(\frac{S(x,y)}{C(x,y)}\right), \tag{6}$$

$$P(x,y)=\sqrt{S(x,y)^2+C(x,y)^2}. \tag{7}$$

These four functions are compiled in Fig. 8(b), which was recorded with the eightfold supersampling technique. The complex wave function confirms the result of the stroboscopic measurement in Fig. 3 that the wave fronts are curved. This curvature and the origin of the wave from a spot on the left-hand side of the dust cloud become even more evident in the phase distribution. The wave amplitude decreases towards the edge of the dust cloud.

Because the individual slices have a fixed phase relationship we can deduce the shape of the phase fronts in a vertical section through the center of the dust cloud from a sequence of horizontal sections. In Fig. 9 the resulting wave function is shown as real and imaginary part. For comparison, the shape of the dust cloud is indicated by the dotted boundary line. The wave fronts are inclined and show that the wave propagation has both an axial and a downwards component. This orientation is compatible with the assumed ion flow direction which has the same pattern.

VI. WAVE DISPERSION

The dispersion of the density wave is estimated from the apparent wavelength λ^* measured in a horizontal section of the dust cloud. The true wavelength λ corresponds to the perpendicular distance between two wave fronts as seen in Fig. 9 and $\lambda=\lambda^*\cos\alpha$, where α is the inclination of the propagation vector $\vec{k}$ with respect to the horizontal. We use

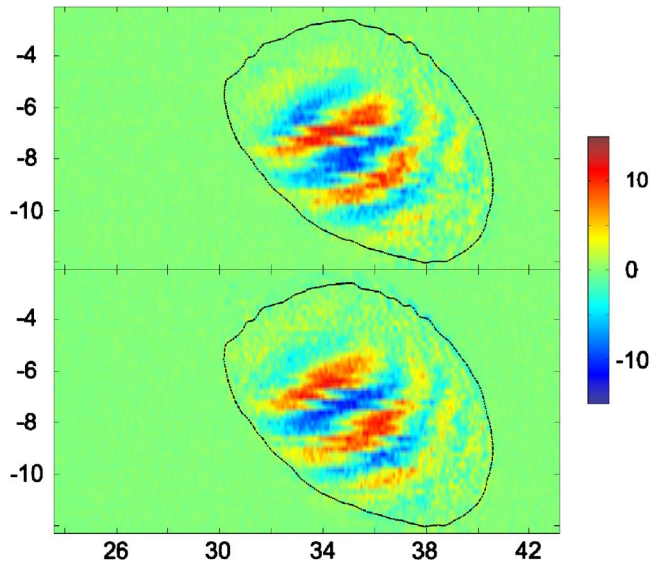

FIG. 9. (Color online) The reconstructed real (top) and imaginary part (bottom) of the wave function in a vertical section of the dust cloud. The labels give the x and z coordinates (in mm) with respect to the center of the anode disk. The boundary of the dust cloud is marked by the dotted line.

an estimate of $\alpha \approx 45°$ in the following. This measured wavelength λ^* varies with the modulation frequency f_{mod} as shown in Fig. 10.

For comparison, we have plotted the long wavelength limit of the dust acoustic wave dispersion, $\omega = \omega_{pd}\lambda_D k$, and the cylindrical-waveguide mode of Shukla and Rosenberg,[10] which, when dust neutral collisions are neglected, is given by

$$\omega = \omega_{pd}\left[\frac{k^2+\gamma^2}{k_D^2+k^2+\gamma^2}\right]^{1/2}. \tag{8}$$

Here, $k_D = 1/\lambda_D$ and $\gamma = 2.4/R$ represents the fundamental mode. This gives (at $k=0$) a cutoff frequency $\omega_{\mathrm{min}} = \omega_{pd}\,\gamma(k_{\mathrm{D}}^2+\gamma^2)^{-1/2}$. At our experimental conditions ($n_d = 1.7\times 10^{10}$ m^{-3}, $Z_d = 3000$) we obtain $\omega_{pd} \approx 780$ s^{-1}. The diameter $2R \approx 5$ mm of the waveguide is estimated from the transverse dimension of the dust cloud in Fig. 9.

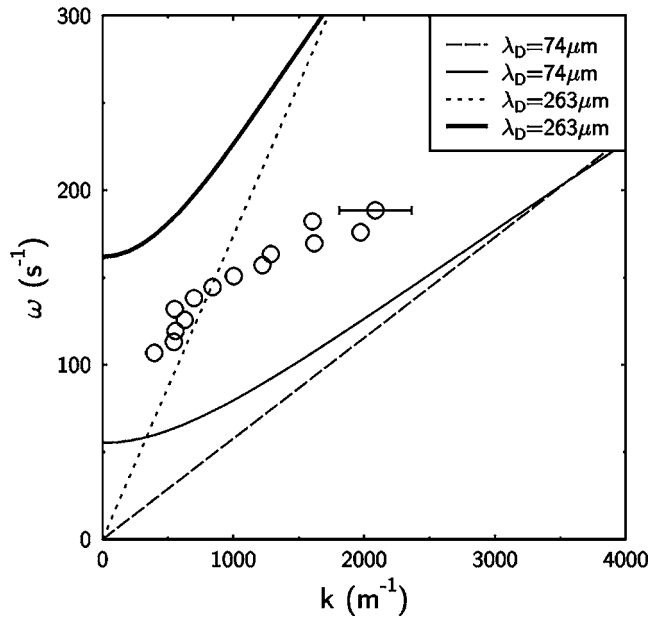

FIG. 10. Measured dispersion in the center of a small dust cloud in comparison with the acoustic dispersion of a dust acoustic wave (dashed and dotted line) and the fundamental waveguide mode from Ref. 10 (full lines).

For the waveguide mode we consider two limiting cases. In the first case, assuming thermal ions with $k_B T_i = 0.1$ eV, the ion Debye length becomes $\lambda_{Di} = 74$ μm and, because $T_e \gg T_i$, $\lambda_D \approx \lambda_{Di}$. Then the dust acoustic velocity becomes 74 mm/s, which is smaller than the observed phase velocities. In the second case, we assume that the ions have the Bohm speed, $v_B = \omega_{pi}\lambda_{D,e}$. In this limit, ion shielding is reduced and the estimated ion shielding length is $\lambda_{D,i} \approx \lambda_{D,e}$, which results in $\lambda_D \approx 2^{-1/2}\lambda_{D,e}$.

The data points lie between both limiting cases and show that, in the experiment, the group velocity is smaller than the phase velocity. This effect is different from a dust acoustic wave, which has identical group and phase velocity in the long-wavelength limit. Such a difference, however, is found in the waveguide modes as a consequence of the frequency cutoff.

VII. DISCUSSION

A. Confinement

The small dust clouds were found vertically displaced from the axis of the anodic plasma. One could imagine that the levitation might be described by the balance of weight force and electric field force, $m_d g = Z_d e E_r$. For the known electric field $E_r \approx 10^3$ V m^{-1}, however, the dust charge estimate becomes $Z_d = 48$ only, which is unreasonably small. The model for axial confinement[7] required $Z_d \approx 2000-3000$ instead. Hence, the radial confinement is also determined by a balance of ion drag force and electric field force. This means that the observed radial displacement from the center of the anodic plasma is equivalent to the formation of a dust-free void[20] in the center, as observed in rf discharges under microgravity.[21] The force balance at the void edge was recently quantified experimentally.[22]

For slightly different plasma parameters and using a large amount of dust, we have found a toroidal shape of the dust cloud with a central hole. This is an immediate hint at the formation of a central void region. In an earlier investigation[7] we had shown that the critical electric field for void formation, at our present plasma parameters, has the value of ≈ 180 V m^{-1}. Comparing the potential contours in Fig. 2, this is a realistic value expected at the position $z = -3$ mm, where the force equilibrium for the top side of the spheroidal cloud is established.

B. Structure

The formation of stripes on the topside of a small dust cloud can be understood by crystallization in the top layer and slow rotation of the cloud about the magnetic field direction. The observed pattern is different from the nested shell structure found in Yukawa balls.[13] The assumed dust charge $Z_d = 3000$ is sufficiently large that the Coulomb coupling parameter $\Gamma = (Z_d e)^2/(4\pi\epsilon_0 a_{\mathrm{WS}} k_B T_d)$ attains a large value $\Gamma = 1900$. Here, $a_{\mathrm{WS}} = [3/(4\pi n_d)]^{1/3}$ is the Wigner-Seitz

radius, which becomes $a_{WS}=271\ \mu$m at $n_d=1.2\times10^{10}\ \mathrm{m}^{-3}$. For comparison, the critical values for melting in an extended system with Yukawa interaction with a shielding factor $\kappa=a_{WS}/\lambda_D$ are $\Gamma_{crit}=172,217,440,1185,\ldots$ for $\kappa=0,1,2,3,\ldots$.[23] Therefore, the parameters in our system allow crystallization provided that $\kappa\leqslant3$ and that the dust is at room temperature.

Rotational motion of dust clouds in a magnetic field is attributed to the azimuthal component of the ion motion that exerts a weak torque on the dust cloud. For our experimental conditions, the ion Hall parameter takes a value of $\omega_{ci}/\nu_{in}\approx0.1$, which means that the ion velocity is preferentially oriented in the electric field direction and has a smaller azimuthal component, which is 10% of that velocity. Although the torque is weak, the damping rate of the rotational motion by dust-neutral friction is also small and allows a constant rotation. The orientation of the electric field direction can be estimated from Fig. 2(a). At a distance of $x=36$ mm from the anode and $z=-8$ mm, which corresponds to the center of the dust cloud in Fig. 9, the electric field has an inclination of 60°–80° from the horizontal. This compares fairly well with the inclination of the wavevector in Fig. 9.

The fact that the top layers of the dust cloud are crystalline while the lower layers are found in a liquid state may be explained by the excitation of the dust density wave. This wave attains large amplitudes in the center of the cloud, which results in particle displacements that exceed the Lindeman melting criterion.[24] Because the ion streaming direction has both an axial and a downward component, it is not surprising that the top layer, where the wave has small amplitude, can remain crystalline while the growing wave amplitude leads to the melting down to the bottom of the cloud.

C. Sloshing and stretching

The observed sloshing motion attains a resonant enhancement at a frequency of 4 Hz. For comparison, the eigenfrequency determined by the curvature of the effective potential well shown in Fig. 2(b) at its lowest point is 12.6 Hz. This difference can be explained by assuming a weaker curvature of the confining well at the position of the small dust cloud.

The observed stretching of the dust cloud cannot be explained by the periodic motion in a strictly parabolic confining potential. In that case, the particle cloud would move like a rigid body. The typical confining well shown in Fig. 2(b), however, has an asymmetric shape with a pronounced "softening" that becomes visible as an inflection on the right-hand side. Hence, such an asymmetry, which we also expect for the confining well of the small dust cloud, allows for a stretching at the right turning point and a compression at the left turning point.

D. Phase fronts of dust density waves

Different from the observation in extended dust clouds,[2,7] where the approximation of nearly plane waves could be justified, the phase fronts in small dust clouds have a pronounced curvature. This was already seen in the stroboscopic image in Fig. 3 and becomes even more pronounced in the small dust cloud in Fig. 8. Apparently, the waves emerge from a spot at the left-hand side of the dust cloud and form a set of sickle-shaped regions that propagate to the right.

One could imagine that the wave fronts are determined by the eigenmodes of a small spheroidal cloud. Such eigenmodes are composed of forward and reflected waves. In the present case, the forward wave is an unstable wave that is fed by the streaming ions. In the observed plane the ions have an axial (parallel to x) and radial (parallel to $\pm y$) velocity. Therefore, all parts of the curved wave front can be considered as being amplified by the ion streaming motion. The opposite situation is found for any reflected wave, which propagates against the ion flow. Consequently, the reflected wave is damped with a damping length comparable to the wavelength. The damping of the reflected wave is therefore responsible for the nonestablishment of global standing waves.

We could extract the vertical structure of the wave fronts from a set of individual horizontal slices which were mutually phase synchronous. The wave fronts are asymmetric with respect to the dust cloud and describe a propagation direction that has an axial and a downward component. This orientation is consistent with the expected ion streaming direction.

E. Wave dispersion

We have found that because of the inclined wave propagation with respect to a horizontal section of the cloud, the apparent wavelength λ^* is longer than the true wavelength λ. Varying the wave frequency, we find a dispersion that deviates from the dust acoustic wave in an infinite medium. The group velocity is found smaller than the phase velocity. This behavior is found consistent with the waveguide mode,[10] and can be attributed to a frequency cut-off. A similar frequency cutoff was found for dust acoustic waves in a plasma slab,[12] which can be considered as a dielectric waveguide. Therefore, the influence of the finite transverse dimension of the dust cloud is insensitive to the kind of boundary condition (metallic/dielectric). Although the model of a cylindrical waveguide is only a rough approximation for a small dust cloud, the essential feature that results from a frequency cutoff is reproduced in our experiment.

F. Consistency of the observations

The crystallization of medium size dust clouds requires that $\kappa<3$. Therefore, the linearized Debye length must be $\lambda_D>150\ \mu$m. Such an increase beyond the thermal ion Debye length (74 μm) is expected when the ion drift speed comes close to the Bohm velocity. The ion mobility and the radial electric field at the position of confinement result in such a high speed. Hence, the structural properties of and the wave dispersion in medium size dust clouds can be described by a consistent set of plasma parameters.

The Schweigert instability[25,26] involves chain formation by wakefield attraction and excitation of short-wavelength transverse modes, which eventually lead to melting of plasma crystals. It was observed in unmagnetized plasmas

with multilayer dust systems in the sheath of radio-frequency discharges. This instability appears for ion drift speeds that exceed the Bohm speed. In the present experiments, the ion drift speed is close to the Bohm speed. Therefore, we cannot rule out that wakefield attraction is also acting here. In medium size dust clouds, the unstable dust density wave may mask the Schweigert instability. One could also speculate that a contribution from wakefield attraction favors the fourfold symmetry in parts of the crystallized top layers. In small dust clouds, the appearance of a fluid phase with high dust velocities may hint at the action of the Schweigert instability.

The large dust clouds studied in Ref. 7 are not affected by a vertical inclination of the wave front because these clouds were nearly centered with the anode disk. Therefore, a distinction between λ and λ^* was unnecessary. Moreover, the cross section of the cloud was larger by a factor of 2–3. Since the radius of the waveguide enters as $1/R^2$ in Eq. (8), the influence of the frequency cut-off becomes negligible and the interpretation of the wave dispersion in terms of a kinetic model is not affected by our new finding.

In summary, we present a first exhaustive survey of the structure and dynamical features of small and medium size dust clouds. Novel findings are the void formation in a dc discharge, the strict alignment of a crystal axis perpendicular to the magnetic field, and the competition of sixfold and fourfold symmetry. The full three-dimensional structure of the phase fronts of dust density waves reveals that the waves propagate in the direction of the local electric field.

ACKNOWLEDGMENTS

The present investigations were financially supported by DFG within the transregional collaborative research center TR-24, Project No. A2. M.E.K. acknowledges partial support by the U.S. NSF.

[1] N. N. Rao, P. K. Shukla, and M. Y. Yu, Planet. Space Sci. **38**, 543 (1990).
[2] C. Thompson, A. Barkan, N. D'Angelo, and R. L. Merlino, Phys. Plasmas **4**, 2331 (1997).
[3] A. V. Zobnin, A. D. Usachev, O. F. Petrov, and V. E. Fortov, JETP **95**, 429 (2002).
[4] S. Ratynskaia, M. Kretschmer, S. Khrapak, R. A. Quinn, M. H. Thoma, G. E. Morfill, A. Zobnin, A. Usachev, O. Petrov, and V. Fortov, IEEE Trans. Plasma Sci. **32**, 613 (2004).
[5] S. Ratynskaia, S. Khrapak, A. Zobnin, M. H. Thoma, M. Kretschmer, A. Usachev, V. Yaroshenko, R. A. Quinn, G. E. Morfill, O. Petrov, and V. Fortov, Phys. Rev. Lett. **93**, 085001 (2004).
[6] E. Thomas, Jr., Phys. Plasmas **13**, 042107 (2006).
[7] T. Trottenberg, D. Block, and A. Piel, Phys. Plasmas **13**, 042105 (2006).
[8] M. Rosenberg, J. Plasma Phys. **67**, 235 (2002).
[9] A. Piel, M. Klindworth, O. Arp, A. Melzer, and M. Wolter, Phys. Rev. Lett. **97**, 205009 (2006).
[10] P. K. Shukla and M. Rosenberg, Phys. Plasmas **6**, 1038 (1999).
[11] N. X. Wei and J. K. Xue, Phys. Plasmas **13**, 052101 (2006).
[12] V. Yaroshenko, H. Thomas, and G. Morfill, Phys. Plasmas **14**, 082104 (2007).
[13] O. Arp, D. Block, and A. Piel, Phys. Rev. Lett. **93**, 165004 (2004).
[14] O. Arp, D. Block, M. Klindworth, and A. Piel, Phys. Plasmas **12**, 122102 (2005).
[15] L. Malter, E. Johnson, and W. Webster, RCA Rev. **12**, 415 (1951).
[16] B. Song, N. D'Angelo, and R. Merlino, J. Phys. D **24**, 1789 (1991).
[17] T. An, R. Merlino, and N. D'Angelo, J. Phys. D **27**, 1906 (1994).
[18] E. Thomas and M. Watson, Phys. Plasmas **6**, 4111 (1999).
[19] E. Thomas, Phys. Plasmas **8**, 329 (2001).
[20] J. Goree, G. E. Morfill, V. N. Tsytovich, and S. V. Vladimirov, Phys. Rev. E **59**, 7055 (1999).
[21] G. E. Morfill, H. M. Thomas, U. Konopka, H. Rothermel, M. Zuzic, A. Ivlev, and J. Goree, Phys. Rev. Lett. **83**, 1598 (1999).
[22] M. Wolter, A. Melzer, O. Arp, M. Klindworth, and A. Piel, IEEE Trans. Plasma Sci. **35**, 266 (2007).
[23] S. Hamaguchi, R. Farouki, and D. H. E. Dubin, Phys. Rev. E **56**, 4671 (1997).
[24] J. P. Hansen and I. R. McDonald, *Theory of Simple Liquids*, 2nd ed. (Academic, London, 1990).
[25] A. Melzer, V. Schweigert, I. Schweigert, A. Homann, S. Peters, and A. Piel, Phys. Rev. E **54**, R46 (1996).
[26] V. A. Schweigert, I. V. Schweigert, A. Melzer, A. Homann, and A. Piel, Phys. Rev. E **54**, 4155 (1996).

B.2

TORUS-SHAPED DUST CLOUDS TRAPPED IN A MAGNETIZED ANODIC PLASMA

I. Pilch, T. Reichstein, and A. Piel

Reprinted with permission from
I. Pilch, T. Reichstein, and A. Piel,
Physics of Plasmas, Vol. 15, Page 103706 (2008).

Torus-shaped dust clouds trapped in a magnetized anodic plasma

Iris Pilch,[a] Torben Reichstein, and Alexander Piel
IEAP, Christian-Albrechts-Universität, D-24098 Kiel, Germany

(Received 25 September 2008; accepted 1 October 2008; published online 31 October 2008)

Dust particles confined in a magnetized anodic plasma can form a torus-shaped cloud with a dust-free region (void) in the center. Most of the dust particles perform a rotational motion about the major axis of the torus. The torus-shaped dust cloud and the velocity of the particles are studied by varying the external plasma parameters like magnetic field strength and rf-power of the source plasma. Two-dimensional potential contours are measured with an emissive probe. The results are used to discuss the force balance between electric field force and ion drag acting on the dust particles that determines the void size. © *2008 American Institute of Physics*.
[DOI: 10.1063/1.3006085]

I. INTRODUCTION

In dusty plasmas, dust-free regions occur when the ion drag force on the particles exceeds the opposing electric field force and pushes the particles out of the central region. This phenomenon is well known for radio-frequency (rf) discharges under microgravity,[1,2] where dust is inserted into the discharge, and plasma processing discharges,[3–5] where dust particles are growing and a periodic growth and collapse of the dust cloud was observed. In both experiments the plasma production takes place in the central region of the discharge. The ions, produced in the center, are drifting radially outwards. This ambipolar diffusion of the ions is acting on the dust particles as the ion drag force[6–9] and pushes the particles out of the central region until the particles have reached an equilibrium position established by the ion drag force and the inward-directed electric field force. This equilibrium position has a sharp boundary and particles are separated according to their grain size. A quantitative description of this mechanism could be achieved by computer simulations.[10–13] Voids are also found in the vicinity of Langmuir probes.[14,15] The mechanism of those voids is similar, but in that geometry the confinement is induced by an inward-directed ion drag force and an outward-directed electric field force.

In two-dimensional dust clusters dust-free regions can also be observed.[16,17] These clusters are orientated parallel to the electrode and confined in the sheath of the rf plasma. Here, void formation is different from the mechanism in the volume of the rf discharge. The void in two-dimensional clusters can be explained with a force balance between the dust particles[16] and recently it was found, in molecular dynamics simulations, that the void in the plasma crystal is due to a potential bump caused by the cylindrical symmetry.[17]

The influence of a magnetic field perpendicular to the two-dimensional dust cluster was investigated by Konopka *et al.*[18] and analyzed by means of simulation in Ref. 19. It was found that the cluster performed a rigid-body rotation or a sheared rotation depending on the discharge parameters. In a recent experiment the role of the neutral gas in cluster rotation was examined by Carstensen *et al.*[20]

In anodic plasmas[21–23] dust clouds without a void region can be confined. Barkan *et al.*[21] have reported a dust ball which performs a rigid-body rotation in the $E\times B$ direction of the ions due to a magnetic field. Recently, we have reported the formation of a torus-shaped dust cloud with a void in the central region, which are confined in a magnetized anodic plasma.[24] The particles confined in the torus are rotating in the $E\times B$ direction of the ions.

In the present paper we analyze this phenomenon in more detail with emphasis on the existence regime, the shape and the rotation of the dust clouds. The paper is organized as follows. In Sec. II a brief description of the experimental setup is given. The dependence of the torus-shaped dust cloud on the discharge parameters is described in Sec. III. Emissive probe measurements and the calculation of the ion drag are given in Sec. IV. The experimental results are discussed in Sec. V.

II. EXPERIMENTAL SETUP AND DIAGNOSTICS

The experiment consists of a primary source plasma, which is generated by a radio-frequency plasma ($f=27.12$ MHz) at a low power of 1–15 W. A secondary anodic plasma is generated in front of a positively biased disk anode. A detailed description of the experiment was given in Refs. 22 and 24. A sketch of the anodic plasma is shown in Fig. 1. The anode is operated at voltages of 60–90 V and low currents of 5–14 mA. The experiments are performed in argon gas at pressures of 3–8 Pa. The magnetic field has a strength of about 5–150 mT. Typical plasma parameters are density $n_e\approx 10^{15}$ m^{-3} and electron temperature $T_e=3$ eV. These parameters can be measured with an axially movable and rotatable emissive probe or Langmuir probe. Because of the scattering of ions, i.e., ion-neutral collisions, the ion temperature is larger than the neutral temperature and reaches $T_i\approx 0.1$ eV.[22]

For our experiments we use spherical monodisperse dust particles (melamine formaldehyde) of (0.97 ± 0.05) μm diameter. The dust is confined in the anodic plasma by a force balance of the electric field and ion drag force. The axial confinement of dust clouds in front of an anode disk was studied in detail by Trottenberg *et al.*[22]

[a]Electronic mail: pilch@physik.uni-kiel.de.

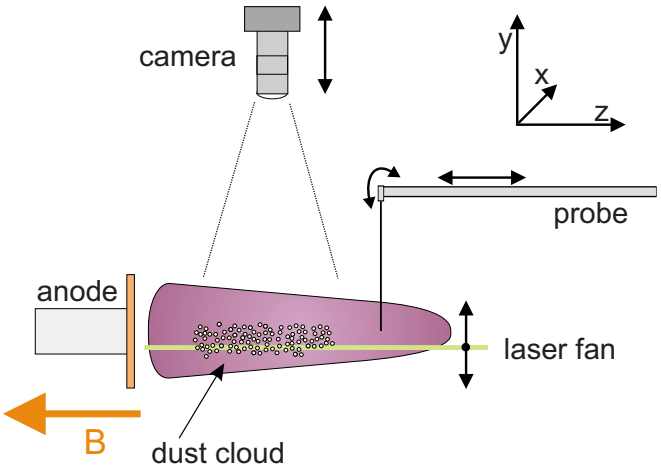

FIG. 1. (Color online) A dust cloud is trapped in the anodic plasma and observed with a combination of a horizontal laser fan and camera, which can be placed at any vertical position. An emissive or a Langmuir probe can be used to diagnose the anodic plasma in a horizontal midsection. A sketch of the used coordinate system is shown.

Our observation geometry is shown in Fig. 1. The dust cloud is illuminated by a laser fan ($\lambda = 532$ nm, 200 mW) and the scattered light is recorded by a camera viewing from the top side at right angle. The camera is a CCD camera with a frame rate of 150 fps at maximum resolution (480×640 pixels). By using a region of interest the frame rate can be increased up to 473 fps. Camera and laser fan are together mounted on a translation stage and can be vertically positioned to image any horizontal plane of the dust cloud.

For our experiments we have used two different recording methods. To record the three-dimensional shape of the dust cloud, we are scanning vertically through the dust cloud at a low frame rate to reduce the amount of data, because we are not interested in single particle motion. For recording the motion of particles in a fixed horizontal section of the dust cloud, we typically choose three sections: the midsection to observe the change of the torus size and a section of the top and of the bottom to measure the horizontal velocity of the particles.

The coordinate system we are using is sketched in Fig. 1. The z-axis is aligned with the magnetic field direction, the x-axis lies in the horizontal plane, and the y-axis defines the vertical scanning direction.

III. DUST CLOUDS IN MAGNETIZED PLASMA

A. Topology of dust clouds

The three-dimensional shape of the dust cloud is reconstructed from a vertical scan through the cloud with a low frame rate of 25 fps. First we have subtracted an offset image to remove spurious light reflections from the anode disk. Then we have increased the scattered light intensity by averaging over five consecutive frames. A three-dimensional matrix was built with these images and the boundary of the cloud was then calculated with a contour algorithm.[25]

In Fig. 2, three types of dust clouds are shown for different magnetic fields. The field direction points away from the anode. The vertical scans were performed at gas pressure

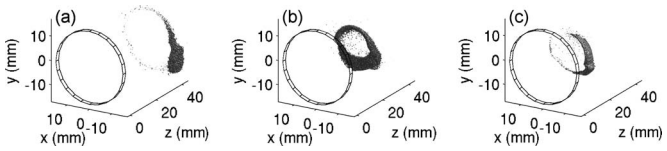

FIG. 2. Three-dimensional reconstruction of a dust cloud for constant discharge parameters of pressure $p \approx 5.4$ Pa, rf-power $P_{rf} = 3$ W and anode voltage $U_A \approx 65$ V at (a) low magnetic field ($B = 10$ mT, $I_A = 14.1$ mA), (b) medium magnetic field ($B = 20$ mT, $I_A = 12.3$ mA), and (c) high magnetic field ($B = 74$ mT, $I_A = 4.8$ mA).

($p \approx 5.4$ Pa), rf-power ($P_{rf} = 3$ W), and anode voltage ($U_A \approx 65$ V). Note that the anode current varies with the magnetic field. For increasing magnetic field, the anode current increases up to a magnetic field of $B \approx 15$ mT and decreases again for higher magnetic field.

In earlier experiments[24] we had found that an elliptic dust cloud forms at weak magnetic field and lower gas pressure, which was vertically displaced from the axis through the anode disk. At high magnetic field and higher gas pressure, a torus-shaped dust cloud appeared. Here we study the formation of these clouds in detail.

In Fig. 2(a) a strongly asymmetric torus is found at low magnetic field ($B = 10$ mT, $I_A = 14.1$ mA). A few particles are found to rotate in the counterclockwise direction about the major axis when seen from the anode. The center of the cloud is dust-free and the center of mass of the cloud is

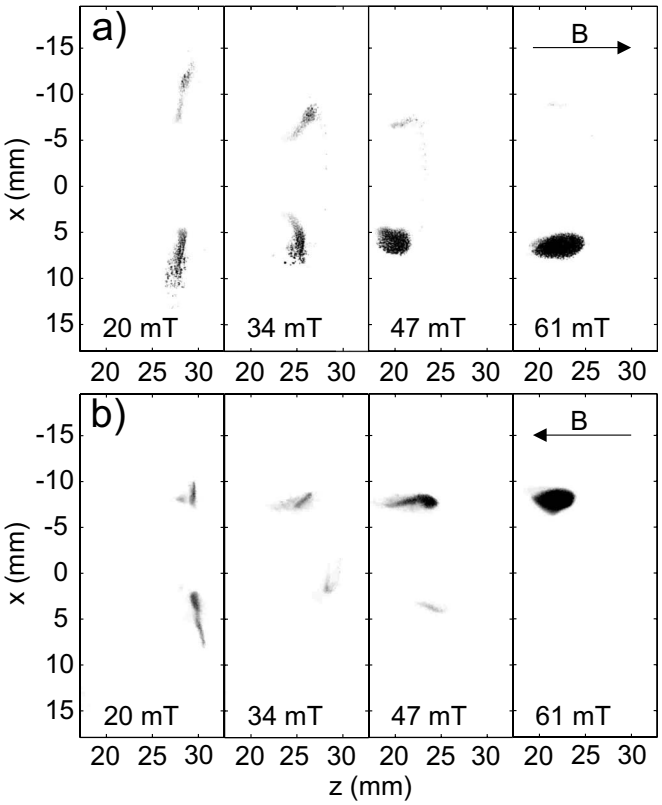

FIG. 3. A time averaged horizontal section through the midplane is shown for different strength and sign of the magnetic field. (a) Magnetic field is pointing towards and (b) away from the anode. With increasing magnetic field the torus becomes asymmetric and disappears at high magnetic field of 61 mT.

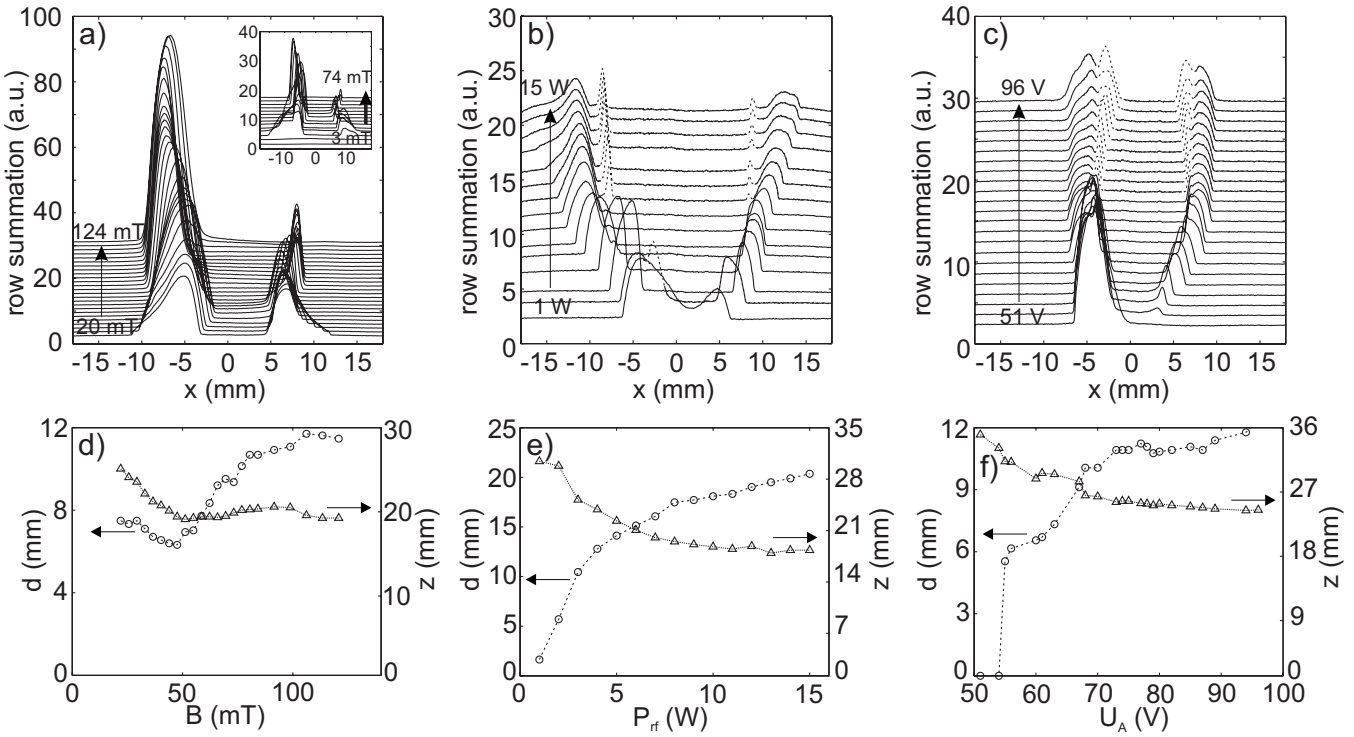

FIG. 4. Waterfall diagrams of the row summation of the time-averaged horizontal slices for a variation of (a) the magnetic field (P_{rf}=3 W, U_A=67 V, p=5.4 Pa), (b) the primary discharge rf-power (B=20 mT, U_A=67 V, p=5.4 Pa), and (c) the anode voltage (B=20 mT, P_{rf}=3 W, p=5.4 Pa). The inner diameter d (circles) and the axial position z (triangles) of the torus towards the anode are shown for (d) the magnetic field variation, (e) the rf-power variation, and (f) the anode voltage variation.

shifted from the anode axis sidewards in the $+x$ direction and downwards. When the magnetic field is decreased further, only a displaced cloud is found and no particle rotates about the axis. These clouds at low magnetic field, however, are difficult to study in detail, because the confinement of the dust particles becomes weak and particles are gradually lost. For higher magnetic field (B=20 mT, I_A=12.3 mA), as shown in Fig. 2(b), a nearly symmetric torus is formed. If the magnetic field is increased further (B=74 mT, I_A=4.8 mA), Fig. 2(c), the torus becomes asymmetric again and only some particles are able to rotate about the major axis. For even higher magnetic field the torus collapses.

To observe the reaction of the dust cloud to the external discharge parameters a fixed section of the midplane is observed while one parameter was varied. In Fig. 3(a) a time-averaged image is shown for different magnetic field strength. The anode is located on the left side (z=0 mm) of the figure. In this set of experiments, the magnetic field is orientated in the $+z$ direction. The time-averaged midsections are taken from a vertical scan and compromise a layer of Δy=0.8 mm. The number of averaging frames is typically 20 and the averaged intensity profile shows some residual grain structure.

At low magnetic field (B=20 mT) the torus is slightly asymmetric and has a flat shape. By increasing the magnetic field to 34 mT, the torus diameter and the distance from the anode is reduced. The torus is slightly tilted with respect to a plane z=const. The shape of the torus becomes more asymmetric and the dust cloud is shifted in the direction of the drifting ions. At high magnetic field (B=61 mT) the torus has collapsed, and a radially displaced cloud remains. We conjecture that the displacement of the cloud and the toroidal particle rotation are caused by the azimuthal component of the ion drag force. To verify this shift, we have inverted the magnetic field direction and with it the azimuthal component of the ion drift [Fig. 3(b)]. The magnetic field now points towards the anode. The same qualitative behavior is seen again. With increasing magnetic field the torus size and the distance to the anode is reduced. The dust is now pushed in the opposite direction, as expected from the different rotation direction of the ion wind.

The change of the torus diameter and the amount of mass in the torus branches can be analyzed in a quantitative manner in Fig. 4. Here, the row-summed intensity is plotted versus x in terms of a waterfall diagram. In Fig. 4(a) the magnetic field is varied (P_{rf}=3 W, U_A=67 V, p=5.4 Pa), in Fig. 4(b) the rf-power (B=20 mT, U_A=67 V, p=5.4 Pa) and in Fig. 4(c) the anode voltage (B=20 mT, P_{rf}=3 W, p=5.4 Pa). Note that the step width of the magnetic field and the anode voltage variation is not equidistant. In Figs. 4(d)–4(f) the modification of the torus is shown in more detail. The diameter of the dust-free center (circles) and the z-position of the center of mass (triangles), i.e., the distance from the anode, are plotted over the variation parameter, (d) magnetic field, (e) rf-power, and (f) anode voltage.

For the magnetic field variation in Fig. 4(a), it is found that the torus diameter first slightly decreases and then increases until a nearly constant value of about 11 mm is reached. Also the asymmetric branches of the torus can be seen. The intensity in the left branch of the torus rises with

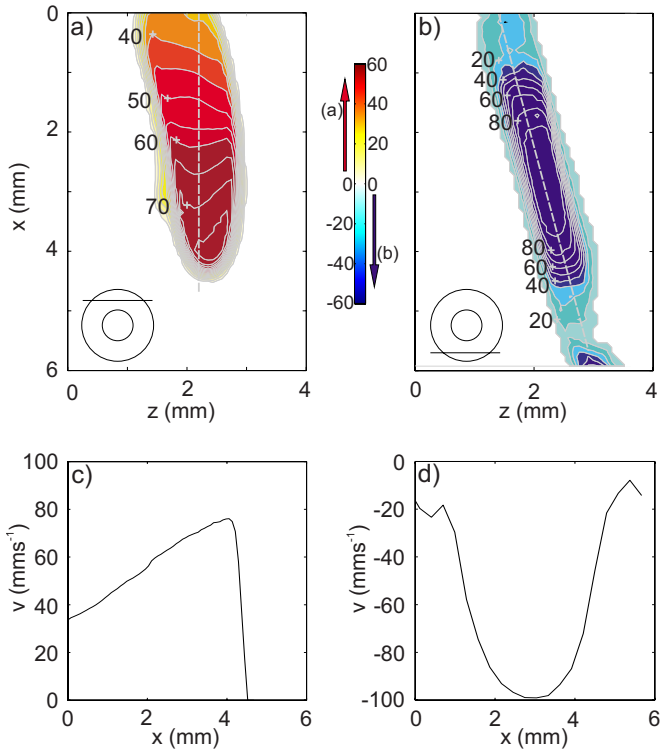

FIG. 5. (Color online) Particle image velocity measurement of the horizontal component of the particle velocity (a) in the upper part and (b) in the lower part of the torus as indicated by the insets. A section through the velocity profile is plotted vs x for (c) the upper part and (d) the lower part of the torus. The position of the section is indicated with a dashed line in (a) and (b).

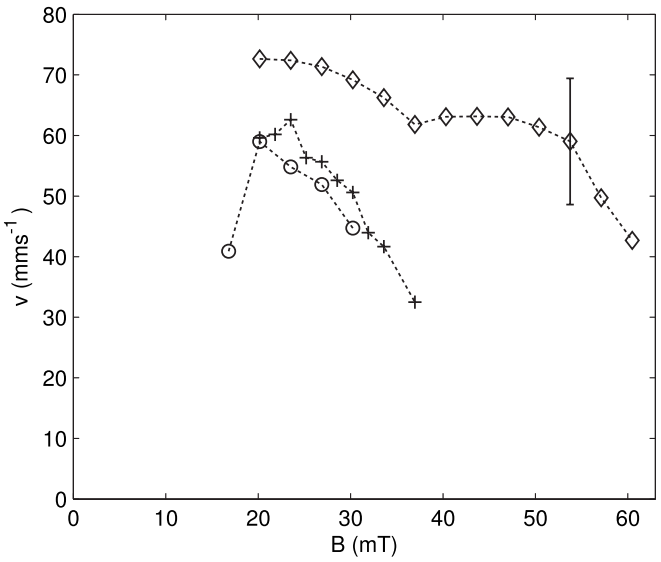

FIG. 6. The dependence of the particle velocity on the magnetic field was measured in the top section of the torus. Shown are the results for different pressures of 5.8 Pa (circles), 6.3 Pa (crosses), and 7.9 Pa (diamonds).

increasing magnetic field. Whereas the maximum amplitude in the right arm is nearly constant, the width decreases. In this dataset the torus does not completely disappear at high magnetic field, but we expect that this would happen if the magnetic field strength was further increased. The inset in Fig. 4(a) shows a second measurement of the magnetic field variation with less data points, which was performed directly after the first run. The same behavior as before is observed, but the intensity is reduced, because dust was lost at high magnetic field strength. In Fig. 4(d) the movement of the torus is shown in more detail. With increasing magnetic field the distance from the anode decreases until a constant value of 20 mm is reached.

In Figs. 4(b) and 4(e) the diagrams for a variation of the rf-power of the source plasma is shown. The rf-power has an influence on the ion density in the anodic plasma. The ion density rises with increasing rf-power. At low power (1 W) two peaks can be seen, which are not of the same intensity, but no dust-free region is measured. By increasing the rf-power these peaks tend to separate and a torus is formed. At low rf-power this torus is asymmetric and the amplitude in the left branch is larger than in the right branch. For higher rf-power the torus becomes nearly symmetric. Two additional peaks, marked with a dashed line, appear, representing a secondary inner torus, which consists of much finer particles that originate from sputtering of the melamine particles. This torus has typically a smaller diameter and is located between the anode and the primary torus of monodisperse particles. For the analysis of the inner diameter and the z-position we neglect the secondary torus at high rf-power. In Fig. 4(e) the inner diameter (circles) and the axial distance (triangles) of the torus towards the anode are plotted versus the rf-powerr. The inner diameter increases with increasing rf-power and the axial distance decreases until a constant value of approximately 18 mm is reached.

In Figs. 4(c) and 4(f) the diagrams for a variation of the anode voltage are shown. As for the rf-power variation, smaller particles are seen, because this measurement was performed after the rf-power variation. It should be noted that with increasing anode voltage also dust particles in the vicinity of the anodic plasma can be attracted and confined during a measurement. At low anode voltage (51 V) no torus is observed. Only a displaced cloud appears, which later becomes the left branch of the torus. By increasing the anode voltage a torus is formed with nearly symmetric branches. The dashed peaks indicate the location of the secondary torus, which is located between the anode disk and the primary torus. But in contrast to the secondary torus found during the rf-power variation, which was residing between the primary torus branches with a smaller torus diameter, rather the present secondary torus has a diameter of the order of the primary torus diameter and is located at the same x position. The diameter of the primary torus increases with rising anode voltage until a value of $d \approx 12$ mm. The distance from the anode is reduced until a value of about 24 mm is reached.

B. Dust rotation in tori

In our observation geometry, only the horizontal component of the particle velocity can be measured. We have analyzed the mean particle velocity by particle image velocimetry (PIV) (Ref. 26) in a top section and in a bottom section of the torus [see insets of Fig. 5(a) and 5(b)]. One measurement was defined over 50 samples of a PIV-measurement and these measurements were averaged over 20. The results

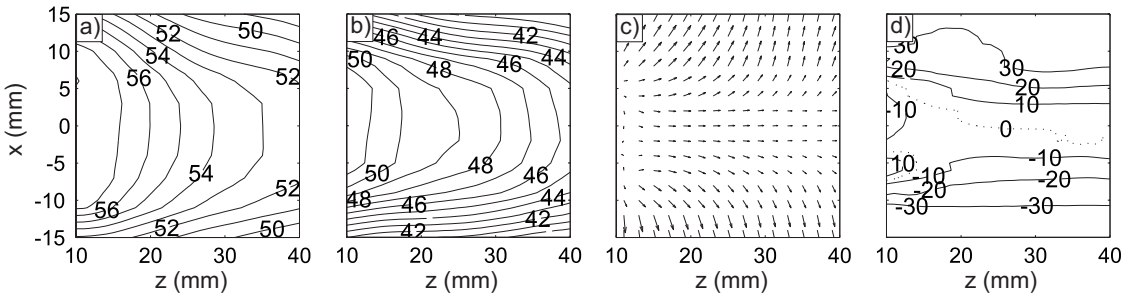

FIG. 7. The two-dimensional plasma potential profiles given in Volt for (a) low magnetic field, $B=20$ mT and (b) high magnetic field, $B=50$ mT. The magnetic field points in the direction of the anode disk. (c) Calculated ion velocity and (d) the azimuthal component of the ion velocity at low magnetic field.

are shown in Figs. 5(a) and 5(b) for the top and bottom section, respectively. The image axes are scaled in millimeters, but have an offset from the anode coordinate system. For a rotation of the particles about the torus, we expect that the sign of the particle velocity changes. Figure 5 shows that in the upper part it is positive and in the lower part it is negative. In the top section, a velocity gradient is observed. Figure 5(c) shows a vertical section through the velocity profile of the top section. The velocity increases in the x-direction until the edge of the dust cloud is reached. Such a velocity gradient is not seen in the bottom section of the torus. Figure 5(d) shows the velocity along the indicated line through the cloud. The velocity profile has a parabolic shape with a negative extremum of the velocity.

In Fig. 6 the velocity is shown for varying magnetic field at different pressures of 5.8 Pa (circles), 6.3 Pa (crosses), and 7.9 Pa (diamonds). In order to confirm the results from the PIV method, the velocity was determined with a particle tracking algorithm.[27] The averaged velocity obtained from a pair of frames is defined as one measurement. The resulting mean velocity is then determined as the average of about 1000 measurements. The displayed data points cover the region where a torus is formed. Except for lower magnetic field values of 20 mT at the pressure of 7.9 Pa, the torus has existed, but the velocity could not be measured. The velocities of the particles are found larger at higher gas pressures. All three measurements show that with increasing magnetic field the velocity of the particles is decreased. This decrease is counterintuitive, because the azimuthal component of the ion drag should increase with the magnetic field. Ion density measurements with a Langmuir probe, however, have shown that the plasma density decreases with increasing magnetic field. For this reason, a variation of the magnetic field has a non-negligible influence on the plasma production in the anodic plasma.

IV. MEASUREMENT OF THE PLASMA POTENTIAL AND CALCULATION OF THE ION DRAG FORCE

A. Plasma potential

In order to understand the behavior of the dust clouds, it is necessary to measure the plasma parameters and to determine the forces which are acting on a dust particle. Therefore a two-dimensional scan of the plasma potential was performed with an emissive probe that is axially movable (z) and horizontal rotatable (φ). We assume that the anode potential contours have a rotational symmetry about the z-axis and convert the φ-z coordinates to x-z coordinates.

In Figs. 7(a) and 7(b) two measurements of the plasma potential are shown for different magnetic field strengths $B=20$ mT and 50 mT, respectively. The plasma potential is given in Volt and the magnetic field points in the direction towards the anode disk. The plasma potential has a nearly symmetric shape about the midsection $x=0$ mm. The contours are convex curved and elongated. If the magnetic field is increased the structure of the potential changes significantly. The potential is decreased and the contour becomes narrower and more elongated. The radial electric field increases as can been seen from the higher density of contour lines.

B. Modelling the ion drag

1. Ion velocity

With the emissive probe a two-dimensional data set of the plasma potential in the x-z plane was obtained. For rotational symmetry $\vec{E}=-\nabla\Phi$ lies in the x-z plane and it is possible to determine the electric field vector inside the anodic plasma. The azimuthal component of the electric field is $E_y=0$. The stationary equation of motion for the ions reads

$$m_i\nu_{in}\vec{v}_f = e(\vec{E}+\vec{v}_f\times\vec{B}), \tag{1}$$

ν_{in} being the ion-neutral collision frequency, m_i the ion mass, and $\vec{v}_f$ the ion drift velocity, $\vec{E}=(E_x,0,E_z)$ and $\vec{B}=(0,0,B)$. This yields for the drift velocity

$$\vec{v}_f = \begin{pmatrix} \frac{1}{1+\mu^2B^2} & \frac{\mu B}{1+\mu^2B^2} & 0 \\ -\frac{\mu B}{1+\mu^2B^2} & \frac{1}{1+\mu^2B^2} & 0 \\ 0 & 0 & 1 \end{pmatrix} \mu\vec{E}. \tag{2}$$

$\mu=e/m_i\nu_{in}$ is the mobility of the ions. Frost[28] found the mobility of argon ions in their parent gas as $\mu(E,p)=\mu_0 p_0/p\cdot(1+AE/p)^{-1/2}$, with $\mu_0=0.146$ m^2/V s, $p_0=133$ Pa, and $A=0.035$ Pa m/V.

The ion velocity components are shown for the potential structure of the low magnetic field [Fig. 7(a)] in Figs. 7(c) and 7(d), (c) showing the radial and axial velocity components in the x-z plane. The ions follow mainly the electric

field, the magnetic field forces them to describe a curved trajectory, giving rise to a small azimuthal component of ion drift velocity of a few percent of the drift velocity. In Fig. 7(d) the azimuthal velocity component $v_{i,\varphi}$ is shown. It is obvious that the sign of the velocity changes between the upper half ($x>0$) and the lower half ($x<0$).

Due to the drift motion of the ions their temperature is elevated above the neutral gas temperature T_n (Refs. 22 and 29) (k_B being the Boltzmann constant)

$$T_i(v_f) = T_n + \frac{\pi-2}{6}\frac{1}{k_B}m_i v_f^2. \tag{3}$$

2. Ion drag force

There are many models that estimate the ion drag force on a spherical particle.[6–9] Hutchinson[6] by means of simulations showed that most of the analytic expressions underestimate the ion drag. Therefore, he proposed an effective ion velocity which gives a good agreement between simulations and an analytic expression. We follow his calculations for the ion drag force for singly charged ions.

The ion drag force consists of a collection part by direct momentum transfer of ions hitting the dust particle (F_c), and an orbital part from scattered ions (F_o). The orbital motion limited (OML) collection force is given for a shifted Maxwellian distribution with flow velocity v_f in terms of $u=v_f/v_{ti}$, normalized to the ion thermal velocity $v_{ti}=\sqrt{2k_BT_i/m_i}$,

$$F_c = n_i r_p^2 m_i v_{ti}^2 \frac{\sqrt{\pi}}{2u^2}\left\{ u(2u^2+1+2\chi)\mathrm{e}^{-u^2} + [4u^4+4u^2-1-2(1-2u^2)\chi]\frac{\sqrt{\pi}}{2}\mathrm{erf}(u)\right\} \tag{4}$$

with $\chi \equiv -e\phi_p/k_BT_i$ being the normalized potential of the particle. The orbit force reads as follows:

$$F_o = n_i \frac{q_i^2\phi_p^2}{m_i v_{ti}^2} r_p^2 8\pi G(u)\ln\Lambda, \tag{5}$$

where $G(u)\equiv[\mathrm{erf}(u)-2u\mathrm{e}^{-u^2}/\sqrt{\pi}]/(2u^2)$ is the Chandrasekhar function,[30] q_i is the ion charge, r_p is the particle radius, and $\ln\Lambda$ is the Coulomb logarithm. The surface potential ϕ_p is estimated using the floating condition for a dust grain in the OML approximation

$$\overline{\Gamma}_e(\phi_p) = \frac{1}{4}n_{e\infty}\left(\frac{8k_BT_e}{\pi m_e}\right)^{1/2}\exp(e\phi_p/k_BT_e) = n_{e\infty}v_{ti}\frac{u}{4}\left\{\left(1+\frac{1}{2u^2}+\frac{\chi}{u^2}\right)\mathrm{erf}(u)+\cdots + \frac{1}{u\sqrt{\pi}}\exp(-u^2)\right\} = \overline{\Gamma}_i. \tag{6}$$

For the Coulomb logarithm $\ln\Lambda$ the expression from Khrapak *et al.*[7] is used: $\ln\Lambda=\ln[(b_{90}+\lambda_s)/(b_{90}+r_p)]$, where $b_{90}=r_pe\phi_p/m_iv_{\mathrm{eff}}^2$ is the 90° scattering impact parameter for Coulomb collisions and $\lambda_s^2=\lambda_{\mathrm{De}}^2/[1+2k_BT_e/m_iv_{\mathrm{eff}}^2]+r_p^2$ the effective Debye length. Good agreement between this analytic expression and simulations was found if one takes the following expression for an effective drift velocity v_{eff}:[6]

$$m_iv_{\mathrm{eff}}^2 = 2k_BT_i + m_iv_f^2\left\{1+\left[\frac{v_f/\sqrt{k_BT_e/m_i}}{0.6+0.05\ln(M)+(\lambda_{De}/5r_p)(\sqrt{k_BT_i/k_BT_e}-0.1)}\right]^3\right\}, \tag{7}$$

M being the ion mass in units of hydrogen mass. Using Eqs. (2)–(7) we have calculated the ion drag force along the drift direction of the ions at every point in the area of interest. Splitting the drag force into their components along the coordinate axes and assuming rotational symmetry, it is possible to obtain the three-dimensional ion drag force. Using the capacitance model for the dust grains charge $q_d=4\pi\epsilon_0r_p\phi_p$, the electric field force $\vec{F}_{\mathrm{el}}=q_d\vec{E}$ is also obtained.

The confinement in the axial and radial direction is maintained by the balance of the radial and axial component of the ion drag force and the electric field force. For a detailed discussion of the axial confinement, see Ref. 22.

In Fig. 8 the total electric field force (circles) and the total ion drag force along the electric field line for different ion densities of $n_i=4\times10^{14}$ m^{-3} (squares), 6×10^{14} m^{-3} (diamonds), and 8×10^{14} m^{-3} (triangles) are plotted versus x at $z=25$ mm. The intersection of the ion drag and the electric field force defines an equilibrium position where the dust can be confined. The ion drag force increases with rising ion density. But the position of the force equilibrium does not change that much, because of the strong gradient of the electric field force. In the midsection of the anode the ion drag force exceeds the electric field force and pushes the particles out of the central region. If the ion density would be smaller, the electric field force exceeds the ion drag force and no dust would be confined at an axial position of $z=25$ mm.

Due to the assumption of rotational symmetry of the anodic plasma, no azimuthal component of the electric field is present. However, an azimuthal part of the ion drag force results from the off-diagonal part of the ion drift velocity. This azimuthal component of the ion drag has to be balanced against the azimuthal part of the gravitational force and neutral friction. As long as $F_{i,\varphi}$ does not exceed

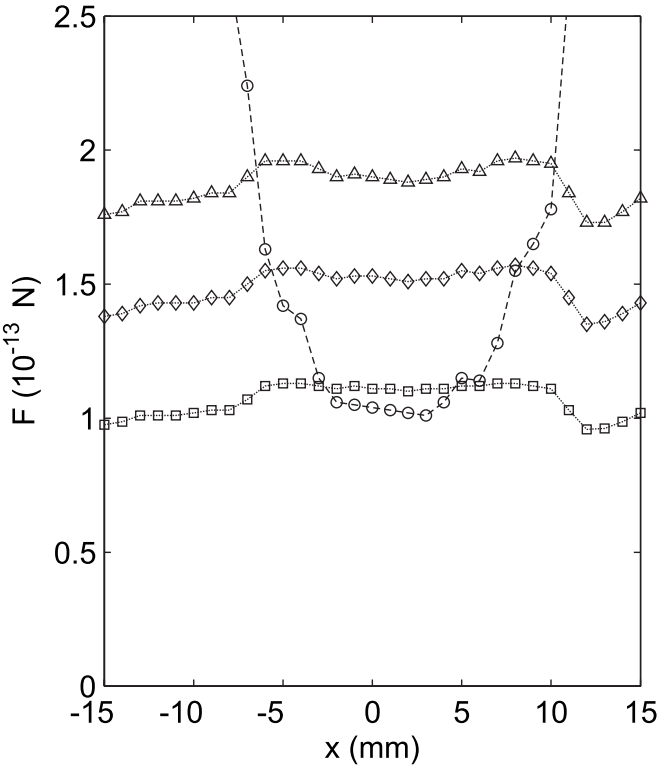

FIG. 8. Total electric field force (circles) and total ion drag force along the electric field line for different ion densities of $n_i=4\times10^{14}$ m^{-3} (squares), 6×10^{14} m^{-3} (diamonds), and 8×10^{14} m^{-3} (triangles) are plotted vs x at $z=25$ mm.

$F_g=0.6\times10^{-14}$ N, no rotation of the dust particles about the axis is possible and hence the cloud shape of 2 (a) is observed. If now $F_{i,\varphi}>F_g$ rotation is possible and the torus-shaped dust cloud 2 (b) results.

To get an estimate of the dust rotation velocity, we assume that $F_{i,\varphi}-F_{g,\varphi}+F_n=0$, i.e., the excess of $F_{i,\varphi}$ over $F_{g,\varphi}$ is balanced by neutral friction, $F_n=-m_d\beta v_\varphi$, with v_φ the rotation velocity. $\beta=\delta(8/\pi)p(r_p\rho_p v_{\mathrm{th},n})^{-1}$ is the Epstein coefficient[31] with p the pressure, ρ_p the mass density of the particles, $v_{\mathrm{th},n}$ the thermal velocity of the neutrals, and δ a parameter in the order of unity. Typical values of $F_{i,\varphi}$ are 0.8×10^{-14} N, which give a rotational velocity of $v_\varphi\approx200$ mm s^{-1}. Compared to the velocity measured in the experiment it is of the same order, but a factor of about 3 larger.

V. DISCUSSION

In this paper we have studied the existence regime, the shape and the rotation of toroidal dust clouds in a magnetized plasma. With increasing magnetic field strength, we have found a transition from a radially displaced dust cloud to a torus. The dust particles perform a rotational motion about the torus axis in the $E\times B$ direction of the ions.

We conclude that the central void in the torus is created by the same mechanism that generates the voids in unmagnetized rf-discharges, i.e., in the center, the ion motion is predominantly radial and the ion speed is low. Therefore, the ion drag force becomes stronger than the opposing electric field force. The net force then removes the dust particles from the central region. The position of the force equilibrium (Fig. 8), which determines the void edge, is found at $x\approx7$ mm for a typical density in our experiment of $n_i=6\times10^{14}$ m^{-3}. The observed void radius in Fig. 2 is in reasonable agreement with this equilibrium point. Hence, the zero-order equilibrium of the dust particles is determined by the radial and axial forces. This observation confirms our earlier conclusion in Ref. 24 that the displacement of small dust clouds from the center of the anodic plasma is caused by the ion drag force.

The weight force of the small dust particles is only a few percent of the radial electric field force. Therefore, dust particles can be set into rotation about the torus axis by similar weak forces. One of these weaker forces is the azimuthal component of the ion drag force. A balance of these two forces is already achieved at a weak magnetic field of 10 mT. Below this threshold, no torus is formed, above the threshold a torus is formed and becomes increasingly symmetric, as shown in Figs. 2(a) and 2(b).

The observed streaming velocities of the dust particles in the upper part of the torus show a velocity gradient, which is consistent with a simplified picture of adding the azimuthal components of weight force and ion drag force, which eventually are balanced by friction with the neutral gas, which is assumed to be at rest. The radial part of the weight force slightly shifts the zero-order radial equilibrium. On the side where the dust rises, the speed is low, whereas, on the falling side ion drag and weight force add up and give an increased speed. However, this simplified single-particle model is still incomplete, because it cannot explain the almost constant velocity in the bottom part of the torus and would predict a very high speed on the side where the dust descends. One of the weaker forces, which we have neglected is the electrostatic repulsion between dust grains, which becomes important in denser parts of the torus. Such an electrostatic pressure force would introduce nonlocal aspects into the force balance. However, an increase of the dust speed on the descending branch, which would result from the single-particle model, manifests itself indirectly by a reduced cross section of the torus.

An influence of a neutral drag caused by motion of the background gas was neglected so far. This can be justified, on the one hand, by the construction of the gas-feed and vacuum system. The gas inlet and vacuum pump are mounted on the same port at the end of the vacuum vessel. Therefore, any directed gas flow is prevented and argon gas enters only by diffusion. Observing the behavior of small dust grains at weak magnetic field showed that effects from neutral gas motion are negligible. Further, the symmetry of the dust rotation under reversal of the magnetic field rules out rotational gas flows of this kind. On the other hand, gas rotation from an azimuthal ion velocity which is effected through ion-neutral collisions cannot be excluded *a priori*.[20] If such a gas rotation would contribute to the observed rotation of dust particles about the torus axis, the threshold for the onset of rotation would be lowered, because neutral drag and ion drag force would act in the same direction. The relative contribution of ion drag and neutral drag, however, can only be deduced from a global model of ion and gas

motion, which is not available yet. However, since our analysis of the forces in Sec. IV gives a proper estimate for the onset of dust rotation, we conclude that ion drag is more important than neutral drag for the observed dust particle rotation.

The dependence of the torus shape and rotation on the discharge parameters can be generally explained by the influence of the discharge parameters on the ion density and ion drag force, respectively. The ion density increases with rf-power or discharge current and decreases with magnetic field strength (approximately $B > 15$ mT). We had found that the torus-shaped dust cloud exists for an intermediate region of the discharge parameters. The torus collapse at high magnetic fields is caused by a reduction in plasma density, which leads to a stronger reduction of the azimuthal ion-drag force than the gain from the increasing tilt of the ion-drag force towards the azimuthal direction. At low magnetic field the torus collapses, because of a weak confinement potential and a low azimuthal ion drag force component. The influence of the rf-power and the anode voltage on the anodic plasma production is similar, with increasing parameter the ion density rises.

In summary, the presented investigations give a comprehensive picture of toroidal dust clouds and the formation of voids in magnetized dusty plasmas.

ACKNOWLEDGMENTS

Fruitful discussions with D. Block, F. Greiner, and T. Trottenberg are gratefully acknowledged.

The present investigations were financially supported by DFG within the transregional collaborative research center TR-24, project A2.

[1] G. E. Morfill, H. M. Thomas, U. Konopka, H. Rothermel, M. Zuzic, A. Ivlev, and J. Goree, Phys. Rev. Lett. **83**, 1598 (1999).
[2] M. Klindworth, O. Arp, and A. Piel, J. Phys. D **39**, 1095 (2006).
[3] G. Praburam and J. Goree, Phys. Plasmas **3**, 1212 (1996).
[4] J. Goree, G. E. Morfill, V. N. Tsytovich, and S. V. Vladimirov, Phys. Rev. E **59**, 7055 (1999).
[5] D. Samsonov and J. Goree, Phys. Rev. E **59**, 1047 (1999).
[6] I. H. Hutchinson, Plasma Phys. Controlled Fusion **48**, 185 (2006).
[7] S. A. Khrapak, A. V. Ivlev, G. E. Morfill, and H. M. Thomas, Phys. Rev. E **66**, 046414 (2002).
[8] M. S. Barnes, J. H. Keller, J. C. Forster, J. A. O'Neill, and D. K. Coultas, Phys. Rev. Lett. **68**, 313 (1992).
[9] S. A. Khrapak, A. Ivlev, S. K. Zhdanov, and G. E. Morfill, Phys. Plasmas **12**, 042308 (2005).
[10] M. R. Akdim and W. J. Goedheer, Phys. Rev. E **65**, 015401 (2002).
[11] M. R. Akdim and W. J. Goedheer, Phys. Rev. E **67**, 056405 (2003).
[12] V. Land, W. J. Goedheer, and M. R. Akdim, Phys. Rev. E **72**, 046403 (2005).
[13] V. Land and W. J. Goedheer, New J. Phys. **8**, 8 (2006).
[14] M. Klindworth, A. Piel, A. Melzer, U. Konopka, H. Rothermel, K. Tarantik, and G. Morfill, Phys. Rev. Lett. **93**, 195002 (2004).
[15] E. Thomas, K. Avinash, and R. L. Merlino, Phys. Plasmas **11**, 1770 (2004).
[16] R. P. Dahiya, G. V. Paeva, W. W. Stoffels, E. Stoffels, G. M. W. Kroesen, K. Avinash, and A. Bhatacharjee, Phys. Rev. Lett. **89**, 125001 (2002).
[17] Y. Zhang, X. Wang, and J. Liu, Phys. Rev. E **78**, 016405 (2008).
[18] U. Konopka, D. Samsonov, A. V. Ivlev, J. Goree, V. Steinberg, and G. E. Morfill, Phys. Rev. E **61**, 1890 (2000).
[19] L. J. Hou and Y. N. Wang, Phys. Plasmas **12**, 042104 (2005).
[20] J. Carstensen, F. Greiner, L. Hou, H. Maurer, and A. Piel, "Influence of neutral gas motion on the rotation of dust clusters in an axial magnetic field," Phys. Plasmas (submitted).
[21] A. Barkan and R. L. Merlino, Phys. Plasmas **2**, 3261 (1995).
[22] T. Trottenberg, D. Block, and A. Piel, Phys. Plasmas **13**, 042105 (2006).
[23] E. Thomas and M. Watson, Phys. Plasmas **6**, 4111 (1999).
[24] I. Pilch, T. Trottenberg, A. Piel, and M. E. Koepke, Phys. Plasmas **14**, 123704 (2007).
[25] MATLAB, The MathWorks, Inc., 3 Apple Hill Drive, Natick, MA 01760–2098 USA, http://www.mathworks.com/.
[26] J. K. Sveen, "An introduction to matpiv v.1.6.1," Eprint No. 2, ISSN, 0809–4403, Department of Mathematics, University of Oslo (2004), http://www.math.uio.no/~jks/matpiv.
[27] O. Arp, private communication (2008), arp@physik.uni-kiel.de.
[28] L. S. Frost, Phys. Rev. **105**, 354 (1957).
[29] S. Robertson and Z. Sternovsky, Phys. Rev. E **67**, 046405 (2003).
[30] S. Chandrasekhar, Astrophys. J. **97**, 255 (1943).
[31] P. S. Epstein, Phys. Rev. **23**, 710 (1924).

B.3

SYNCHRONIZATION OF DUST DENSITY WAVES IN ANODIC PLASMAS

I. Pilch, T. Reichstein, and A. Piel

Reprinted with permission from
I. Pilch, T. Reichstein, and A. Piel,
Physics of Plasmas, Vol. 16, Page 123709 (2009).

Synchronization of dust density waves in anodic plasmas

Iris Pilch,[a] Torben Reichstein, and Alexander Piel
Institut für Experimentelle und Angewandte Physik, Christian-Albrechts-Universität, D-24098 Kiel, Germany

(Received 29 September 2009; accepted 2 November 2009; published online 31 December 2009)

Dust clouds can be confined in anodic plasmas by an equilibrium of the electric field force and the ion drag force. In these dust clouds self-excited dust density waves are observed as soon as the cloud length exceeds typical wavelengths. By superimposing an external modulation signal on the anode bias, the self-excited wave can be synchronized at the modulation frequency when the frequency is close to the natural frequency of the self-excited wave. For very low frequencies, an interaction of the center of mass motion of the cloud with the self-excited wave is found. For intermediate frequencies, close to the natural frequency of the self-excited modes, entrainment is observed, and for slightly higher frequencies a spatial cascade to subharmonic modes is found. At the highest frequencies, an influence of the modulation is still present, the wave is entrained if the modulation frequency is close to a rational factor of the natural frequency, as can be seen by the narrowing of the spectral components. © *2009 American Institute of Physics*. [doi:10.1063/1.3274928]

I. INTRODUCTION

A dusty (complex) plasma consisting of ions, electrons, and macroscopic dust particles can be confined in anodic dc discharges[1] by an equilibrium of ion drag force and electric field force.[2,3] In these dust clouds dust acoustic waves[4] or rather self-excited dust density waves appear due to streaming ions.[5] Besides their dynamical aspects these waves are also of interest for measuring the particle charge, which depends on the plasma parameters, e.g., electron temperature and ion mass. The particle charge can be estimated by determining the onset of the wave instability[6,7] or by measuring the dispersion properties[8] for the particular situation.

The present models of dust density waves range from a simple fluid theory[4] to a kinetic theory[5] including several effects like a variable particle charge or finite size. For comparing the experiments with the known theoretical approaches, and thus to distinguish which assumption is valid, the linear dispersion relation is commonly measured. This can be done by varying the external discharge parameters (e.g., anode current, rf power) and by simultaneously analyzing the effect on the self-excited wave.[9] The disadvantage of this method is that the plasma parameters (e.g., electron density) have to be accurately known for a normalization of the measurements. A better and more suitable method is to modulate the discharge current, thus driving the self-excited wave at the modulation frequency. This method is independent of the discharge parameters, but requires that the plasma is only little disturbed by the modulation signal.

The synchronization of dust acoustic waves was first introduced by Thompson *et al.*,[10] who found an agreement of the observed wave dispersion with the dust acoustic wave theory[4] over a region of (5–40) Hz. A comparison with the kinetic theory was performed by Trottenberg *et al.*[2] over a frequency range of (16–40) Hz. There, a reduction in the wavelength in direction of the wave propagation was also observed. Recently, Thomas, Jr., *et al.*[11] and Williams *et al.*[12] analyzed the response of a self-excited wave to modulation signals at high frequencies above 100 Hz. It was found that the dispersion cannot be described by the previously used theories. This was attributed to a modification of the dispersion by a finite kinetic temperature of the dust particles that was neglected before. A recent model by Rosenberg *et al.*[13] includes these temperature effects and finds good agreement with the measured data.

Nevertheless, the mechanism responsible for the synchronization of the self-excited wave in the present situation is still an open issue although it was studied in other plasma systems.[14,15] The nature of the dust density wave is complex because it is an extended three-dimensional oscillatory system with varying growth and damping rates. Therefore, it is interesting to study the nonlinear dynamics that are excited by the external modulation. One of the interesting aspects is sub- and superharmonic entrainment of the self-excited waves.

The established synchronization models range from the simple resonance of a driven harmonic oscillator over parametric excitation and circle map to the van der Pol oscillator, which includes nonlinear damping. An introduction to these dynamical aspects can be found in numerous textbooks.[15–18] The van der Pol oscillator was extensively studied in laser physics[19] where it describes injection locking. Alternatively, in laser physics, injection seeding is also analyzed, where a coherent external signal competes with noise. The laser medium amplifies the modulation signal until it becomes the strongest growing mode.

Concerning the synchronization of dust density waves, only few theoretical approaches were made. A theory including a parametric excitation due to a periodical modulation of the dust charge was proposed by Yaroshenko and Morfill.[20] Mathieu's equation was derived from a fluid model including charge variation. It was mentioned that a reduction of a fluid model to Mathieu's equation is possible for any kind of pe-

[a]Electronic mail: pilch@physik.uni-kiel.de.

riodical modulation, in particular density fluctuations of ions and electrons. On the experimental side, Pramanik *et al.*[21] studied wave turbulence in dependence of the neutral gas pressure. They found that the wave becomes more incoherent at low gas pressures.

In the present paper, we describe the influence of an external modulation on the self-excited dust density wave over a wide frequency range of $f=(1-140)$ Hz. We previously found[22] that the modulation signal at low frequencies ($f<15$ Hz) leads to a sloshing and stretching motion of the entire dust cloud for small clouds ($\lambda \geq L$, wavelength λ and cloud length L). The sloshing motion is the movement of the center of mass and the stretching the deformation of the cloud shape. In medium-sized ($\lambda < L$) and large clouds ($\lambda \ll L$) self-excited waves occur. These waves could be synchronized over an estimated frequency range of about $f \approx (18-40)$ Hz. Hence, it was concluded that the sloshing motion is only present for low frequencies and therefore no interference with the wave propagation at higher frequencies was expected. Now, we analyze the spatial frequency distribution in a large dust cloud and discuss the influence of a sloshing motion at low frequencies on the propagation of the self-excited dust density wave. Furthermore, the entrainment regime close to frequencies of the self-excited wave is studied. Finally, the influence of a modulation at high frequencies with respect to the frequency of the self-excited wave is analyzed. In the following, we will use the terms synchronization and entrainment synonymously.

II. EXPERIMENTAL SETUP

The experiment consists of a primary source plasma generated by a radio-frequency discharge ($f=27.12$ MHz) at low power of 1 W. The dust is confined in a secondary anodic plasma which builds up in front of a positively biased disk-shaped anode. A detailed description of the experiment was given in Refs. 2 and 22. A sketch of the anodic plasma is shown in Fig. 1. The anode is operated at a bias of $\bar{U}_a = +60$ V with reference to the grounded discharge vessel and low currents of about $I_a \approx 7$ mA. For the modulation of the dust clouds a sinusoidal signal of $\delta U_a = 10$ V_{pp} can be superimposed. The experiments are performed in argon gas at a pressure of 3 Pa. The magnetic field has a strength of about 20 mT. Typical plasma parameters are density $n_e \approx 10^{15}$ m^{-3} and electron temperature $T_e \approx 3$ eV.

The dust particles (melamine formaldehyde) used during the experiments are spherical and monodisperse with a diameter of (0.97 ± 0.05) μm. The dust is confined in the anodic plasma by a force balance of the electric field force and the ion drag force. The axial confinement of dust clouds in front of an anode disk was studied in detail by Trottenberg *et al.*[2]

The observation geometry is shown in Fig. 1. The dust cloud is illuminated by a horizontal laser fan ($\lambda = 532$ nm, 200 mW), and the scattered light is recorded at right angle by a camera viewing from the top. The camera is a charge coupled device camera with a frame rate of 302 fps by selecting a region of interest (ROI). Camera and laser fan are mounted together on a translation stage and can be vertically positioned to image any horizontal section of the dust cloud. For recording the dust density waves, a fixed horizontal section of the dust cloud was chosen.

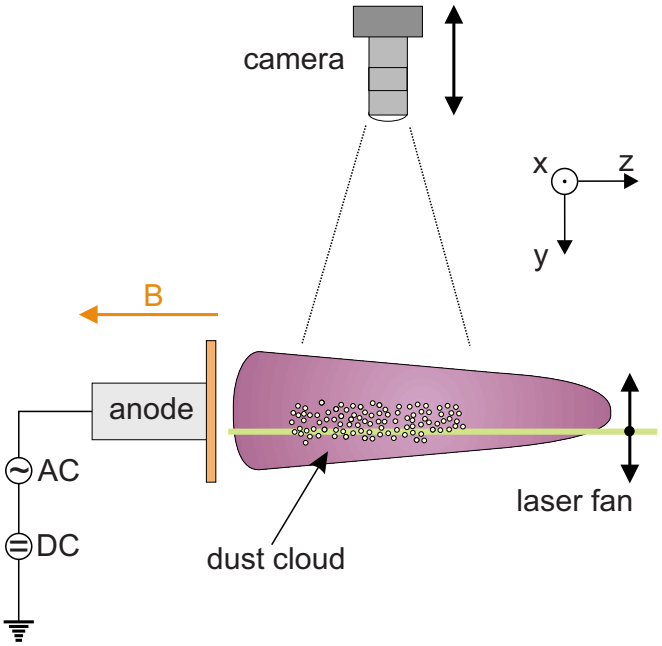

FIG. 1. (Color online) A dust cloud is confined in the anodic plasma and is observed with a combination of a horizontal laser sheet and a camera, which can be positioned at any vertical position.

III. SELF-EXCITED DUST DENSITY WAVE

Dust clouds exhibit self-excited waves when the cloud size exceeds the typical wavelength. A snapshot of the observed self-excited wave is displayed in Fig. 2(a), the pixel intensity is inverted, and the contrast is enhanced. The horizontal lines mark the ROI, which is chosen to analyze the dynamics of the dust density wave.

In this region of about 1.6 mm width, it can be assumed that the wave front is sufficiently straight along the x-axis. The z-axis defines the propagation direction of the wave. The intensity profile $I_m(z,t)$, which is assumed to be proportional to the dust density distribution, is then estimated by averaging along the x-axis over the pixel intensity $I(x,z,t)$ at position z and time t. The averaging region is defined by the boundary of the ROI (pixel x_1 and x_2),

$$I_m(z,t) = \frac{1}{(x_2 - x_1)} \sum_{x=x_1}^{x_2} I(x,z,t).$$

This ensures that the profile is smoother and less affected by particle granulation. The time-averaged intensity profile $\langle I_m(z) \rangle$ is calculated by averaging over the entire time series

$$\langle I_m(z) \rangle = \frac{1}{N} \sum_{t=1}^{N} I_m(z,t).$$

In Fig. 2(b) the intensity profile $I_m(z,t)$ at a given time step t and the time-averaged intensity profile $\langle I_m(z) \rangle$ are shown with a solid and a dashed line, respectively. For comparison, the same snapshot is chosen as in Fig. 2(a).

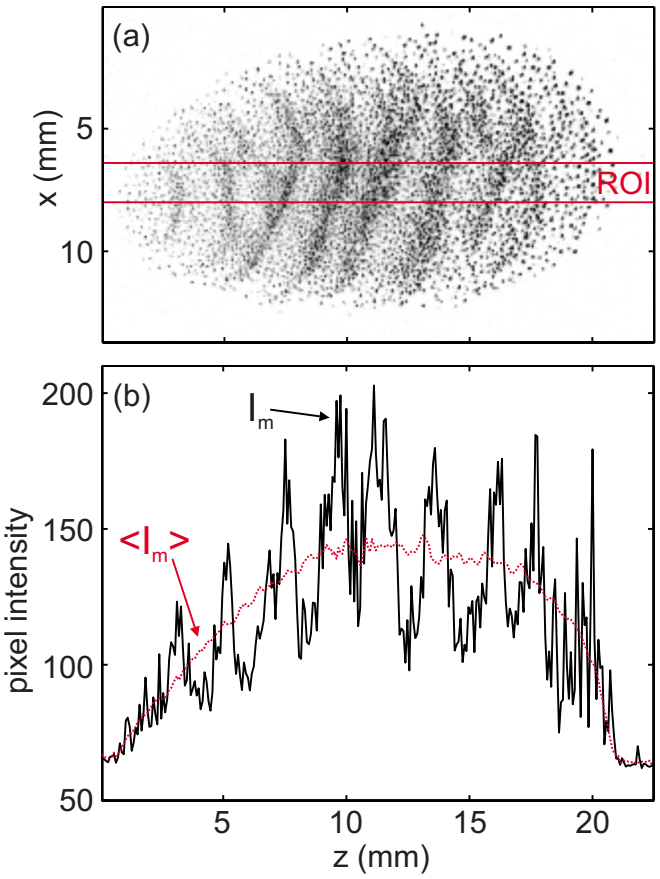

FIG. 2. (Color online) (a) A snapshot of the self-excited wave (inverted color). The gray (red online) lines mark the ROI, which is analyzed. (b) The intensity profile (black line) averaged along the x-axis in the ROI and the time-averaged intensity profile (red dashed line) are displayed.

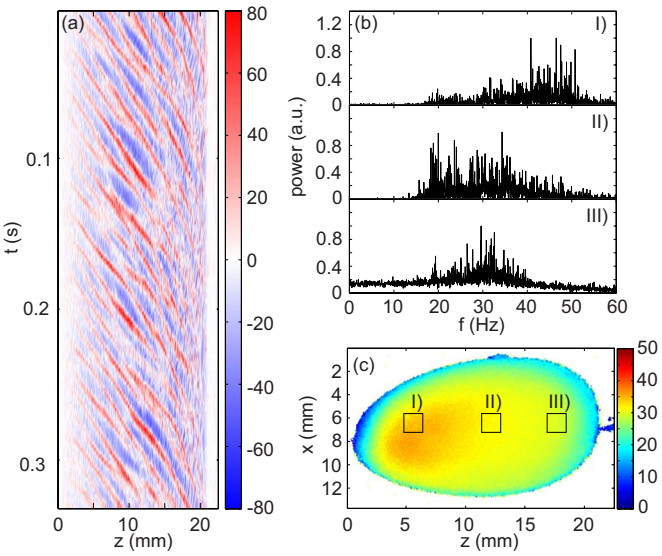

FIG. 3. (Color online) Shown are (a) the space-time diagram of the dust density fluctuations. The colormap of the space-time diagram is given in pixel intensity of the dust density fluctuations. (b) Power spectra, spatially averaged over the indicated square regions in (c) and labeled there with Roman numerals. The spectra are normalized to the highest spectral component. (c) The mean frequency distribution; the colorbar is given in units of hertz.

The cloud has a length of $L \approx 19$ mm, and the wavelength of the self-excited wave is approximately $\lambda \approx (2-3)$ mm; thus, according to our previous definition, we classify this cloud as large. The wave fronts are visible as narrow dark regions in the snapshot where the dust density is increased. The modulation degree of the dust density wave is $M=(I_{\max}-I_{\min})/(I_{\max}+I_{\min})=(0.11-0.25)$. The wave fronts appear narrower than the troughs, introducing some anharmonicity.

In order to study the dynamics of the dust density wave, the dust density fluctuations $\tilde{n}_d(z,t)$ are calculated by subtracting the time-averaged intensity profile $[\langle n_d(z)\rangle \propto \langle I_m(z)\rangle]$ from the intensity profile for each time step $[n_d(z,t) \propto I_m(z,t)]$,

$$\tilde{n}_d(z,t) = I_m(z,t) - \langle I_m(z)\rangle.$$

Finally, these fluctuations are composed to a two-dimensional map, where the time evolution is displayed over the z-axis, which is the propagation direction of the wave. This representation is referred to as space-time diagram, and the used colormap in this article is given in pixel intensity of the dust density fluctuations.

The space-time diagram is shown in Fig. 3(a). By tracking single wave fronts in the space-time diagram a variation of the slope is observed. For a regularly propagating wave, a constant frequency and wavelength would be expected. In the space-time diagram the wave fronts would appear slanted forming a set of parallels. In fact, the inclination of the wave fronts in the space-time diagram is not constant and varies in the z-direction, forming complex patterns.

For a quantitative measure of the phase velocity of the wave, the spatial shift between the wave fronts of consecutive intensity profiles was determined. This shift was obtained from the maximum of a cross-correlation function.[23] In the representation of the space-time diagram, the phase velocity is then $v_\varphi = dz/dt$. Hence, the varying slope of the trajectories of a maximum indicates the variability of the instantaneous phase velocity. Nevertheless, it is possible to estimate an averaged phase velocity of the wave $v_{\varphi,m} = (75 \pm 5)$ mm s^{-1}.

Furthermore, it is found that the wavelength is not constant over the entire cloud length. This observation is attributed to the propagating wave fronts with different phase velocities. For the same reason, a merging of wave fronts occurs. This wave-front merging develops without a periodicity and a faster propagating wave front overtakes a slower one.

The frequency spectrum of the wave is obtained by a fast Fourier transformation (FFT) algorithm.[23] In Fig. 3(b) averaged spectra over a square region are displayed. The position of the regions is indicated in Fig. 3(c) and labeled with Roman numerals. For a better representation, the spectra are normalized by their largest component, so that a comparison of spectral intensities between the shown spectra is not possible. All three spectra show no dominant spectral component but a noisy distribution. However, a shift from higher to lower mean frequencies from the anode-facing side (left) to the far side (right) is observed.

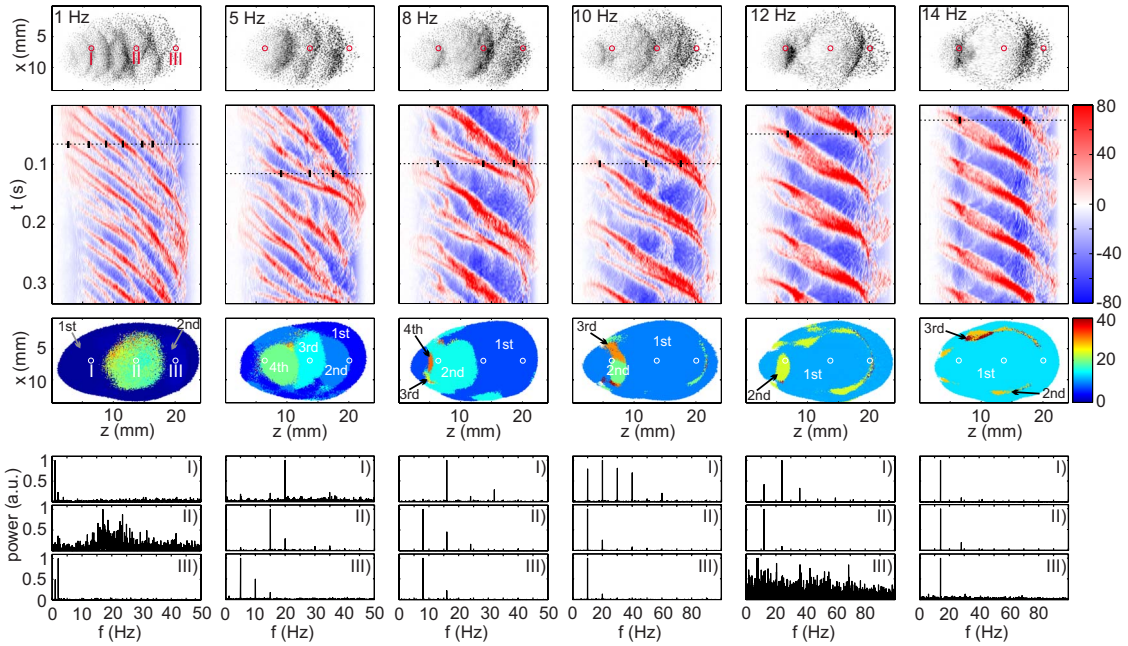

FIG. 4. (Color online) Response of the cloud on different modulation frequencies (from left to right: 1, 5, 8, 10, 12, and 14 Hz). Displayed are in columns the raw images, the space-time diagrams, the frequency distribution of the dominant component and the corresponding spectra at positions marked with open circles and labeled with Roman numerals at 1 Hz. The labels 1st, 2nd, 3rd, and 4th refer to the regions of the first, second, third, and fourth harmonic.

For obtaining a spatial two-dimensional diagram of the typical frequency at each position, a FFT of the time series was calculated for each pixel position. The mean frequency $\bar{f}$ is the weighted spectral intensity,[24]

$$\bar{f} = \frac{\int P(f')f'df'}{\int P(f')df'},$$

with $P(f)$ being the spectral power density. This mean frequency was calculated for every pixel position and used to color code the pixel. We will call this representation frequency map.

The frequency map for the self-excited wave is shown in Fig. 3(c). Here, the observation of the frequency shift found in the spectra [Fig. 3(b)] is also identified. The boundary region of the dust cloud has a smaller frequency compared to the core region. At the anode-facing side, higher frequencies of about 40 Hz are found and a decay toward smaller frequencies of about 20 Hz at the far region on the right hand side is observed.

IV. LOW-FREQUENCY MODULATION: SLOSHING AND WAVE INTERACTION

In the previous section, the self-excited wave was studied. Now, a low frequency sinusoidal modulation is applied to the anode voltage and the response of the cloud is analyzed.

In Fig. 4, a representative selection of measurements at modulation frequencies of 1, 5, 8, 10, 12, and 14 Hz is compiled. In the first row, snapshots of the dust cloud are displayed to visualize the shape of the wave fronts. The wave dynamics can be studied in the space-time diagrams shown in the second row. In the third row, the frequency maps are compiled. Deviating from the frequency map of the self-excited wave in this representation, the dominant frequency is used instead of the mean frequency. Selected frequency spectra of a single pixel can be found in the bottom row. The position, where the spectra were calculated, is indicated by open circles in the previous plot and labeled with Roman numerals.

At an excitation frequency of 1 Hz, the shape of the wave fronts is similar to the shape of the self-excited wave fronts, but the wave fronts are sharper. The wave pattern, shown in the space-time diagram, has a similar structure as the self-excited wave pattern. Here, only a fraction of the period of the modulation signal is displayed. The sloshing motion is described in more detail below. The phase velocity of the wave is varying, as can be seen from the alternating slope of the wave fronts. A noisy core with a central frequency regime of $f \approx (18-25)$ Hz is found in the frequency map. These frequencies resemble those observed for the self-excited wave. This can be seen in more detail in spectrum (II). Here, a noisy and broad frequency distribution is found. This is a hint that the self-excited wave propagates in the core-region nearly independently of the modulation signal. On the anode-facing side, the dominant frequency component is found at 1 Hz and corresponds to the modulation frequency [spectrum (I)]. The frequency of the dominant component at the far side is twice the exciting frequency, see spectrum (III).

Different from that, even at a modulation frequency as low as 5 Hz, the wave is entrained at the modulation frequency, which can be seen by the sharp frequency components in the spectrum. The wave fronts are broader in shape and the dust density in the maxima is higher compared to the self-excited wave. The space-time diagram shows no regular wave propagation, which would be seen as a linear slope

over the entire cloud length in the space-time diagram. Instead, a varying pattern of merging wave fronts with alternating phase speed is found. Here, a faster wave front overtakes a slower and the wave fronts merge. The resulting wave front then propagates at the higher phase velocity. The structure of the varying wave pattern has a period of the external modulation. Thus, the self-excited wave is entrained by the modulation signal.

In the center regions, the two-dimensional frequency map shows dominant peaks of higher harmonics. The highest component is found at the anode-facing side and toward the far side the dominant harmonics are shifted to lower harmonics. This is in good agreement with the space-time diagram, because the wave merging reduces the number of wave fronts from the anode-facing side toward the far side, thus reducing the effective wave frequency. The occurrence of these higher harmonics hints at a subharmonic synchronization, where an oscillator is synchronized at higher harmonics of the external modulation signal. Here, it is found that the fourth harmonic (20 Hz) is of the order of the self-excited wave spectrum. At the boundary region of the cloud the fundamental frequency from the modulation is dominant.

For increasing frequencies, the self-excited wave becomes more entrained at the modulation frequency and the wave propagation becomes more regular, as can be seen in the space-time diagrams. One interesting observation is found at a modulation frequency of 10 Hz. Here, the space-time diagram shows faint wave fronts of weak intensity, which are reaching a stagnation point and then travel in the opposite direction until they merge with the consecutive wave fronts, e.g., from 14 mm at 0.1 s to 13 mm at 0.15 s. At close inspection, this is also found at 8 Hz at the cloud boundary of the far side. For higher frequencies, the wave fronts become more regular until at approximately 14 Hz the wave is completely entrained at the modulation frequency over the entire cloud.

A. Sloshing motion

For a more detailed analysis of the sloshing motion, the space-time diagrams for 1 and 2 Hz are shown in Figs. 5(a) and 5(c) over a time interval of 1 s. The center of mass motion (solid line) and the envelope of the cloud boundary (dotted lines) are marked in Figs. 5(a) and 5(c). This representation visualizes that on the anode-facing side a modulation of the cloud boundary at the excitation frequency and on the far-side edge a response of twice the modulation frequency was found. This is in agreement with the spectral components shown in Fig. 4 spectra (I) and (III).

Furthermore, the sloshing motion is more pronounced at the far side. This is found in a stronger shape variation of the cloud boundary at the far side. The sloshing and stretching motion of small dust clouds showed a similar behavior. There, a distinct stretching motion at the far side and a compression at the anode-facing side was found.[22]

As mentioned before, the slope of the wave fronts varies with time and has a lower inclination, i.e., the wave propagates faster, in the expansion phase of the sloshing motion when the dust cloud is pushed away from the anode to the right hand side (see, e.g., time interval 0.8–1.0 s). In Figs. 5(b) and 5(d) the sloshing velocity v_s [gray line (red online)] and the phase velocity of the wave v_φ (black line) are shown for 1 and 2 Hz, respectively.

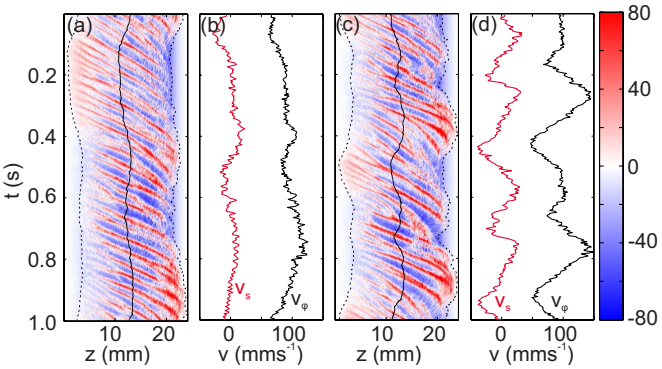

FIG. 5. (Color online) Space-time diagrams for modulation frequencies of (a) 1 Hz and (c) 2 Hz. The position of the center of mass and the envelope are indicated with solid and dashed lines, respectively. The corresponding sloshing velocity v_s [gray line (red online)] and phase velocity of the wave v_φ (black line) are shown in (b) and (d).

To understand the interaction of an externally excited sloshing motion and a simultaneously propagating wave, both motions are expected to be independent. Hence, the observed wave pattern can be approximated by a superposition of both. This simple assumption is supported by the observed spectra, where in the core region of the cloud [Fig. 4 no. (II)] at 1 Hz modulation frequency the wave spectrum resembles the self-excited wave, and the modulation frequency becomes dominant only at the cloud boundary.

The assumption of a superposition of the sloshing motion and the self-excited wave can be verified by analyzing the velocities of the sloshing motion, the phase velocity of the self-excited wave and the phase velocity of the observed wave. It is found that the sloshing motion and the wave velocity are in phase, and the wave speed is accelerated during the expanding time of the sloshing motion. But it is also found that the response of the wave $[v_\varphi=(60-120)\ \text{mm s}^{-1}]$ is stronger than expected compared to a simple addition of the sloshing velocity $[v_s=(-25\cdots20)\ \text{mm s}^{-1}]$ and the phase velocity of the self-excited wave $(v_{\varphi,m}=75\ \text{mm s}^{-1})$.

In summary, it is found that for the low-frequency modulation of a self-excited wave the sloshing motion and the wave propagation interfere with each other and that the appearance of strong higher harmonics hints at subharmonic synchronization of the dust density wave.

V. MEDIUM AND HIGH MODULATION FREQUENCIES: WAVE SYNCHRONIZATION

As described in the previous section, the wave can be synchronized at modulation frequencies of $f\approx14$ Hz. In this section, the influence of modulation frequencies in the range of $f=(20-140)$ Hz is studied.

In Fig. 6 the dynamics of the excited waves are shown for representative excitation frequencies of 20, 30, 40, 70,

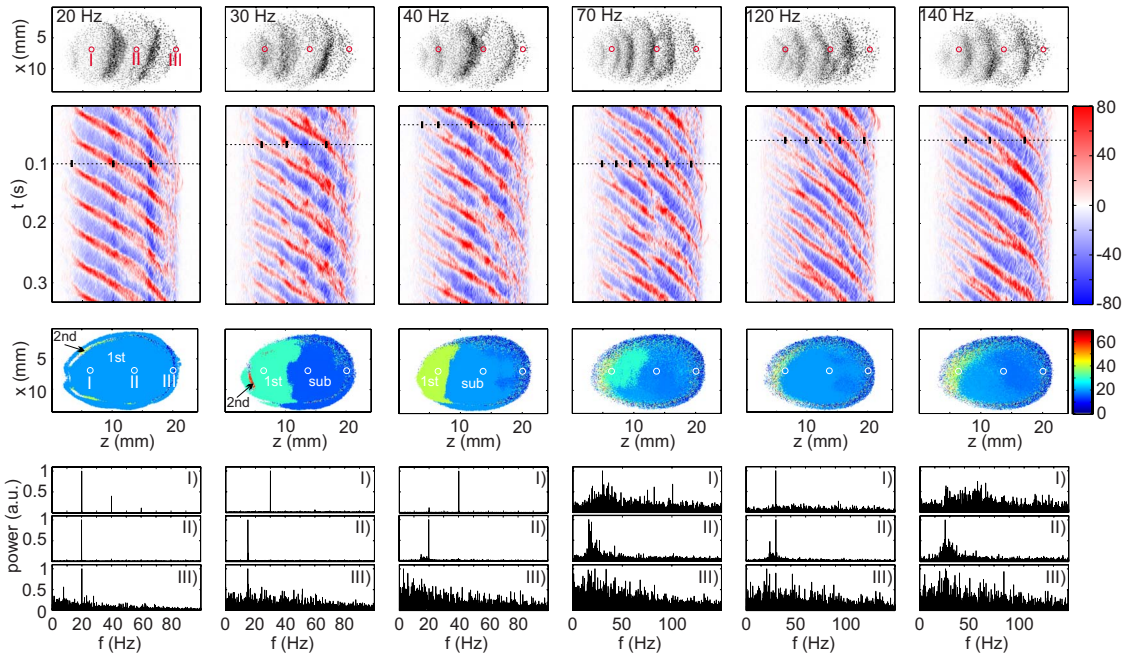

FIG. 6. (Color online) Response of the cloud on different modulation frequencies (from left to right: 20, 30, 40, 70, 120, and 140 Hz). Displayed are in columns the raw images, the space-time diagrams, the frequency distribution of the dominant component, and the corresponding spectra at positions marked with open circles and labeled with Roman numerals at 20 Hz. The labels 1st (2nd) and sub refer to the regions of the first (second) harmonic and the subharmonic.

120, and 140 Hz. The organization of the figure is identical to Fig. 4.

It is found that for all frequencies the wave fronts are affected by the modulation. The wave fronts are more pronounced, and contain a larger number of particles, so that the dust density is increased, and the shape of the wave fronts is broader than the shape of the undisturbed self-excited wave fronts.

For an excitation frequency of 20 Hz a regularly propagating wave was found as can be seen by diagonal, parallel wave fronts in the space-time diagram. The phase velocity of the wave is higher in the anode-facing region of the cloud than in the far region. This can be seen by the smaller slope of the wave fronts on the left hand side of the space-time diagram, the boundary of the changing velocity is close to a z-position of 15 mm. The frequency map shows a homogeneous frequency distribution with a dominant component at the first harmonic of the external frequency. The second harmonic is found in a narrow shell on the anode side.

For higher frequencies of 30 and 40 Hz, a bifurcation of the wave fronts in the space-time diagram is found. This point corresponds to a position where two wave fronts merge. Therefore, the wavelength is not constant over the entire z-direction. This observation can be directly seen in the snapshots of the dust cloud. For a better illustration, the position of the wave fronts in the space-time diagram is marked by a horizontal dashed line. The wavelength in the far region is nearly twice as large as the wavelength in the front region.

In the frequency map, two dominant regions can be found. In the front region, the dominant frequency component is equal to the external modulation frequency. In the back region, the subharmonic frequency of the wave becomes dominant. For increasing modulation frequency, the region with the fundamental frequency shrinks whereas the region of the subharmonic frequency becomes larger. The dependence of the modulation frequency on the position of the bifurcation point is shown in Fig. 7. It is found that its position is shifted for increasing frequency toward the anode-facing side. Hence, the entrainment region at the first harmonic of the modulation frequency shrinks.

At a modulation frequency of 70 Hz, the wave is no longer entrained and the spectrum becomes broad again with a peak at $f \approx 30$ Hz in spectrum (I) and $f \approx 15$ Hz in spec-

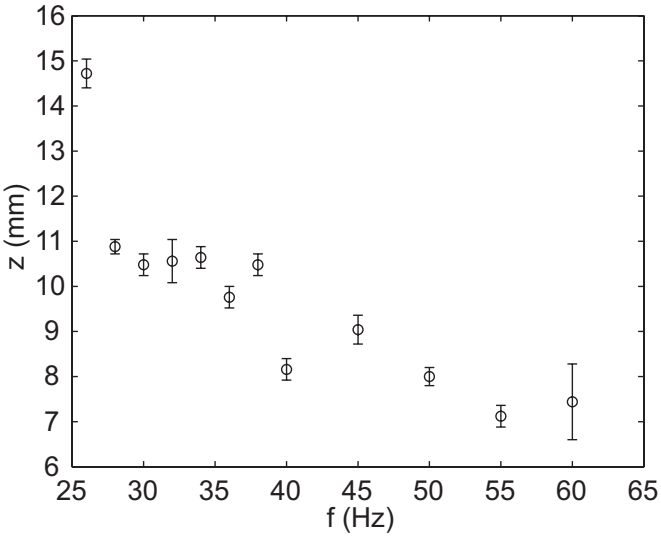

FIG. 7. The position of the bifurcation point from a dominant first harmonic to a dominant subharmonic is shown in dependence of the applied modulation frequency.

trum (II). For the highest frequencies of 120 and 140 Hz, the wave dynamics is more regular compared to the self-excited wave. The calculated main frequency component is near $f \approx 20$ Hz and the narrow width of the spectral lines hints at superharmonic entrainment of the self-excited wave.

A pronounced bifurcation structure for the modulation frequencies of 120 and 140 Hz is found. This merging of wave fronts is periodical. In case of the modulation at 140 Hz, the merging wave fronts propagate approximately at the same phase velocity, which is seen by their parallel orientation, but then the second wave is accelerated to a higher phase velocity until the wave fronts merge and the resulting wave front propagates at the previously slower phase velocity.

VI. DISCUSSION AND CONCLUSIONS

A. Self-excited wave

The analysis of the self-excited wave has shown an incoherent wave pattern, where the wavelength and the wave frequency are varying in time and space. This can be seen by the analysis of the spectra. A broad frequency distribution is found and a better characterization of the wave is given by the mean frequency. In the frequency map a spatial distribution of the mean frequencies is observed. It is found that the frequency is slightly shifted from higher components at the anode-facing side toward lower frequencies at the anode far side.

The observation of a frequency distribution and an incoherent time evolution of self-excited waves is in agreement with other experimental results.[25,26] Samaryan *et al.*[25] studied the spatial distribution of frequency, wavelength, and phase velocity. They found a similar behavior of an incoherent wave structure as described in this work. On the other hand, Menzel *et al.*[26] studied self-excited dust density waves under microgravity conditions. For certain selected conditions, a very coherent wave pattern was observed, which could be used for a three-dimensional reconstruction of the wave front. It was also found that under different conditions an incoherent wave pattern with merging wave fronts appears. The crucial parameter seems to be the particle number.

Therefore, we conclude that self-excited waves can appear either as an incoherent wave pattern of merging wave fronts and varying wavelength, or as a coherent wave. However, the incoherent waves tend to be preferred.

B. Modulation of the anode voltage

In order to understand how a modulation of the anode voltage affects the dust cloud, especially the dynamics of the dust particles, the confinement of the cloud has to be considered.

The cloud confinement in the z-direction is mainly defined by a force equilibrium of the inward-directed electric field force and the outward-directed ion drag force, due to the small particles the force of gravity is neglected. The radial confinement is induced by strong radial electric fields.

The ion drag force depends on the ion density and the electric field, which accelerates the ions. Probe measurements showed that, when the anode voltage is increased (decreased), the plasma potential and the ion density is increased (decreased) as well. However, the shape of the axial potential distribution is only slightly altered and at the position of the dust cloud the plasma potential is well approximated by a straight line. Hence, the electric field for different anode voltages is nearly constant. Consequently, the electric field force is constant as well and the variation of the force equilibrium depends mainly on the variation of the ion drag force during the modulation whereas the ion drag force then mainly depends on the ion density.

A simplified picture of the modulation of the anode voltage then results in a static shift of the confinement potential toward the anode disk for lower anode voltages and away from the anode disk for higher anode voltages. This variation exerts an additional net force on the dust cloud. Hence, the anode voltage modulation can be understood in terms of a parametric excitation due to the modulated ion density.

The confinement potential itself has an anharmonic shape, which was previously verified by the observation of a stretching motion for small dust clouds at low frequency modulations.[22] Hence, the shape of the potential well has a stronger gradient at the anode-facing side than at the far side. Thus, the restoring force acting on the particles should be asymmetric for the inward and outward moving confinement potential.

C. Sloshing

For very low frequencies of $f \approx (1-3)$ Hz a distinct sloshing motion of the entire dust cloud was found. Compared to our previous work[22] the sloshing motion in large clouds is studied, where the self-excited dust density wave is still present and propagates through the cloud.

Due to the fact that the external modulation frequency is very low compared to the broad frequency distribution of the self-excited wave, we assume that the wave propagation and the sloshing motion can be added up. This assumption is supported by the analysis of the sloshing velocity and the phase velocity of the wave, which are in phase, and the velocity of the wave can be approximated by the simple adding model whereas the response of the phase velocity of the wave is stronger than expected. This observation might be explained by the anharmonic confinement potential at the far side, where the gradient is less steep compared to the anode-facing side. Thus, the cloud can flow out at the far side and therefore the larger response is found.

D. Subharmonic synchronization

For the low frequency range of $f \approx (4-12)$ Hz, an interaction of the sloshing motion and the wave propagation was found. Similar to the very low frequency modulation, the boundary has shown a response in agreement with the modulation frequency. But the wave propagation is perturbed in a non-negligible way, where a complex structure in the space-time diagram was found in-phase with the modulation frequency.

The wave spectra have shown a number of harmonics, in particular at higher modulation frequencies above 10 Hz.

Therefore, we assume that the low frequency modulation, compared to the self-excited wave frequency, results in a subharmonic synchronization of the wave.

E. Wave synchronization and wave decay

In the frequency range $f \approx (16-24)$ Hz, the wave was entrained at the modulation frequency over the entire dust cloud apart from a small ringlike structure close to the cloud boundary. We suggest that the latter can be attributed to reflected particles at the boundary of the cloud. A reflection of a wave front at the boundary of the cloud was previously described by Thomas, Jr., and Merlino,[27] thus particle reflection is reasonable. It was also found that the phase velocity of the wave is slowed down at the far side.

In the very large frequency range, $f \approx (26-60)$ Hz, we found an entrained wave at the anode-facing side. However, at the far side, a wave with a dominant component at the subharmonic $f = f_{\mathrm{mod}}/2$ was found. This decay toward lower frequency is accompanied by a reduction in the wavelength.

One explanation for this behavior could be the natural frequency distribution of the self-excited wave, where a frequency shift from higher to lower frequency components from the anode-facing to the far side was observed. Therefore, the wave decay toward the subharmonic frequencies is naturally preferred.

It is suggested that the synchronization of the self-excited wave is driven by a parametric excitation due to the ion density variation, which appeared to be the most significant effect of the frequency modulation. In terms of the simple fluid theory, the ion density is connected with the wave velocity $c_{\mathrm{DAW}} = \omega_{pd} \lambda_D$, where c_{DAW} is the dust acoustic velocity, ω_{pd} is the dust plasma frequency, and λ_D is the Debye length. Thus, via the ion density modulation, the Debye sphere is modulated and therewith the dust acoustic velocity is modulated as well.

In contrast with our observations, Williams *et al.*[12] found a synchronized dust density wave in a small frequency range of $f \approx (10-20)$ Hz. However, the self-excited wave was analyzed with respect to a distribution of the wavenumber [$k \approx (0.1-0.2)$ cm^{-1}]. By reasoning that the wavenumber has a wide distribution, and that the driven waves have shown a narrower distribution, which lies in the range of the self-excited wave or close to it, the authors supposed that a single k-mode is preferentially excited due to the modulation.

At very high modulation frequencies no synchronization at the fundamental was found, but the wave propagation was more coherent compared to the self-excited waves. It was found that the modulation tends to drive the wave, if the excitation frequency is a multiple of 20 Hz. This observation hints at a superharmonic synchronization, although the frequency is quite high. In terms of the van der Pol oscillator, it is known that the Arnol'd tongues, which define the synchronization range in an amplitude versus frequency plot, become narrower for increasing number of superharmonics. Thus, the modulation frequency has to be very close to a rational factor of the natural frequency. Anyhow, this aspect should be studied in further detail and with a higher frequency resolution at these high frequencies.

Comparing our observation at the high frequency modulation with the results obtained by Thomas *et al.*[11] and Williams *et al.*,[12] a general agreement is found. The authors also found that at the high frequency modulation the dust density wave is not driven at these frequencies but rather propagates like the self-excited wave, whereas in our experiment a more coherent wave pattern with superharmonic synchronization was observed. Additionally, Thomas *et al.*[11] found a high frequency modulation of the wave fronts superimposed to the self-excited wave. This is neither seen in our experiment nor in the experiment by Williams *et al.*[12] and might be attributed due to the use of monodisperse particles as mentioned by Williams *et al.* instead of the polydisperse dust distribution used by Thomas *et al.*

VII. SUMMARY

In summary, we analyzed the response of an incoherent (noisy) self-excited dust density wave to an external modulation over a wide frequency range of $f = (1-140)$ Hz. It was found that a sloshing motion of the entire dust cloud interferes with the self-excited wave and that the observation can be understood by a superposition of the sloshing motion and the wave propagation. The synchronization has shown a complex behavior, where we described a subharmonic synchronization for low frequencies, a harmonic synchronization for an intermediate frequency regime with a spatially wave decay and a kind of superharmonic synchronization at high frequencies.

ACKNOWLEDGMENTS

Fruitful discussions with K. O. Menzel and O. Arp are gratefully acknowledged. The present investigations were financially supported by DFG within the transregional collaborative research center TR-24, project A2.

[1] E. Thomas, Jr., Contrib. Plasma Phys. **49**, 316 (2009).
[2] T. Trottenberg, D. Block, and A. Piel, Phys. Plasmas **13**, 042105 (2006).
[3] A. Barkan and R. L. Merlino, Phys. Plasmas **2**, 3261 (1995).
[4] N. N. Rao, P. K. Shukla, and M. Y. Yu, Planet. Space Sci. **38**, 543 (1990).
[5] M. Rosenberg, J. Plasma Phys. **67**, 235 (2002).
[6] S. A. Khrapak, S. V. Ratynskaia, A. V. Zobnin, A. D. Usachev, V. V. Yaroshenko, M. H. Thoma, M. Kretschmer, H. Höfner, G. E. Morfill, O. F. Petrov, and V. E. Fortov, Phys. Rev. E **72**, 016406 (2005).
[7] S. Ratynskaia, S. Khrapak, A. Zobnin, M. H. Thoma, M. Kretschmer, A. Usachev, V. Yaroshenko, R. A. Quinn, G. E. Morfill, O. Petrov, and V. Fortov, Phys. Rev. Lett. **93**, 085001 (2004).
[8] S. Khrapak, D. Samsonov, G. Morfill, H. Thomas, V. Yaroshenko, H. Rothermel, T. Hagl, V. Fortov, A. Nefedov, V. Molotkov, O. Petrov, A. Lipaev, A. Ivanov, and Y. Baturin, Phys. Plasmas **10**, 1 (2003).
[9] V. E. Fortov, A. D. Usachev, A. V. Zobnin, V. I. Molotkov, and O. F. Petrov, Phys. Plasmas **10**, 1199 (2003).
[10] C. Thompson, A. Barkan, N. D'Angelo, and R. L. Merlino, Phys. Plasmas **4**, 2331 (1997).
[11] E. Thomas, Jr., R. Fisher, and R. L. Merlino, Phys. Plasmas **14**, 123701 (2007).
[12] J. D. Williams, E. Thomas, Jr., and L. Marcus, Phys. Plasmas **15**, 043704 (2008).

[13]M. Rosenberg, E. Thomas, Jr., and R. L. Merlino, Phys. Plasmas **15**, 073701 (2008).
[14]M. E. Koepke, A. Dinklage, T. Klinger, and C. Wilke, Phys. Plasmas **8**, 1432 (2001).
[15]T. Klinger, in *Handbook of Chaos Control*, edited by H. G. Schuster (Wiley-CHV, Weinheim, 1999), Chap. 20, pp. 513–561.
[16]E. A. Jackson, *Perspectives of Nonlinear Dynamics* (Cambridge University Press, New York, 1989).
[17]A. Pikovsky, M. Rosenblum, and J. Kurths, *Synchronization* (Cambridge University Press, Cambridge, 2001).
[18]A. Balanov, N. Janson, D. Postnov, and O. Sosnovtseva, *Synchronization: From Simple to Complex* (Springer, Berlin, Heidelberg, 2009).
[19]A. E. Siegman, *Lasers* (University Science Books, Mill Valley, 1986), Chap. 29, pp. 1130–1170.
[20]V. Yaroshenko and G. E. Morfill, Phys. Plasmas **9**, 4495 (2002).
[21]J. Pramanik, B. M. Veeresha, G. Prasad, A. Sen, and P. K. Kaw, Phys. Lett. A **312**, 84 (2003).
[22]I. Pilch, T. Trottenberg, A. Piel, and M. E. Koepke, Phys. Plasmas **14**, 123704 (2007).
[23]MATLAB, The MathWorks, Inc., 3 Apple Hill Drive Natick, MA 01760–2098, USA, http://www.mathworks.com/.
[24]The summation was performed for frequencies up to 60 Hz, which is below the Nyquist limit. Above this frequency no significant spectral components have been observed.
[25]A. A. Samaryan, A. V. Chernyshev, O. F. Petrov, A. P. Nefedov, and V. E. Fortov, Sov. Phys. JETP **92**, 454 (2001).
[26]K. O. Menzel, O. Arp, D. Caliebe, and A. Piel, "The structure of self-excited dust-density waves under microgravity," IEEE Trans. Plasma Sci. (accepted).
[27]E. Thomas, Jr., and R. L. Merlino, IEEE Trans. Plasma Sci. **29**, 152 (2001).

C Reprints of Conference Proceedings

C.1

SYNCHRONIZATION OF DUST DENSITY WAVES IN ANODIC PLASMAS

I. Pilch, M. E. Koepke, A. Piel, and T. Trottenberg

34th EPS Conference on Plasma Physics
Warsaw, 2-6 July 2007
Europhysics Conference Abstracts Volume 31F, P-5.062

34th EPS Conference on Plasma Phys. Warsaw, 2 - 6 July 2007 ECA Vol.**31F**, P-5.062 (2007)

SYNCHRONIZATION OF DUST DENSITY WAVES IN ANODIC PLASMAS

I. Pilch[1], M. E. Koepke[2], A. Piel[1], T. Trottenberg[1]

[1] *IEAP, Christian Albrechts-Universität, Kiel, Germany*

[2] *Department of Physics, West-Virginia-University, Morgantown, USA*

It is well known that self-excited dust density waves [1, 2] in current carrying dusty plasmas can apparently be "synchronized" by an external periodic modulation of the discharge voltage [3]. This method was used to measure the dispersion relation of the dust-density wave [3, 4]. However, little is known about the detailed mechanism behind the synchronization. The present investigation is concerned with the response of the dust cloud to modulation of the discharge voltage over a wide frequency range.

Our experiments were performed in the magnetized radio-frequency discharge described in [4]. The argon plasma ($p = 2$ Pa) has a density $n_e \approx 10^{15}$ m^{-3}, and electron temperature $T_e = 3$ eV. In the magnetic field ($B = 20$ mT) the electrons are magnetized and the ions unmagnetized. The different Hall parameters are responsible for the formation of a radial electric field that provides radial dust confinement. The anodic plasma forms in front of a small disk electrode of 30 mm diameter that is held at a high positive potential of 60…75 V. Figure 1(a) shows the potential contours measured with an emissive probe [4]. A cloud with an ellipsoidal shape containing spherical melamine particles (0.97 ± 0.05 μm diameter) is trapped inside this anodic plasma. The axial confinement is a balance of the ion drag force F_{ion} and the axial electric field force F_C, which form an effective potential that traps the dust as shown in Fig. 1(b). The hatching marks the region in which dust can be trapped, which agrees with the position and width of the dust cloud.

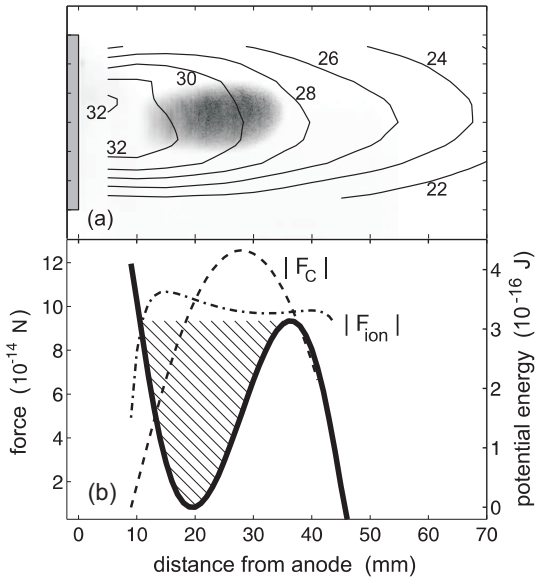

Figure 1: (a) Dust cloud and electric potential contours in a horizontal section, (b) effective potential well formed by ion drag and electric field force.

The dust particles are observed with the combination of a horizontal sheet of laser light ($\lambda = 532$ nm, 200 mW), positioned in the midplane of the dust cloud, and a fast CCD video

camera. Self-excited waves are only found in dust clouds, which exceed a minimum size of ≈ 5 mm. These self-excited waves have frequencies of $f = (25 \ldots 30)$ Hz and can be stimulated by modulating the anode bias with external frequencies f_{mod}.

Our first series of investigations was focused on the response of stable small dust clouds to external modulation in the frequency range (1 – 20) Hz. We find that, at low frequencies, the dust cloud performs a sloshing and stretching motion (Fig. 2), which is analyzed in the following way: The dust density information is obtained from the intensity distribution $B_{ij}(t)$ of scattered laser light in each frame of the video recording after subtracting the signal background in a dark frame. Herefrom we deduce the "center of mass" position in each frame

$$x_{c.o.m.}(t) = \frac{1}{B_{tot}(t)} \sum_{i=0}^{N-1} \sum_{j=0}^{M-1} j B_{ij}(t) \,, \qquad (1)$$

where $B_{tot}(t) = \sum_i \sum_j B_{ij}(t)$ is the total intensity in that frame.

The x-direction corresponds to the magnetic field direction. The stretching of the dust cloud is obtained by calculating the second moment of the intensity distribution

$$d_x^2 = \frac{1}{B_{tot}(t)} \sum_{i=0}^{N-1} \sum_{j=0}^{M-1} [j - x_{c.o.m.}(t)]^2 B_{ij}(t) \,. \qquad (2)$$

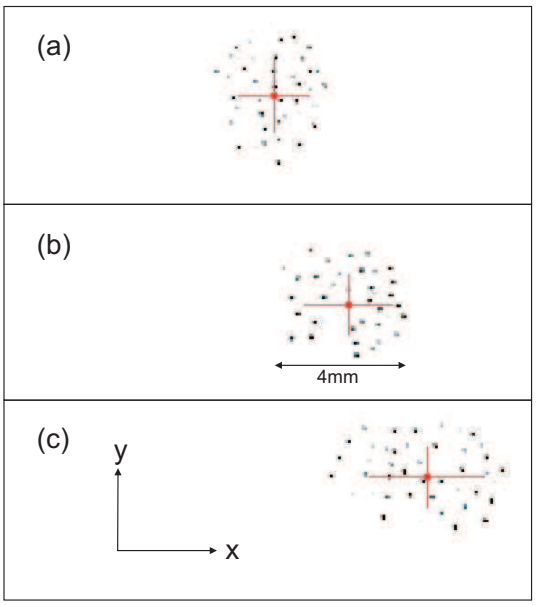

Figure 2: Sloshing and stretching of the dust cloud at low modulation frequency $f_{mod} = 4$ Hz. ($U_a = 70$ V, $U_{mod} = 10$ V$_{pp}$). (a) left turning point, (b) equilibrium position, (c) right turning point.

The sloshing amplitude in x-direction is dependent on the applied frequency (full circles) in Fig. 3). The c.o.m. motion at the lowest frequency ($f_{mod} = 1$ Hz) is representative for the static shift of the dust cloud's equilibrium position with applied anode bias U_a. With increasing frequency, the sloshing amplitude becomes larger and attains a maximum at 4 Hz. For even larger frequencies, the sloshing amplitude decreases rapidly. The sloshing motion has obviously a resonant response to the external modulation. A similar behavior with a resonance at the same frequency is found for the stretching of the dust cloud (circles in Fig. 3). In summary, we understand the combined sloshing and stretching as the motion of the dust fluid in an asymmetric potential well whose x-position changes according to the applied modulation.

For small dust clouds no self-excited waves are found in the investigated frequency range (1–60) Hz. Nor does the external modulation excite any propagating density waves, which should become visible in the range $f_{mod} > 20$ Hz, where the sloshing and stretching motion disappears.

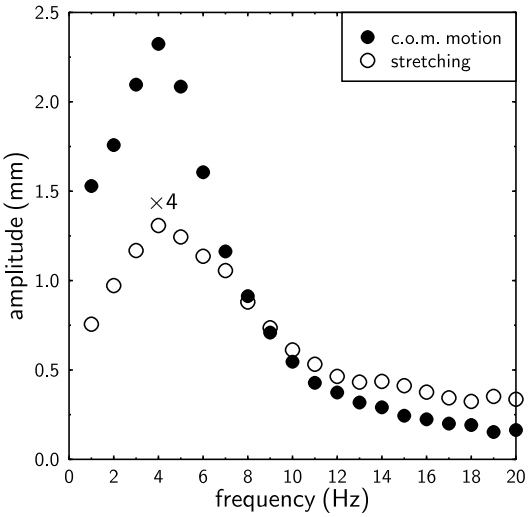

Figure 3: Response of the dust cloud to external modulation.

The self-excited dust density waves found in larger dust clouds represent a spatially amplifying plasma medium. When self-excited waves in such a system are stimulated by an external signal at a different but close-by frequency, the situation resembles the phenomenon of injection locking of lasers [6]. Injection locking can be described by a periodically driven van der Pol-oscillator. This model was also successfully used to describe the spatio-temporal synchronization of plasma waves, e.g., in neon-gas discharges [7] or drift waves [8].

First we have studied the system response in the vicinity of the naturally excited modes by choosing the modulation frequency in the range $f_{mod} = (15 \ldots 40)$ Hz. Surprisingly, in the entire range, the system response was found as a monochromatic wave at the modulation frequency f_{mod} and its harmonics (see Fig. 4). For a van der Pol-system we would have expected the transition from a quasiperiodic state with the two independent frequencies $f \neq f_{mod}$ to a phase-locked state with $f = f_{mod}$. In other experiments, the phase-locking range had a typical width $2\Delta f_{mod}/f < 0.2$ [9]. Here, the single-frequency response is found over a very much wider frequency range, which sheds doubt on the concept of synchronization in a van der Pol scenario for this system. Rather, the actual system behavior bears similarities with the case of injection seeding, where a seed wave with an amplitude above the noise level sets the proper initial conditions for the wave that subsequently wins the competition with all other noise-excited modes.

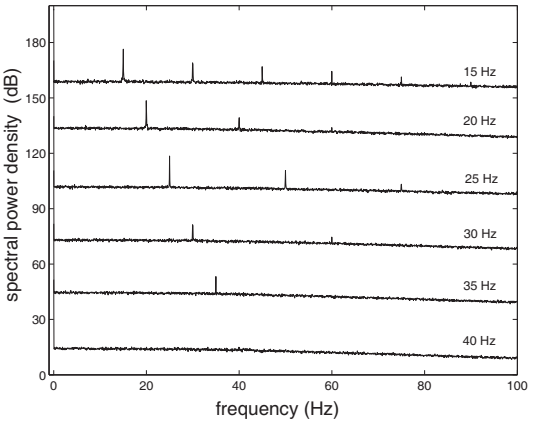

Figure 4: Frequency spectra of the excited waves.

In a second step, we have investigated the system response when the modulation frequency is chosen close to the first harmonic of the naturally excited modes, $f_{mod} \approx 2f$. In this situation

we expected superharmonic synchronization, as observed in [9]. For this purpose the wave is recorded by triggering the camera shutter synchronously at $f_{mod}/2$. In this way an entrained wave would give a system of standing phase fronts. An independent mode appears at the beat frequency $f - f_{mod}/2$.

The response of the system, however, did not show any clear entrainment of the natural mode to the modulation signal. A spectral analysis of the beat spectrum (see Fig. 5) shows that it is determined by the natural mode as seen from the reference frame of the modulation signal. A monochromatic natural mode at exactly $f = 29$ Hz would follow the dashed line. The dominant peak in each beat spectrum (full circles) obviously follows this expectation. However, the beat spectrum is more complex with additional peaks (open circles). In summary, the observed waves resemble the phenomenon of injection seeding of pulse lasers, which also do not show the van der Pol behavior found in injection locking of cw lasers.

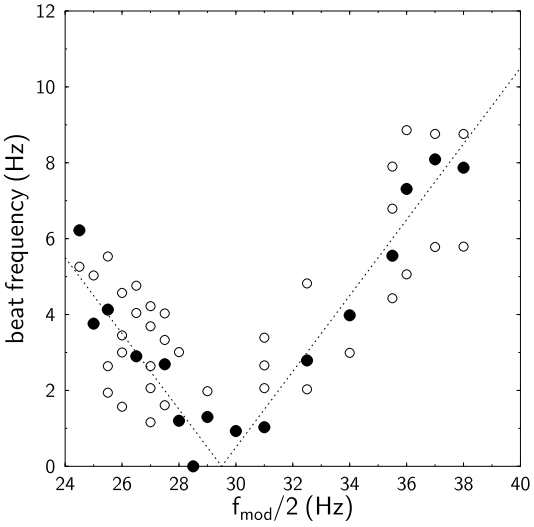

Figure 5: Measured beat spectrum as a function of modulation frequency.

This work was financially supported by DFG under contract SFB-TR24 A2.

References

[1] N. N. Rao, P. K. Shukla, M. Y. Yu, Planet. Space Sci. **38**, 543 (1990)

[2] A. Barkan, R. L. Merlino, N. D'Angelo, Phys. Plasmas **2**, 3563 (1995)

[3] C. Thompson, A. Barkan, N. D'Angelo, R. L. Merlino, Phys. Plasmas **4** 2331 (1997)

[4] T. Trottenberg, D. Block, A. Piel, Phys. Plasmas **13**, 042105 (2006)

[5] A. Piel, I. Pilch, T. Trottenberg, M. E. Koepke, *this conference*

[6] A. E. Siegman, *Lasers*, Chap. 29, University Science Books, Mill Valley CA (1986)

[7] K. D. Weltmann, M. E. Koepke, C. A. Selcher, Phys. Rev. E **62**,2773 (2000)

[8] D. Block, A. Piel, Plasma Phys. Control. Fusion **45**, 413 (2003)

[9] T. Klinger, A. Piel, I. Axnäs, S. Torvén, Physica Scripta **56**, 70 (1997)

C.2

THREE-DIMENSIONAL STRUCTURE OF DUST CLOUDS AND WAVE FRONTS IN AN ANODIC PLASMA

A. Piel, I. Pilch, T. Trottenberg, and M. E. Koepke

34th EPS Conference on Plasma Physics
Warsaw, 2-6 July 2007
Europhysics Conference Abstracts Volume 31F, P-5.063

34th EPS Conference on Plasma Phys. Warsaw, 2 - 6 July 2007 ECA Vol.**31F**, P-5.063 (2007)

THREE-DIMENSIONAL STRUCTURE OF DUST CLOUDS AND WAVE FRONTS IN AN ANODIC PLASMA

A. Piel[1], I. Pilch[1], T. Trottenberg[1], M. E. Koepke[2]

[1] *IEAP, Christian Albrechts-Universität, Kiel, Germany*

[2] *Department of Physics, West-Virginia-University, Morgantown, USA*

Dust density waves [1] are naturally excited modes in current carrying dusty plasmas [2]. The wave fronts appear as bright regions in scattered laser light. Because of their low frequency (15-40 Hz) these modes are ideally suited for studies with digital video cameras. The dispersion relation of these modes for dust trapped in an anodic plasma was studied before and compared with a fluid model [3] and kinetic theory [4]. While the earlier investigations were made in dust clouds that were larger than 3-4 wavelengths, which justifies the assumption of nealy plane waves and the comparison with models for a homogeneous and infinitely large system, the present investigation is concerned with the quantitative measurement of the wavefronts in smaller systems.

The experiments were performed in the magnetized radio-frequency discharge described in [4]. The argon plasma ($p = 2$ Pa) has a density $n_e \approx 10^{15}\mathrm{m}^{-3}$, and electron temperature $T_e = 3$ eV. In the magnetic field ($B = 20$ mT) the electrons are magnetized and the ions unmagnetized. The different Hall parameters are responsible for the formation of a radial electric field that provides dust confinement. The anodic plasmas forms in front of a small disk electrode of 30 mm diameter that is held at a high positive potential of $60 \ldots 75$ V (see Fig. 1). A cloud with an ellipsoidal shape containing spherical melamine particles of $(0.97 \pm 0.05)\mu$m diameter is trapped inside the anodic plasma. Its axial confinement is a balance of the ion drag force and the axial electric field force [4]. The dust particles are observed with the combination of a horizontal sheet of laser light ($\lambda = 532$ nm, 200 mW) and a fast CCD video camera with 640×480 pixel and up to 150 frames per second. The camera and laser sheet can be moved vertically to record the particle motion in a series of horizontal slices.

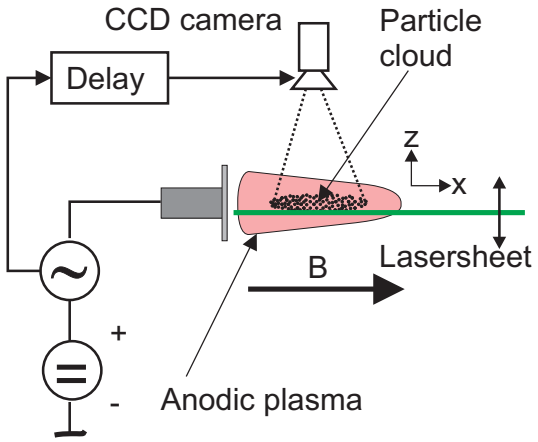

Figure 1: Experimental arrangement. The waves are observed with a fast video camera and a horizontal laser sheet.

Dust density waves are excited by the axial ion flow through the dust cloud. The frequency

of these waves can be locked by a sinusoidal modulation of the anode voltage [3, 4]. In the first set of experiments, the shutter of the video camera is triggered synchronously with the modulation voltage. This produces a series of stroboscopic images at the same phase of the wave. By averaging over 100 samples we obtain the dust density distribution in the wave from the intensity of the scattered light. Fig. 2 shows a series of horizontal sections at various vertical positions $z = (-3 \ldots -9)$ mm. $z = 0$ mm corresponds to the center of the anode disk. The wave frequency is $f = 25$ Hz.

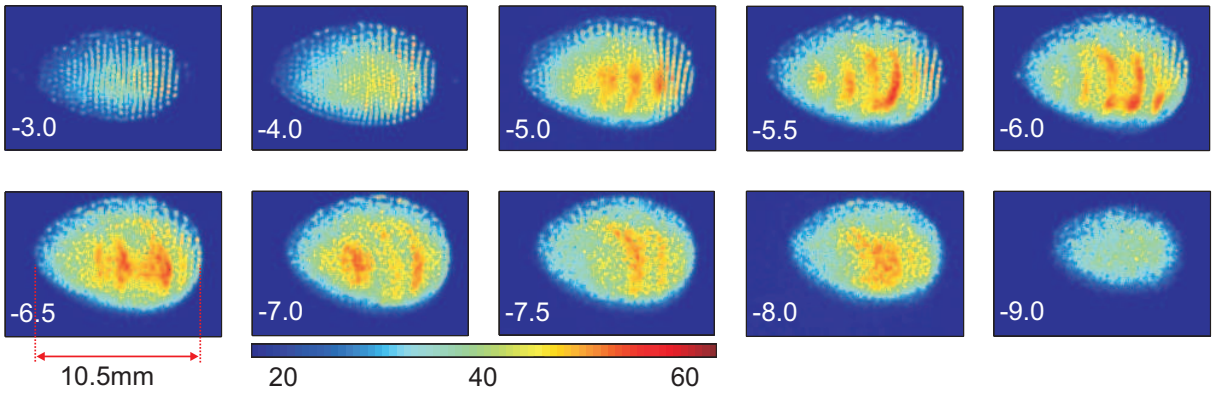

Figure 2: A series of horizontal sections obtained by the stroboscopic recording of the dust density fluctuations in the wave.

Obviously a dust cloud of 10.5 mm length and 7.3 mm diameter is trapped in the lower half of the anode disk, where a stronger radial electric field exists. The top of the dust cloud ($z = -3$ mm) shows that the dust particles are arranged in a set of parallel stripes. These stripes are perpendicular to the magnetic field direction and apparently the stripes do not move in axial direction, which can be seen from the sharp image in the average over 4 s. In transverse direction the image is slightly blurred but still individual particles can be recognized. The distance of the stripes is the same as the interparticle distance d. In a hexagonal lattice the distance would be $0.86d$. This crystalline order gradually disappears when we compare with sections taken at lower positions (see Fig. 4).

The dust density waves can be seen as strong periodic density modulations in the regime $z = -5 \ldots -8$ mm. By changing the trigger delay we have verified that the waves move from left to right, i.e. in the direction of the axial ion flow away from the anode disc. The wave fronts are curved and apparently emanate from a point-like source at the left side of the dust cloud. The wave amplitude increases during propagation but is already saturated in the center of the cloud. The wave amplitude falls to zero at the right edge of the cloud.

The stroboscopic method has the disadvantage that wave fronts can only be seen in terms of the wave crests. A more refined analysis can be made from long movies of the density wave in the case that wave frequency and frame rate of the camera are incommensurate. For this purpose we have recorded a movie with 8192 frames at 473 frames per second. A FFT-analysis of the intensity fluctuations in a cluster of 21×21 pixels in the center of the cloud shows that the spectrum has only sharp lines at 25 Hz and its harmonics. The fundamental has an intensity that is 20 dB higher than the incoherent background. Hence the wave is highly coherent. Therefore, we can determine the complex wavefunction $C(x,y) + \mathrm{i}S(x,y)$ by projecting the intensity distribution $B_i(x,y)$ in the frames $i = 0 \ldots N-1$ on the dominant Fourier component at the fundamental frequency $\omega_0/2\pi = 25$ Hz.

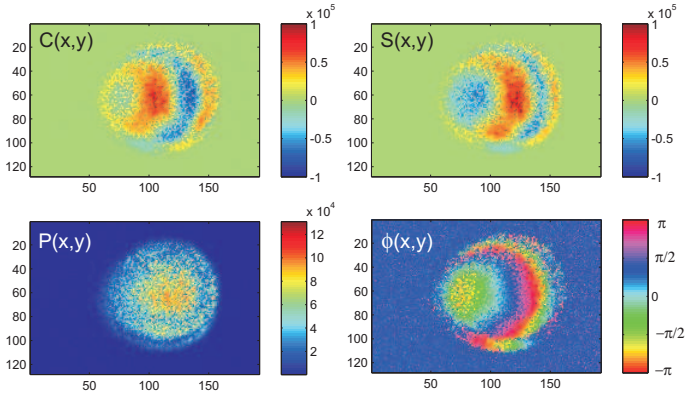

Figure 3: Complex wave function, wave energy density and phase evolution. The axis labels give x and y-coordinates in pixels.

$$C(x,y) = \frac{1}{N}\sum_{i=0}^{N-1} B_i(x,y)\cos\omega_0 t \quad ; \quad S(x,y) = \frac{1}{N}\sum_{i=0}^{N-1} B_i(x,y)\sin\omega_0 t \tag{1}$$

From the complex wave amplitude we immediately obtain the distribution of the wave phase $\varphi(x,y) = \arctan[S(x,y)/C(x,y)]$ and wave amplitude $P(x,y) = [S(x,y)^2 + C(x,y)^2]^{1/2}$. These four quantities are compiled in Fig. 3. The wave function confirms the result of the stroboscopic measurement in Fig. 2 that the wave fronts are curved. This curvature and the origin of the wave from a spot on the left hand side of the dust cloud become even more evident in the phase distribution. The wave amplitude decreases towards the edge of the dust cloud. This decrease is counterintuitive because, at first glance, the boundary of the dust cloud could be considered as a free moving surface. Then, waves at the open end of a transmission line should be reflected with the same sign and the amplitude should attain twice the value which it has inside the waveguide. Here, the decrease of the wave amplitude at the boundary hints at reflection with the opposite phase, like in a shortcircuited transmission line. However, we find no evidence for standing waves, which would be expected as the eigenmodes of the spheroidal dust cloud. The obvious dominance of the forward travelling wave can be understood by the ion streaming instability that excites the wave. The wave propagating in the direction of the ion flow is amplified whereas the reflected wave is damped by friction

with the background gas. A tentative explanation for the curved wavefronts and the point-like origin of the waves could be the periodic modulation of the ion current. Ions are produced in the anodic plasma and impinge on the dust cloud, thereby depositing their momentum by Coulomb scattering on the dust particles preferentially within the first few crystal layers. Different from larger dust clouds, which are in a liquid state [4], the smaller dust clouds are crystalline in the upper half, as can be seen from the column (along y) averaged intensity distribution (averaged over 100 frames) for the top layer at $z = -3$ mm and the bottom layer at $z = -9$ mm. The parallel crystal layers become quite evident from the modulation in the plane $z = -3$ mm whereas the structure disappers at $z = -9$ mm. The observed parallel layers that are perpendicular to the magnetic field direction are quite different from the nested spherical shells which are typical of Yukawa balls [5]. The present investigation has further shown that dust density waves can be excited by ion flows even in the solid phase as discussed theoretically by Rosenberg et al. [6] with respect to the coupling of longitudinal and transverse phonons excited by an ion beam.

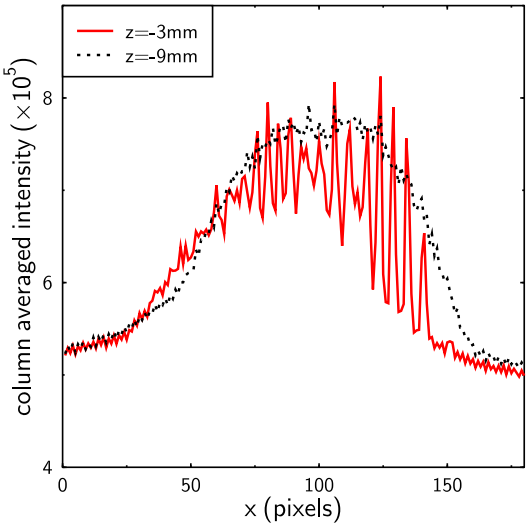

Figure 4: The crystalline structure becomes evident from the modulation of the column averaged intensity, which is pronounced at $z = -3$ mm and disappears at $z = -9$ mm.

This work was supported by DFG under grant SFB-TR24 A2.

References

[1] N. N. Rao, P. K. Shukla, M. Y. Yu, Planet. Space Sci. **38**, 543 (1990)

[2] A. Barkan, R. L. Merlino, N. D'Angelo, Phys. Plasmas **2**, 3563 (1995)

[3] C. Thompson, A. Barkan, N. D'Angelo, R. L. Merlino, Phys. Plasmas **4** 2331 (1997)

[4] T. Trottenberg, D. Block, A. Piel, Phys. Plasmas **13**, 042105 (2006)

[5] O. Arp, Block, Piel, Melzer, Phys. Rev. Lett. **93**, 165004 (2004)

[6] M. Rosenberg et al., J. Phys. A **39**, 4613 (2006)

C.3

TORUS-SHAPED DUST CLOUDS IN MAGNETIZED ANODIC PLASMAS

I. Pilch, T. Reichstein, F. Greiner, and A. Piel

Reprinted with permission from
I. Pilch, T. Reichstein, F. Greiner, and A. Piel,
AIP Conference Proceedings Volume 1041, Page 303-304
MULTIFACETS OF DUSTY PLASMAS: Fifth International Conference on the Physics of Dusty Plasmas,
Ponta Degada, Azores (Portugal), 18-23 May 2008,
ISBN: 978-0-7354-0569-1

Torus-Shaped Dust Clouds in Magnetized Anodic Plasmas

I. Pilch, T. Reichstein, F. Greiner and A. Piel

Institute for Experimental and Applied Physics, Christian-Albrechts University, D-24098 Kiel, Germany

Abstract. The generation of a torus-shaped dust cloud in an anodic plasma is decribed. The confined dust particles perfom a rotational motion around the torus major axis. The structure of the cloud in dependence of the external parameters are observed and the rotation velocity of the particles was measured and compared with a simple estimate.

Keywords: dusty plasmas, plasma magnetohydrodynamics
PACS: 52.27.Lw, 52.30.Cv

It is well known that dust clouds can be confined in weakly magnetized anodic plasmas [1, 2]. In our experiment, the source plasma is an rf discharge and a small disk anode of 3 cm diameter, which is biased at 60 . . . 80 V, is used. Recently, the dynamics of small dust clouds was discussed in this arrangement [3]. It was shown that the center of mass of these clouds is vertically displaced from the axis of the anodic plasma, in the direction of gravity, by typically six millimeters. For this shift, we suggested that a void region exists in the central region of the anode glow from which, by means of the ion drag force, the dust particles are expelled. The void phenomenon is well known from microgravity experiments [4]. This void is explained by the ambipolar diffusion of ions which are produced in the center of the discharge and pushes the particles radially to the chamber walls. The position of the void edge is defined by the equilibrium of the ion drag and the electric field force. In our situation, the ions perform an additional poloidal motion caused by the Lorentz force. For larger amounts of confined dust we observe torus-shaped clouds [3] with a dust free region in the center. The particles trapped in such a toroidal cloud show no ordered structures but perform a rotational motion about the torus major axis. Such a rotation caused by a magnetic field was already observed in two dimensional clusters [5, 6].

In our experiment the dust cloud was illuminated with a horizontal laser sheet and the scattered light of the particles was recorded by a CCD camera. The three dimensional structure of a dust cloud can be measured by scanning vertically the laser sheet through the cloud. The tori can be observed at typical parameters of $P_{RF} \geq 2$ W, $p > 5$ Pa, $B > 10$ mT and $U_A \geq 70$ V. The structure of the torus depends on the amount of dust which is confined in the anodic plasma. It is possible to make fat and slim tori. The maximum amount of dust is limited by the confinement potential. A slim torus can be used to indicate the equilibrium position of the inward directed electric field and the outward directed ion drag. Fig. 1(a) shows an example of a fat torus. The torus axis is oriented parallel to the magnetic field. In Fig. 1(b), a section through the midplane of a slim torus is shown. The axis ($x = 0$) is centered with the anode disk, which

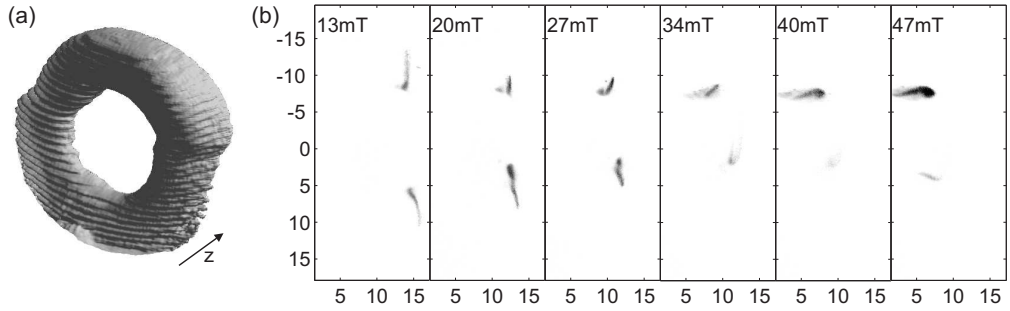

FIGURE 1. (a) Three-dimensional reconstruction of a fat torus. (b) Section through the midplane of a slim torus for different magnetic field.

defines the plane ($z = 0$). The torus size and the distance to the anode decreases with increasing magnetic field. The change in the size of the torus can be understood as follows: With increasing magnetic field the discharge current and likewise the plasma density decreases. Therefore, the ion wind force is reduced and the radial electric field force pushes the particles radially inwards. At high magnetic fields, the dust density becomes asymmetric with respect to the $\pm x$ symmetry of the torus.

We measured the velocity of the particles in a top section of the torus and obtained velocities in a range of $40 \ldots 100$ mm s^{-1}. We have also measured the dependence of the velocity on the magnetic field for different pressures and constant anode voltage. For different pressures the velocity does not significantly change. For increasing magnetic field, the velocity first increases but then decreases. The decrease of velocity may be explained by the observation that for high magnetic field the torus collapses. To compare our results, we estimated the velocity of the particles by a simple model, assuming a force equilibrium of the ion drag as driving force and the neutral gas as friction force. For our parameters, we obtained particle velocities of approximately $70 \ldots 120$ mm s^{-1} for pressures $p = 5.5 \ldots 8$ Pa, which approximately agrees with our measurements. This simple model predicts that for increasing magnetic field the velocity should increase and with decreasing pressure the velocity should decrease. This discrepancy has to be studied in more detail. One reason for this difference could be that, with increasing magnetic field, at constant anode voltage the anode current and hence the ion wind is reduced.

The present investigation were financially supported by DFG within the transregional collaboration research center TR-24, Project A2.

REFERENCES

1. A. Barkan *et al.*, Phys. Plasmas **2**, 3563 (1995)
2. T. Trottenberg *et al.*, Phys. Plasmas **13**, 042105 (2006)
3. I. Pilch *et al.*, Phys. Plasmas **14**, 123704 (2007)
4. G.E. Morfill *et al.*, Phys. Rev. Letters **83**, 1598 (1999)
5. U. Konopka *et al.*, Phys. Rev. E **61**, 1890 (2000)
6. F. Greiner *et al.*, this conference

C.4

DYNAMICS OF FINITE DUST CLOUDS IN A MAGNETIZED ANODIC PLASMA

A. Piel, I. Pilch, T. Trottenberg, and M. E. Koepke

Reprinted with permission from
A. Piel, I. Pilch, T. Trottenberg, and M. E. Koepke,
AIP Conference Proceedings Volume 1041, Page 301-302
MULTIFACETS OF DUSTY PLASMAS: Fifth International
Conference on the Physics of Dusty Plasmas,
Ponta Degada, Azores (Portugal), 18-23 May 2008,
ISBN: 978-0-7354-0569-1

Dynamics of Finite Dust Clouds in a Magnetized Anodic Plasma

A. Piel*, I. Pilch*, T. Trottenberg* and M.E. Koepke†

*Institute for Experimental and Applied Physics, Christian-Albrechts University, D-24098 Kiel, Germany

†Department of Physics, West Virginia University, Morgantown, West Virginia 26505-6315, USA

Abstract. The response to an external modulation voltage of small dust clouds confined in an anodic plasma is studied. Dust density waves are excited when the cloud is larger than a wavelength, whereas a sloshing and stretching motion is found for smaller clouds. The wave dispersion shows similarities with waveguide modes.

Keywords: dusty plasmas, plasma magnetohydrodynamics
PACS: 52.27.Lw, 52.30.Cv

The dispersion relation of dust density waves (DDWs) at low collision rate was subject of several investigations [1, 2, 3]. These investigations were made in large dust clouds, with dimensions much greater than the wavelength, which were trapped in anodic plasmas. The wave frequency was varied by applying an additional modulation voltage of typically (15 - 50) Hz to the anode. Recently, Thomas et al. [3] analyzed the DDWs at high frequencies of (15-150) Hz with a finite dust temperature and wave interference effects. The confinement of the dust and the wave dynamics are quantitatively understood [2] and the waves can be described by a kinetic model [4]. On the other hand, the dynamics of small dust clouds is less well understood, e.g. the modification of the wave by the finite cloud size. In this contribution the response of small ($d < \lambda$) and medium-size ($d \geq \lambda$) dust clouds to modulation of the anode bias is studied. The experimental setup is the same as in Ref. [2].

The response of small dust clouds to a periodic modulation of the anode bias is a combined sloshing and stretching motion as can be seen in the insets of Fig. 1. Panels (a,b,c) correspond to the elongation towards the anode, the equilibrium position and away from the anode, respectively. The sloshing amplitude of the center-of-mass motion and the major semiaxis of the dust cloud, which is a measure of the stretching process, show a resonant enhancement at $f = 4$ Hz. In the wave regime, $f > 20$ Hz, no significant response is found. Dust density waves in a horizontal cross-section through a larger dust cloud are shown in the inset of Fig. 2. These waves exist typically in the regime $f = 20 - 40$ Hz. Because of the external modulation the waves are highly coherent. Therefore, the full phase information of the wave could be retrieved from the time evolution of the intensity of each pixel in a series of 1000 movie frames. Comparing the phase evolution in a stack of horizontal sections, we could derive the full three-dimensional wave field. The measured dispersion in the main propagation direction of the wave is shown by the symbols in Fig. 2. Unexpectedly, the phase velocity of this wave significantly deviates from the group velocity, which we attribute to the finite size

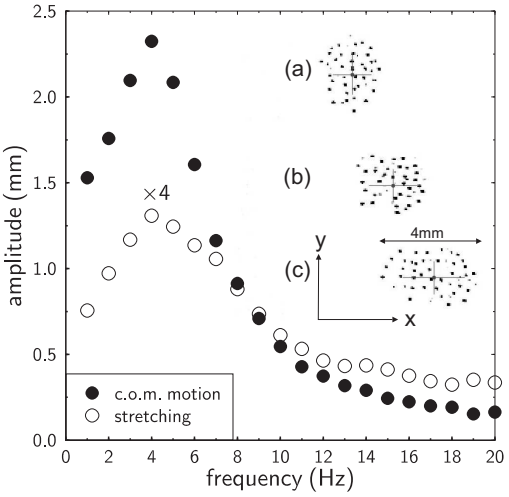

FIGURE 1. Small dust clouds respond to external modulation of the anode bias by a combined sloshing and stretching motion with a pronounced resonance at $f = 4$ Hz.

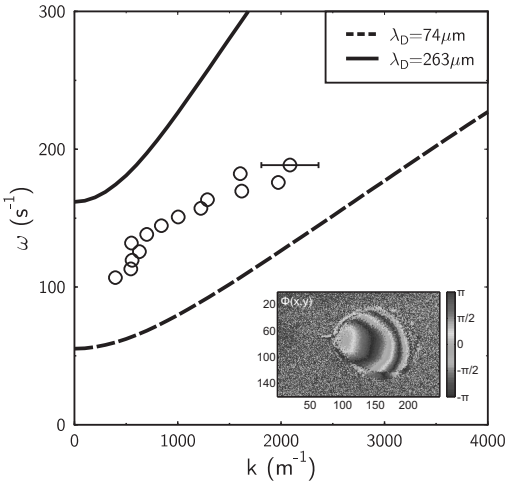

FIGURE 2. Medium-size dust clouds show dust density modes. The dispersion deviates significantly from acoustic dispersion. Two extreme cases of dispersion in finite geometry are shown.

of the dust cloud. Similar deviations from acoustic dispersion was found in bounded dusty plasmas [5], which results in a cut-off frequency. When dust neutral collisions are neglected, the dispersion is given by $\omega = \omega_{pd}\left[(k^2+\gamma^2)/(k_\mathrm{D}^2+k^2+\gamma^2)\right]^{1/2}$. Here, k_D is the Debye wavenumber and $\gamma = 2.4/R$ represents the fundamental mode. This gives a cutoff frequency $\omega_\mathrm{min} = \omega_\mathrm{pd}\,\gamma\,(k_\mathrm{D}^2+\gamma^2)^{-1/2}$. At our experimental conditions ($n_d = 1.7\times10^{10}\mathrm{m}^{-3}$, $Z_d = 3000$) we obtain $\omega_{pd} \approx 780\ \mathrm{s}^{-1}$. The diameter $2R \approx 5$ mm of the waveguide is estimated from the transverse dimension of the dust cloud

In Fig. 2 we have plotted the result for such modes in two limiting cases: In the first case, assuming thermal ions with $k_\mathrm{B}T_\mathrm{i} = 0.1$ eV, the ion Debye length becomes $\lambda_\mathrm{Di} = 74\ \mu\mathrm{m}$ and, because $T_\mathrm{e} \gg T_\mathrm{i}$, $\lambda_\mathrm{D} \approx \lambda_\mathrm{Di}$. Then the dust acoustic velocity becomes 74 mm/s, which is smaller than the observed phase velocities. In the second case, we assume that the ions have the Bohm speed, $v_\mathrm{B} = \omega_{pi}\lambda_{\mathrm{D},e}$. In this limit, ion shielding is reduced and the estimated ion shielding length is $\lambda_{\mathrm{D},i} \approx \lambda_{\mathrm{D},e}$, which results in $\lambda_\mathrm{D} \approx 2^{-1/2}\lambda_{\mathrm{D},e} \approx 263\ \mu\mathrm{m}$.

The present investigation were financially supported by DFG within the transregional collaboration research center TR-24, Project A2.

REFERENCES

1. A. Barkan and R.L. Merlino, Phys. Plasmas **2**, 3563 (1995)
2. T. Trottenberg *et al.*, Phys. Plasmas **13**, 042105 (2006)
3. E. Thomas, Jr. *et al.*, Phys. Plasmas **14**, 123701 (2007)
4. M. Rosenberg, J. Plasma Phys. **67**, 235 (2002)
5. P. Shukla and M. Rosenberg, Phys. Plasmas **6**, 1038 (1999)

List of Publications

Publications in Peer-Reviewed Journals

Part of this thesis:

[B.1] I. Pilch, T. Trottenberg, A. Piel, and M. E. Koepke.
Dynamics of small dust clouds trapped in a magnetized anodic plasma.
Phys. Plasmas **14**, 123704 (2007).

[B.2] I. Pilch, T. Reichstein, and A. Piel.
Torus-shaped dust clouds trapped in a magnetized anodic plasma.
Phys. Plasmas **15**, 103706 (2008).

[B.3] I. Pilch, T. Reichstein, and A. Piel.
Synchronization of dust density waves in anodic plasmas.
Phys. Plasmas **16**, 123709 (2009).

Further Publications:

1. A. Piel, O. Arp, D. Block, I. Pilch, T. Trottenberg, S. Kading, A. Melzer, H. Baumgartner, C. Henning, and M. Bonitz.
Complex plasmas: forces and dynamical behaviour.
Plasma Phys. Control. Fusion **50**, 124003 (2008).

2. T. Reichstein, I. Pilch, R. Grosse-Ahlert, and A. Piel.
Toroidal dust clouds and voids in a magnetized anodic plasma.
IEEE Trans. Plasma Sci. **38**, 814 (2010).

Selected Contributions to International Conferences:

[C.1] I. Pilch, M. E. Koepke, A. Piel-, T. Trottenberg.
Synchronization of dust density waves in anodic plasmas.
Europhysics Conference Abstracts Vol. **31F**, P-5.062 (2007).

[C.2] A. Piel, I. Pilch, T. Trottenberg, M. E. Koepke.
Three-dimensional structure of dust clouds and wave fronts in an anodic plasma.
Europhysics Conference Abstracts Vol. **31F**, P-5.063 (2007).

[C.3] I. Pilch, T. Reichstein, F. Greiner, and A. Piel.
Torus-Shaped Dust Clouds in Magnetized Anodic Plasmas.
AIP Conference Proceedings **1041**, 303 (2008).

[C.4] A. Piel, I. Pilch, T. Trottenberg, and M. E. Koepke.
Dynamics of Finite Dust Clouds in a Magnetized Anodic Plasma.
AIP Conference Proceedings **1041**, 301 (2008).

Danksagung

An erster Stelle gilt mein Dank Herrn Prof. Dr. Alexander Piel für die Gelegenheit diese Arbeit anfertigen zu können. Die zahlreichen Diskussionen, manchmal auch zu sehr grundlegenden Fragestellungen, haben zum steten Fortschritt dieser Arbeit beigetragen. Außerdem möchte ich mich für die Ermöglichung meine Ergebnisse auf Tagungen präsentieren zu können bedanken.

An zweiter Stelle möchte ich mich bei Torben Reichstein für die *herzliche* Zusammenarbeit und das geduldige Korrekturlesen dieser Arbeit bedanken. Die offene und konstruktive Kritik mit einer Prise Physikerhumor sowie seine gründliche Arbeit zur Diagnostik des anodischen Plasmas waren stets hilfreich.

Für die zahlreichen Diskussionen hinsichtlich der Staubdichtewelle möchte ich mich bei Kristoffer Ole Menzel bedanken. Die vielen Fragen, was denn eine Welle ausmacht und wie man das verstehen kann, haben manchmal etwas Verwirrung gestiftet; jedoch konnte der Gedankenknoten meist mit vielen *mmmh's* und *äh's* gelöst werden.

Ebenso möchte ich mich bei Dr. Oliver Arp und Dr. Franko Greiner, die gerne mit Rat und Tat zur Seite standen, sowie Dr. Dietmar Block für seine aufrichtige Kritik bedanken. Für die bereitwillige Unterstützung zur Lösung von technischen Problemen danke ich Michael Poser, Volker Rohwer und Mario Knüppel. Für den Aufbau und erste Untersuchungen mit der ITO Anode im Rahmen seiner Diplomarbeit gilt mein Dank Robert Große-Ahlert. Frau Thiedemann und Frau Seeger möchte ich für die Unterstützung in bürokratischen Angelegenheiten danken.

Der gesamten Arbeitsgruppe danke ich für das entspannte und freundliche Arbeitsklima, den Kuchenwetten sowie den zahlreichen Tee-/Kaffeepausen, die den Arbeitsalltag aufgehellt haben. Insbesondere möchte ich Mattes Kroll und Imke Goertz für deren offenes Ohr, wenn etwas mal nicht so wollte, wie es sollte, danken.

Zu guter Letzt möchte ich mich bei den Menschen aus meinem privaten Umfeld bedanken, die für die notwendige Abwechslung zur Arbeit gesorgt haben.

Zum einen möchte ich mich bei den Damen für die lustigen Augenblicke während des Trainings und der Spiele bedanken. Zum anderen muss ich an dieser Stelle anmerken, dass ich nur so viel laufe, um euch zu *ärgern*.

Für die lange Begleitung durch die Höhen und Tiefen dieser Arbeit, des Alltags *und so* möchte ich Alexandra Hohmann danken.

Meinen Eltern und meinen Brüdern möchte ich aufrichtig und von Herzen für die stetige Unterstützung in jeder Lebenslage, das Vertrauen und den Rückhalt, dass jemand da ist, falls man ihn braucht, danken.

Lebenslauf

Persönliche Daten

Name:	Iris Pilch
Geburtsdatum:	16.12.1981
Geburtsort:	Kappeln
Staatsangehörigkeit:	deutsch
Familienstand:	ledig

Schulbildung

1988 - 1992	Grundschule Mohrkirch in Mohrkirch
1992 - 2001	Bernstorff Gymnasium in Satrup
Juni 2001	Abitur mit den Prüfungsfächern: Physik, Mathematik, Erdkunde und Kunst

Studium

Okt. 2001	Immatrikulation im Fach Physik an der Christian-Albrechts-Universität zu Kiel
Okt. 2003	Vordiplom mit Nebenfach Informatik
Aug. 2005	Mündliche Diplomprüfungen mit Nebenfach Astrophysik
Okt. 2005 - Okt. 2006	Anfertigung der Diplomarbeit "Experimente zur Synchronisation von Staubdichtewellen" in der Arbeitsgruppe "Plasmadynamik" am Institut für Experimentelle und Angewandte Physik der Christian-Albrechts-Universität zu Kiel
Nov. 2006	Beendigung des Studiums der Physik mit Abschluss Diplom
seit Nov. 2006	Promotion in der Arbeitsgruppe "Plasmadynamik" am Institut für Experimentelle und Angewandte Physik der Christian-Albrechts-Universität zu Kiel

Eidesstattliche Erklärung

Hiermit versichere ich an Eides Statt, dass die vorliegende Dissertation - abgesehen von der Beratung durch meinen wissenschaftlichen Lehrer und der Verwendung der angegebenen Hilfsmittel - nach Inhalt und Form meine eigene ist. Sie hat weder ganz noch teilweise an einer anderen Stelle im Rahmen eines Prüfungsverfahrens vorgelegen.

Kiel, den